Effects of Dipole Model for Magnetic Induction on Biomedical Devices

Jiyun Jeon

Department of Mechanical Engineering

Graduate School of UNIST

Effects of Dipole Model for Magnetic Induction on Biomedical Devices

A dissertation
submitted to the Graduate School of UNIST
in partial fulfillment of the
requirements for the degree of
Doctor of Philosophy

Jiyun Jeon

12. 09. 2019

Approved by

Advisor
Hungsun Son

Effects of Dipole Model for Magnetic Induction on Biomedical Devices

Jiyun Jeon

This certifies that the dissertation of Jiyun Jeon is approved.

12. 09. 2019

Advisor: Hungsun Son

Jae Joon Kim

Ki-Suk Lee

Hyungson Ki

Sang Hoon Kang

Abstract

Magnetic field has been utilized in the biomedical applications for numerous decades, owing to contactless, noninvasive and harmless property, low cost and robustness in operation, and increased safety compared to other radiative fields. The medical applications using magnetic field have been investigated to enhance their performance. Such applications require accurate analysis of the magnetic field for improvement. However, it is difficult to compute the time-varying magnetic field, due to nonlinearity and interactions by various electromagnetic properties. The problems take a lot of computational time for analysis and cause the ill-posed condition.

In this dissertation, the magnetic field is analyzed to develop the medical applications, using the extended distributed multi-pole (eDMP) method. The method utilizes the magnetic dipole moments to solve not only nonlinearity but also interactions and improve ill-posed condition. Based on the modeling method, the magnetic field can be controlled. Then the control method contributes to construct the magnetic field which enhance the performance of the applications.

The methods are illustrated in two applications with experiments: a navigation sensor for an intubation tube and magnetic induction tomography (MIT). The navigation sensor for a tube is proposed to prevent a potential danger of perforation during tube intubation. A trajectory of the tube is reconstructed, based on the magnetic induction. The eDMP method is used to modeling the system and the optimal design is found, considering the practical usage.

A MIT is a medical imaging device mapping conductivity of target objects. It shows inferior performance due to low signal-to-noise ratio and ill-posed condition. The eDMP method is applied to analyze the magnetic field of the MIT system and implement the system to reconstruct an image. The various materials with different conductivities are applied and their properties, such as the shape and conductivity, are characterized. Eventually, it is expected that the MIT system makes image of the biological cell and could be developed as the medical device.

Contents

List of figures

List of tables

Nomenclature

Upper characters

$\mathbf{A}$	Magnetic vector potential
$\mathbf{B}$	Magnetic flux density
$\mathbf{E}$	Electric field
E	Error
I	Current
$\mathbf{J}$	Current density
M	Mutual inductance
R	Resistance
L	Inductance
C	Capacitance

Lower characters

$\mathbf{r}$	Magnetic vector potential
$\mathbf{B}$	Magnetic flux density
$\mathbf{E}$	Electric field
r	Error
I	Current
$\mathbf{J}$	Current density
$\mathbf{m}$	Dipole moment
$\mathbf{P}$	Sensitivity matrix

Greek characters

$\boldsymbol{\gamma}$	Radius of eddy current loop

$\boldsymbol{\varepsilon}$	Electric permittivity
φ	Phase delay
μ	Permeability
ω	Angular frequency
σ	Conductivity
κ	Complex conductivity
Φ	Scalar potential

Abbreviation

eDMP	Extended distributed multi-pole
MIT	Magnetic induction tomography
SD	Single dipole

1. Introduction

1.1 Motivation

Magnetic field has been applied to the biomedical devices since it offers a number of advantages, such as relatively high sensitivity in measurement, robustness in operation against temperature changes, contactless target applicability, and increased safety compared to other radiative fields. For example, magnetic resonance imaging (MRI), a medical imaging device, applies the magnetic field to cause resonance in the human tissue to reconstruct image for the tissue for diagnosis. Transcranial magnetic stimulation (TMS) is a technique which treats neuron using magnetic pulse. Magnetic locomotion is utilized to manipulate a micro-robot wirelessly for drug deliver and capsule endoscopy. Magnetic induction tomography is a novel medical imaging device. As the performance of the applications depends on a magnetic field of each system, the applications can be developed by analyzing the magnetic field.

However, it is difficult to analyze a magnetic field due to nonlinearity and interactions with other materials. There are many nonlinearities in the governing equations of the magnetic field. Even the accurate solver, it takes a lot of time for computation and thus the real-time applications, such as sensing and control, are limited. The magnetic interactions are caused with various materials and they depend on the electromagnetic properties, such as conductivity, permittivity and permeability. Geometry between the materials should be considered. Furthermore, the problems also cause ill-posed condition in the applications of the magnetic field. For example, MRI takes the signal from the patient’s body and compute inverse of the signal for analysis. But, the complexity of the magnetic field makes it hard. Then accuracy is reduced and computational time increases dramatically.

Thus, in this dissertation, the novel modeling method solving the nonlinearity and interactions fast is proposed. Due to fast computation, it could be utilized to control the magnetic field, and further implement the real-time sensing. In particular, the applications using the magnetic induction are investigated to demonstrate the capability of the proposed method.

1.2 Research tasks and contribution

Magnetic field model has been investigated to analyze and utilize the magnetic field for several hundred years. The magnetic single dipole (SD) model provides accurate and fast analysis for the magnetic field. The method can be applied to control individual EMs in real time [1] although it generates a relatively accurate field in the case of needle-shaped magnets. The modeling error increases as the shape becomes complex so that it has been used to analyze the far field of antennas [2]. The extended distributed multipole (eDMP) method has been developed to overcome the drawbacks of the SD method, and provide accurate modeling for the near magnetic field for EMs.

In this research, the eDMP model is further investigated for various designs of EMs and applied to compute magnetic interactions in complex geometry. Then, the method is developed to control the strength and orientation of the magnetic field by using EMs. The methods can be validated by comparing with experiments.

The practical biomedical applications using magnetic induction are presented: navigation sensor for intubation tube and magnetic induction tomography (MIT). The system of each application is analyzed, and then the system design is improved for better performance.

1.2.1. Voice coil navigation sensor

A navigation sensor has been used widely for the medical devices, such as minimally invasive surgical robotics [3, 4], flexible catheters, injecting needles and endoscopy [5], due to low cost, noncontact and harmless properties. It also could be applied to prevent damage during tube intubation. Tube intubation has been utilized for supplement of nutriment, fresh air and monitoring but could cause perforation. In Fig. 1.1, the utilization of intubation tube is shown and each path for esophagus and trachea are drawn. The path is curved sharply at throat area (red circle). As tube intubation depends on a hand of an operator, it could cause injury. Thus, real time navigation sensor is required to avoid damage.

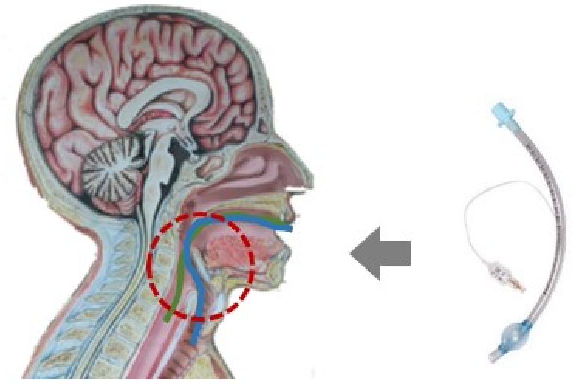

Fig. 1.1. Utilization of intubation tube

Fig. 1.2 shows the concept of a navigation sensor, comprises exciter coil and sensor coil winding an intubation tube. The sensor coil is inclined and the exciter causes magnetic induction on the sensor. As the tube is bent, induced voltage on the sensor change. Even with the symmetrical bending, the induced voltage is different due to the inclined angle. Finally, a path of the tube can be reconstructed. The system is analyzed to demonstrate the feasibility and then, design is optimized to enhance sensitivity considering practical use.

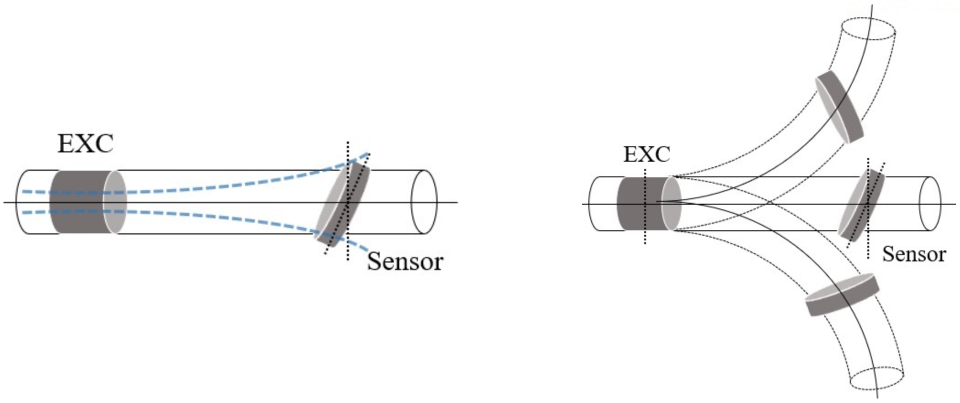

(a) Without bending (b) With bending

Fig. 1.2. Concept of coil navigation sensor

1.2.2. Magnetic induction tomography

Magnetic induction tomography (MIT) is a medical imaging device that uses conductivity to characterize a target object. The existing imaging devices, such as X-ray, CT, and MRI, have been in use for several decades. However, the instruments used in these devices are large and incur high power and cost. In addition, an expert is required to operate the devices, as they can be harmful. In contrast, MIT incurs low power and cost, and thus, is portable and can be used during emergency. In addition, owing to its noninvasive and harmless properties, experts are not required for operation.

A system of MIT comprises transmitter (Tx) coil, receiver (Rx) coil and target objects, as Fig. 1.3(a). A Tx generates the primary field $\mathbf{B}_p$ and then eddy current I_e is induced on the objects. The current generates the secondary field $\mathbf{B}_s$ and both fields are measured by a Rx. $\mathbf{B}_s$ causes phase shift as shown in Fig. 1.3(b). Image can be reconstructed by mapping conductivity σ, in Fig. 1.3(c).

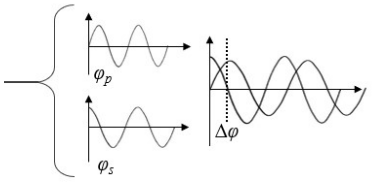

(b) Phase shift in Rx

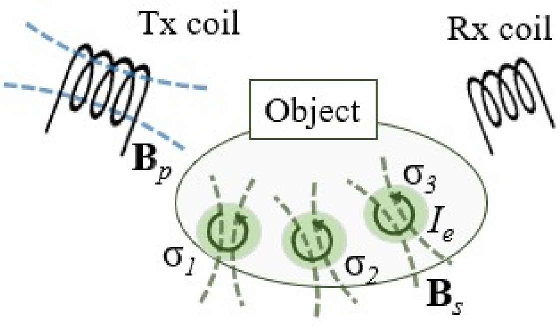

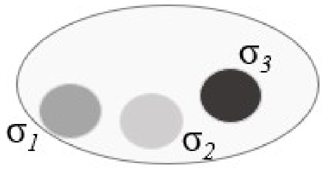

(a) MIT system (c) Imaging result

Fig. 1.3. Principle of MIT

The principle has been utilized in the industry to detect the metal crack for a hundred years [6]. MIT for low conductivity material has been investigated for early 90s [7]. But it still exhibits inferior performance due to the nonlinearity, low signal-to-noise ratio of the magnetic field, and ill-posed inverse problem. Thus, the system is analyzed using the proposed modeling method and then, constructed to detect the living cell.

1.3 Thesis organization

This dissertation is organized as follows: Chapter 1 shows the research motivation and tasks for magnetic biomedical applications. In chapter 2, background studies for the research tasks are introduced. Electromagnetic field modeling methods are investigated and the origin of the eDMP method is explained. Then, researches about the magnetic field control are presented. Chapter 3 presents electromagnetic field modeling and field control using the eDMP. The two illustrative applications, navigation sensor and MIT are investigated in chapter 4 and 5, respectively. The two applications are analyzed and constructed to prove their performance. Last, achievement and contribution of this dissertation are summarized and open issues are discussed in chapter 6.

2. Literature reviews

In this chapter, background studies related to the research tasks are reviewed. First, the governing equation of magnetic field and the common solutions are introduced for magnetic field modeling. The distributed multi-pole (DMP) model for a permanent magnet (PM) is referred to explain the concept of the eDMP model. Next, literatures about magnetic field control are presented and their method, application and results are discussed. Last, researches for MIT are introduced to understand its research history, current performance and future works.

2.1 Magnetic field analysis

2.1.1 Background of electromagnetic field

Magnetic field in a free space is basically expressed as the magnetic flux density **B**, following the Maxwell's equations as below.

$$\nabla \cdot \mathbf{E} = \frac{\rho}{\varepsilon_0} \tag{2.1}$$

$$\nabla \cdot \mathbf{B} = 0 \tag{2.2}$$

$$\nabla \times \mathbf{E} = -\frac{\partial \mathbf{B}}{\partial t} \tag{2.3}$$

$$\nabla \times \mathbf{B} = \mu_0 \left(\mathbf{J} + \varepsilon_0 \frac{\partial \mathbf{E}}{\partial t} \right) \tag{2.4}$$

where **E** is an electric field of the electric charge density ρ; ε_0 is permittivity of free space; t is time variable; μ_0 is the permeability of free space; **J** is the electric current density.

From (2.2), **B** can be presented as a curl of the magnetic vector potential **A** and gradient of scalar potential Φ as (2.5-6).

$$\mathbf{B} = \nabla \times \mathbf{A} \tag{2.5}$$

$$\mathbf{B} = \mu_0 \nabla \Phi \tag{2.6}$$

There are four main types for a solution of the Maxwell's equations: analytical and numerical method, lumped parameter model, dipole moment model. Analytical method uses a general solution while numerical method approximates the governing equation numerically. Lumped parameter model simplifies the system with first order accuracy and dipole moment model utilize the magnetic dipole moment to modeling the magnetic source.

A general solution for the magnetic field is Biot-savart law, a function of current density loop **J** on a position **r'**, as shown in Fig. 2.1. Then **B** and **A** on an arbitrary position **r** is computed as (2.7-8). But it is hard to compute integration for the complex shape of current loop.

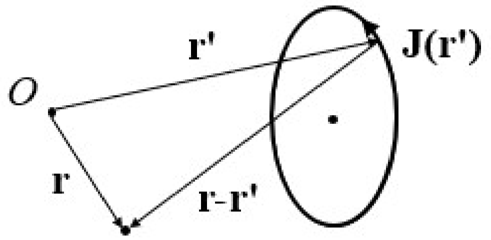

Fig. 2.1. Analytical model of magnetic field.

$$\mathbf{B}(\mathbf{r}) = \frac{\mu_0}{4\pi}\int \frac{\mathbf{J}(\mathbf{r}')\times(\mathbf{r}-\mathbf{r}')}{\left\|\mathbf{r}-\mathbf{r}'\right\|^3} d^3\mathbf{r}' \tag{2.7}$$

$$\mathbf{A}(\mathbf{r}) = \frac{\mu_0}{4\pi}\int \frac{\mathbf{J}(\mathbf{r}')}{\left\|\mathbf{r}-\mathbf{r}'\right\|} d^3\mathbf{r}' \tag{2.8}$$

Numerical method is capable of analyzing any complex geometry with high accuracy. There are many kinds of solution: finite element method (FEM), method of moment (MM), finite difference time domain method (FDTD). Each solution has different uses considering the system. Most solutions apply mesh to acquire reliability, as shown in Fig. 2.2. Thus, a lot of computational time is required.

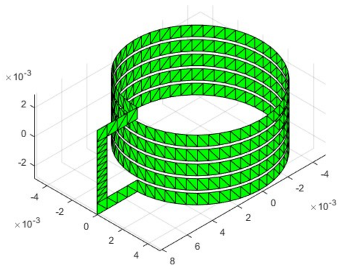

Fig. 2.2. MM method for a coil.

Lumped parameter model converts a system to a simplified model with first order accuracy. Fig. 2.3(a) shows an example of equivalent circuit model; two coil 1 and 2, and magnetic induction is caused between two coils. The system can be expressed as equivalent circuit in Fig. 2.3(b), with resistance R and self-inductance L. Magnetic induction is represented as mutual inductance M. As voltage v_g with frequency ω is supplied, currents flowing each coil, I_1 and I_2, can be computed as (2.9). Due to fast and intuitive computation, the equivalent circuit model is applied to compute the input current or voltage of the system [8], and an equivalent inertia model computes the specific mechanical parameters, such as torque [9]. The methods analyze the interaction between PMs and EMs but they are limited in describing detailed characteristics of each PM and EM, such as size and shape.

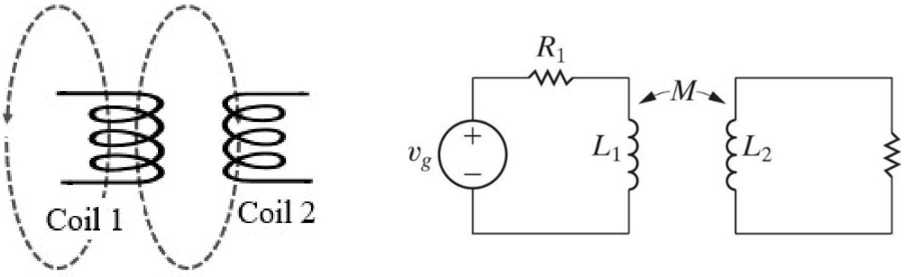

(a) Magnetic induction between coils (b) Equivalent circuit model

Fig. 2.3. Example of lumped parameter model.

$$\begin{bmatrix} v_g \\ 0 \end{bmatrix} = \begin{bmatrix} R_1 + j\omega L_1 & j\omega M \\ j\omega M & R_2 + j\omega L_2 \end{bmatrix} \begin{bmatrix} I_1 \\ I_2 \end{bmatrix} \tag{2.9}$$

Magnetic dipole model uses a magnetic dipole moment to approximate a current loop. As shown in Fig. 2.4(a), the actual source of magnetic field of an EM is the current loop. It can be represented as a single dipole (SD) moment **m** perpendicular to the current in Fig. 2.4(b) and magnetic field is computed as (2.10-11). The method can compute fast and has accuracy. The method can be applied to control individual EMs in real time [1] although it generates a relatively accurate field in the case of needle-shaped magnets. The modeling error increases as the shape becomes complex so that it has been used to analyze the far field of antennas [2].

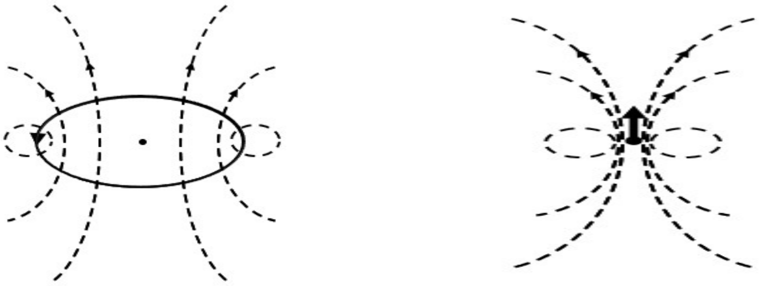

(a) Current loop (b) Dipole moment

Fig. 2.4. Concept of magnetic dipole model.

$$\mathbf{B} = \frac{\mu_0}{4\pi} \frac{\left[3(\mathbf{m} \cdot \hat{\mathbf{r}})\hat{\mathbf{r}} - \mathbf{m}\right]}{\|\mathbf{r}\|^3} \tag{2.10}$$

$$\mathbf{A} = \frac{\mu_0}{4\pi} \frac{(\mathbf{m} \times \hat{\mathbf{r}})}{\|\mathbf{r}\|^2} \tag{2.11}$$

Various magnetic field modeling methods and their application in MIT are analyzed. It is confirmed that lumped parameter model and magnetic dipole model can compute fast while accuracy is low. Both models have been used in magnetic field control. Low accuracy can be supplemented by combining with the other methods. But the variety of fields that could be generated is reduced due to small control parameters.

2.1.2 Distributed multi-pole model

The distributed multi-pole (DMP) method has been developed to overcome the drawbacks of the SD method for a permanent magnet (PM), offering accuracy at the near magnetic field [10]. As it is based on the dipole model, it has a closed form solution with fast computation. Fig. 2.5 shows a DMP model of a cylindrical magnet with radius a and height l, and the magnet is magnetized as $\mathbf{M} = M_o\mathbf{e}_z$. Magnetic poles are distributed on loops with radius $\overline{a}_j$ and height $\overline{\ell}_j$, following (2.12-14) and dipole moments $\mathbf{m}_j$ are parallel to $\mathbf{M}$. R_{ji+} and R_{ji-} indicate the distances from source (red points) and sink (blue points) poles to an arbitrary position P.

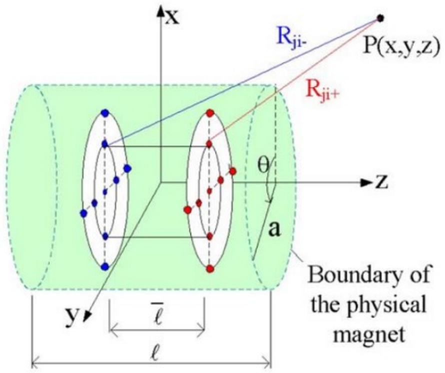

Fig. 2.5. DMP model of a cylindrical magnet [10]

$$\overline{a}_j = aj/(k+1) \quad (j = 1,\ \ldots,\ k) \tag{2.11}$$

$$z = \pm\overline{\ell}/2 \tag{2.12}$$

$$0 < \overline{\ell} < \ell \tag{2.13}$$

At P, a magnetic scalar potential Φ is presented as (2.14) using a magnetic pole, satisfying (2.2) and (2.6). Then, scalar potential of a single dipole in (2.14) can be computed using the DMP model in (2.15), as a summation of each poles.

$$\Phi = \frac{(-1)^p}{4\pi R}m \tag{2.14}$$

$$\Phi_{\text{DMP}} = \frac{1}{4\pi}\sum_{j=0}^{k} m_j \sum_{i=1}^{n_k}\left(\frac{1}{R_{ji+}} - \frac{1}{R_{ji-}}\right) \tag{2.15}$$

where m is the strength of the pole; p takes the value 0 or 1 designating that the pole is a source or a sink, respectively; and R is the distance from the pole to P.

The modeling parameters, such as position and strength, can be determined by minimizing the error between the reference field and the DMP field as (2.16). The analytical method of Φ in (2.17) could yield good prediction for the reference field of the cylindrical PM. Finally, flux density $\mathbf{B}$ at P can be expressed as dipoles in (2.18).

$$E = \int \left(\Phi_A - \Phi_{\mathrm{DMP}}\right)^2 \tag{2.16}$$

$$\Phi_A = \frac{1}{4\pi}\int_V \frac{-\nabla \cdot \mathbf{M}}{\left|\mathbf{R}-\mathbf{R}'\right|}dV + \frac{1}{4\pi}\int_S \frac{-\mathbf{M}\cdot\mathbf{n}}{\left|\mathbf{R}-\mathbf{R}'\right|}dS \tag{2.17}$$

$$\mathbf{B} = \frac{\mu_0}{4\pi}\sum_{j=0}^{k} m_j \sum_{i=1}^{n_k}\left(\frac{\mathbf{a}_{R+}}{R_{ji+}^2} - \frac{\mathbf{a}_{R-}}{R_{ji-}^2}\right) \tag{2.18}$$

where $\mathbf{a}_{\mathrm{R}+}$ and $\mathbf{a}_{\mathrm{R}-}$ are the unit direction vector of $\mathbf{R}_{ji+}$ and $\mathbf{R}_{ji-}$, respectively.

2.1.3 Magnetic field control

The demand for magnetic field control is increasing for effective performance under the limited input power. One of the famous applications is wireless power transfer (WPT) [11]. Magnetic field should be focused on a receiver to maximize the transferred power and reduce charging time. It was achieved by designing the transmitter coil to spiral shape. But most applications have many requirements, such as controlling magnitude and orientations at multiple points. Constructing the gradient field is used for MRI and magnetic locomotion control. Hence, the systematic algorithm which arrange the EMs to yield the desired field is necessary.

Kumer proposed eight coils controller to manipulate micro actuators using magnetic field [1]. Fig. 2.6 shows the system setup for field control; eight coils have same design but different orientations, pointing out the center of the ROI. Only current of the coils could be changed to control the field. Dipole model was applied to compute current of the needle shape coils, as shown in Fig. 2.6 (b). Due to various orientations, the system took good controllability and the field was controlled to yield a trajectory of the actuator as desired within μm range.

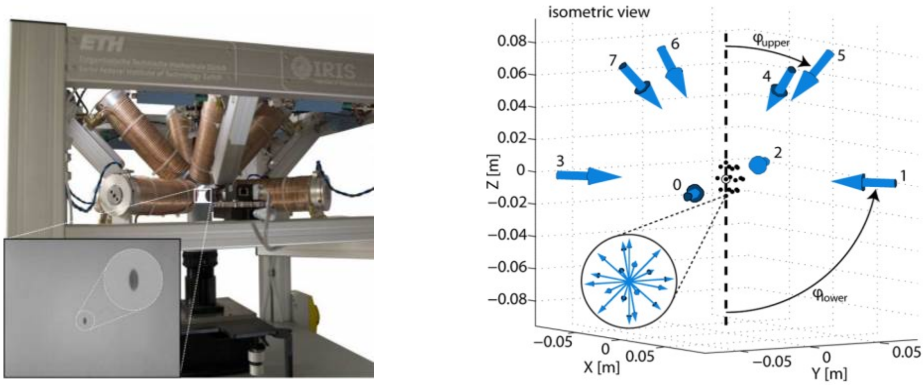

(a) Current loop

(b) Dipole moment

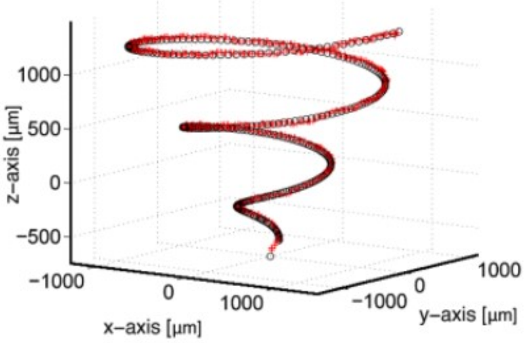

(c) Results of robot trajectory

Fig. 2.6. Magnetic field control [1]

Fig. 2.7 shows the ROI was expanded as wide as coils are distributed, by J. H. Kim [12]. The system has been proposed to focus a magnetic field on a specific region precisely. Rectangular Tx coils were arranged in a z-direction on a plane. As their positions were assigned, the analytical method could be applied to modeling the system. Then, lumped parameter model was used to compute the required current of each coil to control the magnetic field. Fig. 2.7 (b) and (c) present the simulation and experimental results as the field focusing on a center point was desired and it shows good agreement. But, in this system, it is hard to control the orientations of the field since their arrangements are uniform and fixed.

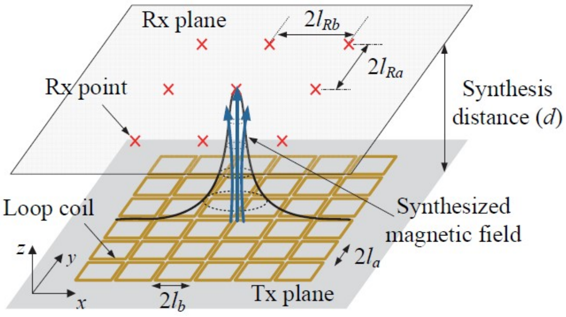

(a) System setup

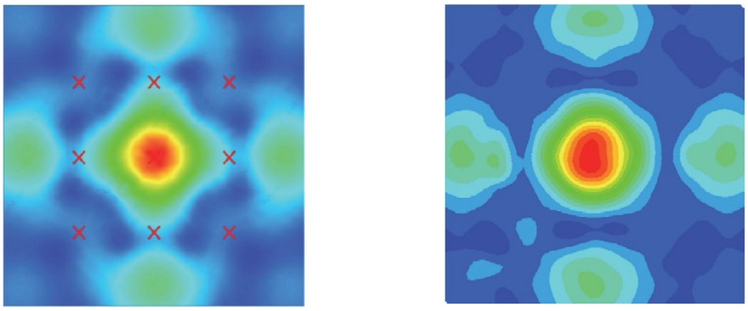

(b) Simulation

(c) Experiment

Fig. 2.7. Magnetic field focusing [12]

2.2 Biomedical applications

2.2.1 Navigation sensor

A navigation sensor as medical usage has been investigated with various types. Optical sensors are capable of detecting microscopic change in planar images in real time with fine resolution, but a light source and free line-of-sight are necessary [13]. It is difficult to secure line-of-sight during intubation since the light source is too bulky to insert into throat [14]. Ultrasound sensing offered the position and orientation of a surgical instrument in 3D [15]. Magnetic sensor, such as MRI, shows good performance in tracking [16], but MRI also requires a lot of cost.

For intubation process, mechanical sensor, such as fiber bragg grating sensor, could measure structure 3D deformation in real time using mechanical strain of the fiber [17]. It could be integrated in flexible needle shape devices due to small size. But a light source is required for operation and then cost become high. An oxygen sensor is used to measure the oxygen level and improve accuracy. However, the sensor has a few centimeters diameter, thus it is difficult to apply to the narrow medical tubes, such as a nasogastric tube. X-ray sensor could be a solution offering good imaging quality. However, it yields radiation hazard to patients and accumulation of X-ray could cause cancers. Electromagnetic tracking has been researched to detect the position and orientation by attaching a small sensor to the medical device [18-20]. It utilizes compact devices satisfying the specific requirements without any risk.

2.2.2 Magnetic induction tomography

It is also applied to detect metal for the industrial applications, such as steel and alloy [21, 22]. MIT can be combined with existing techniques, such as magneto-acousto-electrical tomography [23] and holography technique [24]. A MIT system as biomedical imaging device has been initially proposed by H. Griffith and Korjenevsky [7, 25]. Biological tissues are extremely low conductivity materials, lower than 5 S/m and permeability of them can be treated as 1. Owing to the properties, it can be assumed that the tissue objects have infinite skin depth, but the signal-to-noise ratio (SNR) could decrease dramatically, in contrast of metal applications. Basic design is shown in Fig. 2.8; multiple transmitters and receivers are surrounding the ROI and magnetic shield screen prevents magnetic noise for them. Korjenevsky presented the MIT system using 16 coils and yielded image for the objects with tissue level conductivities, as shown in Fig. 2.9. Due to lack of data, resolution is low and the object shape is not clear. Thus, many researches have been attempted to acquire a lot of useful data and develop the system.

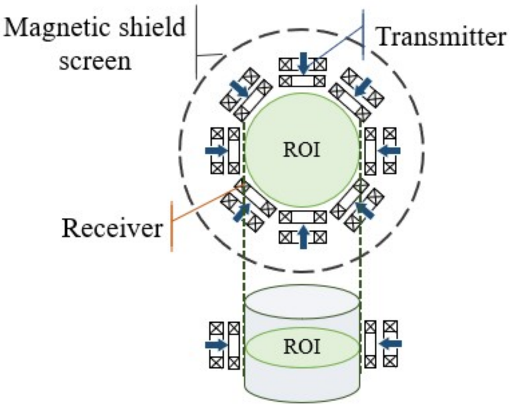

Fig. 2.8. Cylindrical MIT system.

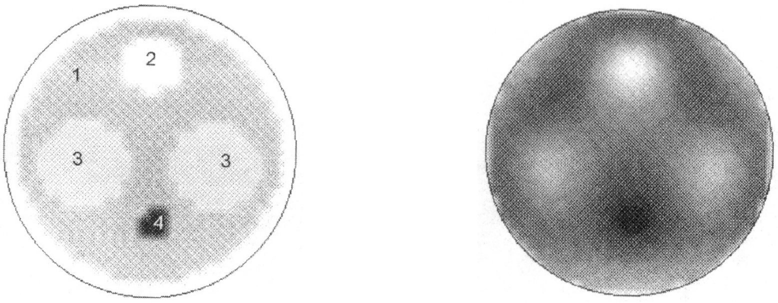

(a) True image (b) Experimental image

Fig. 2.9 Initial MIT [25]

H. Wei presented the rotational MIT in Fig. 2.10 to acquire many data [26]. As shown in Fig. 2.10 (a), 8 channels of coils were used but a lot of data are measured by rotating the coils. For the iron object with triangle shape, imaging results showed its shape with three angles in Fig. 2.10 (c).

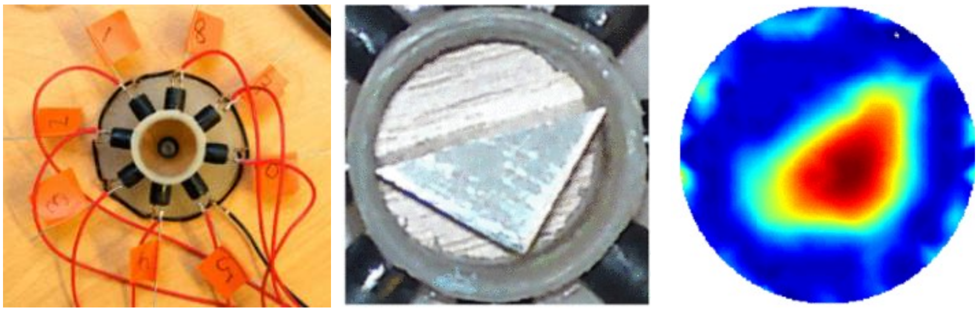

(a) System setup (b) True image (c) Imaging result

Fig. 2.10. Rotational MIT [29]

Jinxi Xiang achieved imaging for low conductivity objects using gradiometers [27]. As the gradiometer could increase SNR by cancelling the primary field, it has been used in MIT researches [28-30]. Fig. 2.11 shows the MIT system of Jinxi Xiang which comprises 8 Txs and 8 gradiometers. There are three low conductivity objects and the objects are observed and distinguished clearly in the experimental images.

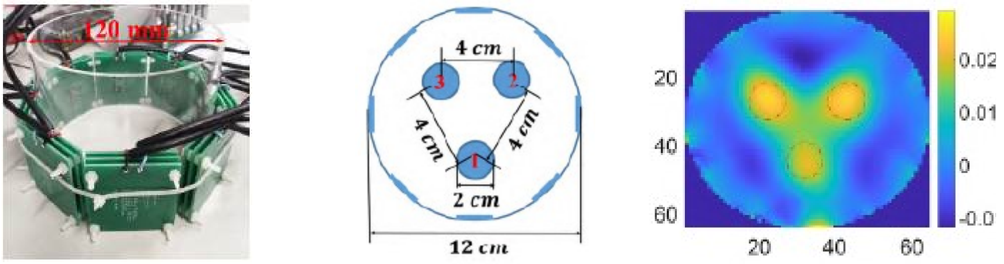

(a) System setup (b) True image (c) Imaging result

Fig. 2.11. MIT using gradiometer [27]

Target objects was initially set to saline water [31] and agarose [32] with conductivity equal to human tissue. It could be expanded to living animals, rats [33] and rabbits [34, 35]. Fig. 2.12 shows the experimental setup and result for detection of bleeding in a rabbit head. As time goes by, blood spreads and phase shift become higher.

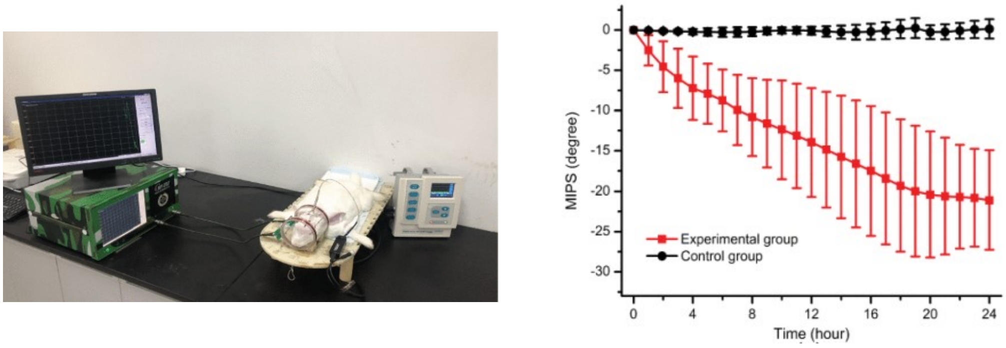

(a) Experimental setup (b) Result of phase shift

Fig. 2.12. MIT for rabbits [34]

Changing designs and arrangements of Txs and Rxs have been suggested, such as multichannel Rxs with different orientations [36]. D. Gursoy attempted to find an optimal array of the cylindrical MIT system changing the Tx and Rx, in order to detect multi objects in a cylinder 3D ROI [37].

In addition, a type of an Rx was changed, not only a voice coil but also atomic magnetometer [38], superconducting quantum interference device (SQUID). Atomic magnetometer and SQUID have precise sensitivity and resolution. To enhance SNR, shielding Txs and Rxs from noise and inserting an iron core into Txs are suggested in [39]. As the conductivity of human tissues depends on frequency, a multifrequency input has been applied to identify the function [29, 40, 41].

Image reconstruction algorithm is one of the important parameters determining imaging quality, since the MIT system has ill-posed condition during inverse, hence imaging algorithms have been investigated [42, 43]. Tikhonov regularization is widely used non-iterative algorithm yielding good accuracy even with ill-posed condition. But it requires to determine regularization parameter for effective computation. Total variation method is capable of denoising for image. Landweber method has been applied for X-ray imaging using iterative algorithm. X. Liu proposed a novel algorithm based on L_1-L_p norm which enhance spatial resolution of the reconstructed image [43].

Even though the development of MIT, it still shows inferior performance because the magnetic field is intrinsically weak, and the analysis of the field is nonlinear and rather complicated. Numerical methods have been utilized to analyze the magnetic field and design MIT systems for high accuracy [44-46]. However, the method requires heavy computational effort and contributes to increasing the system volume. Thus, a novel approach demanding fast computation and high accuracy is required to achieve a MIT system. A lumped parameter method is applied to identify and control the system in real time with first-order accuracy. The equivalent circuit model can identify eddy current distribution, and its interaction in tissues [47, 48]. However, this method faces difficulty in describing the detailed characters of the system, such as positions and orientations of Txs and Rxs. Thus, various methods are used to supplement the drawback. For example, in [47], an analytic method computes the induced voltage, and in [48], a numerical method solves the forward problem of MIT. However, combining the analytic and numerical method still requires high computational resource. Thus, the novel method which reduces the computation effort is required to compensate the ill-posed condition. Then, MIT would be implemented to reconstruct an image for a living cell.

3. Magnetic field modeling and control

3.1 Overview

In this chapter, a magnetic field which is generated by an EM is analyzed, based on the eDMP model since it is applicable to control a magnetic field owing to fast computation. Magnetic interactions between dipoles, such as mutual inductance, magnetic attraction/repulsion force and torque, are also computed. Modeling capability accounting for characters of an EM, such as design and position, could be demonstrated by modeling EMs with various designs and compared to the existing modeling methods. Then, a practical application, transcranial magnetic stimulation (TMS), is introduced for illustration of the eDMP. As mentioned in the previous section, TMS is a method to investigate and treat neurological disorder of the brain using magnetic pulses [49]. The induced electromagnetic fields from the pulse modulate the neural activity at target depth. Various designs of the TMS coil have been proposed to control the pulse propagation since its strength is attenuated rapidly during penetration [50, 51]. The effects of TMS coil designs on attenuation performance is analyzed.

In addition, the eDMP method is applied to control the magnetic field in the ROI such as a circular area. The magnetic field generated by two different EM designs is then simulated numerically and the results are compared to experimental. The active control for the magnetic field is demonstrated experimentally, and the experimental error is analyzed to validate controllability of the magnetic field. The control method is illustrated to manipulate the magnetic locomotion for the capsule endoscope. The capsule endoscope has replaced a conventional tube endoscope that often causes discomfort and injury to patients. Magnetic locomotion utilizes an actuator without additional batteries, unlike mechanical locomotion using motors. The locomotion of the actuator including magnetic materials could be controlled by implementing the magnetic field and its gradient. The results demonstrate capability and accuracy of the eDMP method to actively control magnetic field.

3.2 Extended distributed multi-pole method

3.2.1 Magnetic field modeling

The eDMP is based on the concept of a magnet that consists of a number of magnetic dipole moments. The magnetic field can then be expressed as a finite number of dipole moments. The method was originally used to analyze PMs [10], and was subsequently applied to EMs [52, 53]. Fig. 3.1 shows that the dipoles are distributed on two layers inside a cylinder coil with a current input I flowing through the conductors [54].

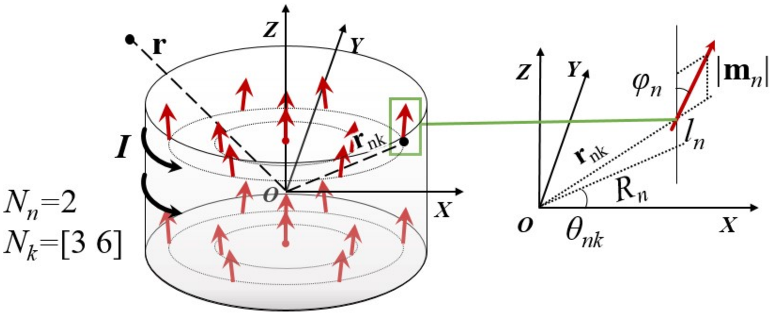

Fig. 3.1. eDMP model of a cylinder coil.

The magnetic dipoles presenting the red arrows in Fig. 3.1 are placed to characterize the magnetic field of the EM using modeling parameters. The position $\mathbf{r}_{nk}$ and the k^{th} dipole moment $\mathbf{m}_{nk}$ on the n^{th} layer are expressed in accordance to (3.1) and (3.2).

$$\mathbf{r}_{nk} = [R_n \cos\theta_{nk} \quad R_n \sin\theta_{nk} \quad \pm l_n]^{\mathrm{T}} \tag{3.1}$$

$$\mathbf{m}_{nk} = |\mathbf{m}_n|\left[\cos\theta_{nk}\sin\phi_n \quad \sin\theta_{nk}\sin\phi_n \quad \cos\phi_n\right]^{\mathrm{T}} \tag{3.2}$$

where R_n and l_n are the radius and height of the n^{th} layer, respectively. In addition, ϕ_n and $\|\mathbf{m}_n\|$ are the orientation and strength of a dipole moment on the layer, $\theta_{nk}=2\pi(k-1)/N_k$; $k=1,2,..,N_k$ and $n=0,1,2,..,N_n$ where N_k is the number of dipoles in the n^{th} layer; N_n is the number of layers; $R_n=0$ at $n=0$.

Based on the dipoles, the magnetic flux density (MFD) **B,** and the magnetic vector potential (MVP) **A** at an arbitrarily position **r,** are computed using (3.3) and (3.4).

$$\mathbf{B} = \frac{\mu_0 I}{4\pi}\sum_{n=0}^{N_n}\sum_{k=1}^{N_k}\left(\frac{3\left(\mathbf{m}_{nk}\cdot\left(\mathbf{r}-\mathbf{r}_{nk}\right)\right)\left(\mathbf{r}-\mathbf{r}_{nk}\right)}{\left\|\mathbf{r}-\mathbf{r}_{nk}\right\|^5} - \frac{\mathbf{m}_{nk}}{\left\|\mathbf{r}-\mathbf{r}_{nk}\right\|^3}\right) \tag{3.3}$$

$$\mathbf{A}(\mathbf{r}) = \frac{\mu_0 I}{4\pi}\sum_{n=0}^{N_n}\sum_{k=1}^{N_k}\frac{\mathbf{m}_{nk}\times\left(\mathbf{r}-\mathbf{r}_{nk}\right)}{\left\|\mathbf{r}-\mathbf{r}_{nk}\right\|^3} \tag{3.4}$$

where $\mathbf{m}_{nk}$ is the k^{th} dipole moment on the n^{th} layer; $\mathbf{r}_{nk}$ is a position of $\mathbf{m}_{nk}$; N_k is the number of dipoles in the n^{th} layer; N_n is the number of layers.

The parameters of the eDMP can be computed by minimizing the error between the predetermined magnetic field and the field described by (3.3) and (3.4). For the computation, the number of the magnetic dipoles and the layers, N_k and N_n, are initially set and increase when the error of field is not acceptable. Analytical or numerical methods could be used as a reference for the MFD, $\mathbf{B}_j^{Ref}$ in (3.5) with a unit current, and for the MVP in (3.6) and (3.6a) to compute the dipole moments.

$$Error = \sqrt{\sum_{j=1}^{N_j}\left\|\mathbf{B}_j^{Ref} - \mathbf{B}_j^{eDMP}\right\|^2} \le E_{DMP} \tag{3.5}$$

$$\mathbf{V}\begin{bmatrix}\mathbf{m}_0\\ \mathbf{m}_{11}\\ \vdots\\ \mathbf{m}_{N_n N_k}\end{bmatrix}_{I=1}=\begin{bmatrix}\mathbf{A}_1\\ \vdots\\ \mathbf{A}_{N_i}\end{bmatrix} \tag{3.6}$$

$$\mathbf{V}_{i,nk}=\frac{\mu_0}{4\pi d^3}\begin{bmatrix}0 & z & -y\\ -z & 0 & x\\ y & -x & 0\end{bmatrix} \tag{3.6a}$$

where E_{DMP} is the maximum desired error; $d = \|\mathbf{r}_d\|$ and $\mathbf{r}_d = \mathbf{r}_i - \mathbf{r}_{nk}$; $i=1,2,..,N_i$; $j=1,2,..,N_j$, where N_i *and* N_j are the number of positions to compute the MVP and MFD respectively and should be as many as possible to characterize the EM satisfying (3.5).

The magnetic field from dipole moments in (3.6) are based on a unit current input (I = 1). As input current changes, the MVP and MFD are proportional to the current input in (3.3) and (3.4). The eDMP algorithm is summarized in Fig. 3.2.

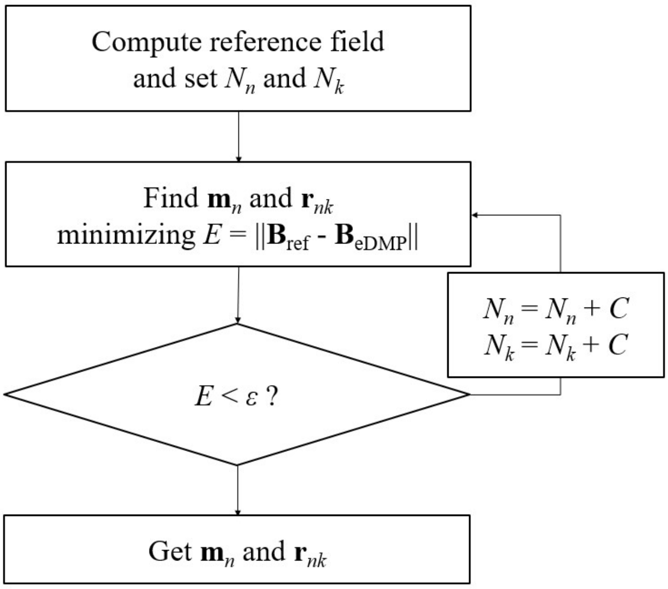

Fig. 3.2. Algorithm of eDMP method.

3.3.2 Magnetic induction

For the time-varying magnetic field, mutual inductance between coils causes the induced voltage on both coils. Fig. 3.3 shows two coils, *a* and *b*, at arbitrary positions and both coils are expressed as the eDMP model, $\mathbf{m}_a$ and $\mathbf{m}_b$ on positions $\mathbf{r}_a$ and $\mathbf{r}_b$, respectively. As $\mathbf{m}_a$ generates the magnetic field $\mathbf{B}_a$ on $\mathbf{r}_\text{b}$, mutual inductance between two coils, M_{ab}, is computed as (3.7). The method is capable of accounting for M_{ab} with any geometries between the coils in real time [55].

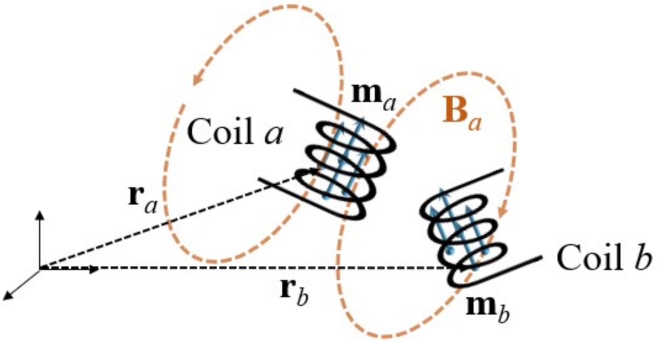

Fig. 3.3. Mutual inductance between two coils.

$$M_{ab} = \frac{1}{I_a I_b}\mathbf{m}_b \cdot \mathbf{B}_a(\mathbf{r}_b) = \frac{1}{I_a I_b}\sum_{i=1}^{N_i}\mathbf{m}_{bi} \cdot \sum_{j=1}^{N_j}\mathbf{B}_{aj}(\mathbf{r}_i) = \frac{1}{I_a I_b}\mathbf{m}_a \cdot \mathbf{B}_b(\mathbf{r}_a) \tag{3.7}$$

where N_j is the number of dipoles of coil a; N_i is the number of dipoles of coil b; I_a and I_b are input current of coil a and b, respectively.

Magnetic force and torque on magnet b caused by magnet a, $\mathbf{F}_{ab}$ and $\mathbf{T}_{ab}$, are also expressed as a function of dipole moments in (3.8-9). Fig. 3.4

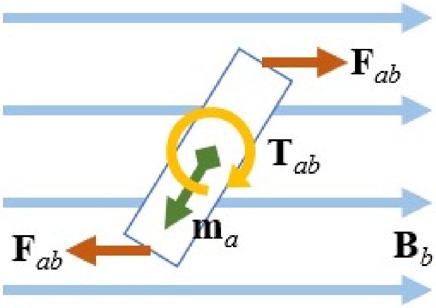

Fig. 3.4. Mutual inductance between two coils.

$$\mathbf{F}_{ab} = \nabla(\mathbf{m}_b \cdot \mathbf{B}_a) = \frac{3\mu_0}{4\pi}\sum_{i=1}^{N_i}\sum_{j=1}^{N_j}\frac{1}{|\mathbf{r}_{ji}|^5}\begin{bmatrix}(\mathbf{m}_{aj} \bullet \mathbf{r}_{ji})\mathbf{m}_i + (\mathbf{m}_{bi} \bullet \mathbf{r}_{ji})\mathbf{m}_j \\ +(\mathbf{m}_{bi} \bullet \mathbf{m}_{aj})\mathbf{r}_{ji} \\ -5(\mathbf{m}_{bi} \bullet \hat{\mathbf{r}}_{ji})(\mathbf{m}_{bi} \bullet \hat{\mathbf{r}}_{ji})\mathbf{r}_{ji}\end{bmatrix} \tag{3.8}$$

$$\mathbf{T}_{ab} = (\mathbf{m}_a \times \mathbf{B}_b) = -\sum_{j=1}^{N_j}\left[\mathbf{m}_{aj} \times \left(\sum_{i=1}^{N_i}\mathbf{B}_{bi}(\mathbf{r}_j)\right)\right] \tag{3.9}$$

3.3 Validation and application

3.3.1 Experimental validation

The eDMP method for the magnetic field of EMs is validated in two designs, namely, in a cylinder coil, and a taper coil. The coils are commonly described by the aspect ratio $\gamma = 2r/h$, with a radius r (mean radius in the taper coil) and a height h. However, the slant angle θ is only defined in the taper coil. The eDMP model of the cylinder coil is shown in Fig. 3.5 (a), and the model of the taper coil in Fig. 3.5 (b). The error corresponding to (3.5) is computed along the green dot set due to symmetry of the MFD. Similar to the SD model, the eDMP shows good agreement for low-aspect ratio coils but for high-aspect ratios, an increased number of dipoles is required to achieve accuracy. In addition, the eDMP method is applied to the taper coil. Correspondingly, the coil can be approximated as assemble of n cylinder coils with the aspect ratio γ_n appropriately arranged to account for the uniformly taper coil. Then, the method can be analyzed for various aspect ratios and slant angles.

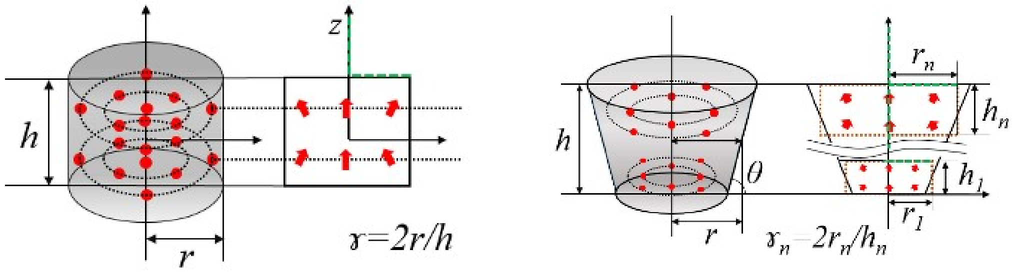

(a) Cylinder coil

(b) Taper coil

Fig. 3.5. eDMP model of coil.

The magnetic fields of the coils are compared along the central axis of the coil, from the coil's surface (z/h = 1) to a distance same as the coil's height (z/h = 2) for every 1 cm. The gap distance of 1 cm is precisely measured and controlled by a micrometer with ±1 μm accuracy.

The four methods are used: eDMP, analytical, numerical, and experimental results with the Gausemeter GM08 (*Hirst, in Falmauth, U.K.*). Analytic method is derived from Biot-Savart law and the numerical method is computed using the commercial software, COMSOL.

Cylinder coil: Three different aspect ratios, 0.5, 1.0 and 5.0, for the cylinder coils are compared in Fig. 3.6 (a). The parameters of the coils are listed in Table 3.1. Fig. 3.6 (b), (c), and (d) illustrate the individual results.

Table 3.1. Cylinder coil geometry

γ	0.5	1.0	5.0
h (cm)	1.2		
r (cm)	0.3	0.6	3.0
Wire diameter (mm)	0.3		
Number of turns	40		
N_n	2	2	8
N_k	[6 6]	[6 12]	[6 6 6 6 12 12 12 12]

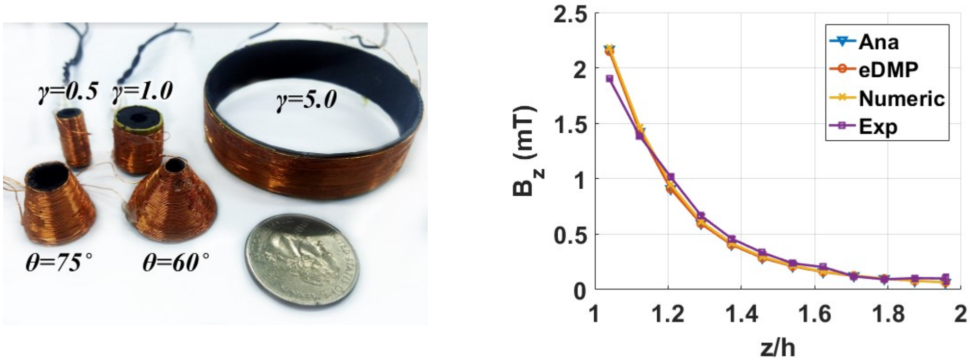

(a) Coil designs (b) $\gamma = 0.5$

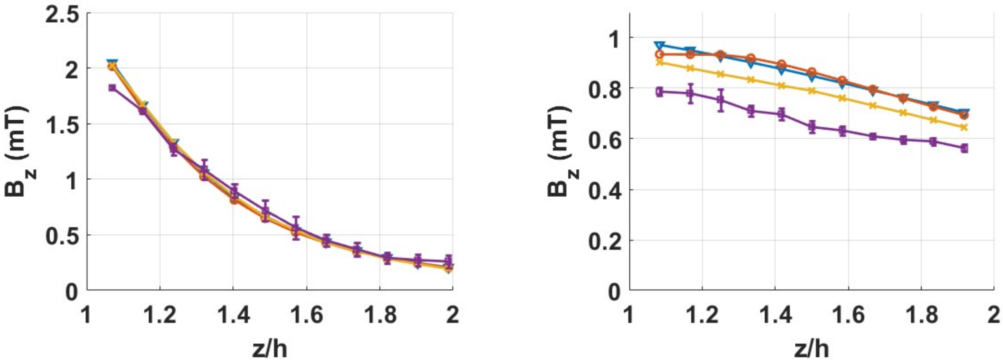

(c) $\gamma = 1.0$ (d) $\gamma = 5.0$

Fig. 3.6. MFD results of cylinder coils.

The error between the simulation results and experiments can be computed in (3.10) at the maximum error occurred. The magnetic field in the experiments has been measured in three times and standard deviation of the mean is computed in Table 3.2. As the aspect ratio increases, the number of dipoles also increase, in particular, near the surface where the dipoles cause a mathematical singularity resulting in a maximum error.

$$Error(\%) = \frac{\max\limits_{z}\left(\left|B_{Exp}(z) - B(z)\right|\right)}{B_{Exp}(z_{\max})} \times 100 \tag{3.10}$$

Table 3.2. Error analysis of Fig. 3.5

γ	0.5	1	5
eDMP (%)	13.2	10.5	33.7
Numerical (%)	14.7	10.9	22.1
Analytical (%)	14.2	12.2	31.3
Standard deviation (mT)	0.0142	0.0589	0.0212

Taper coil: The MFD of two slant angles of the coils in Fig. 3.6 (a), 60° and 75°, are compared on both narrow and wide surfaces since the field of a narrower surface always has a larger B_z than the wider surface. The detailed geometrical and modeling parameters are shown in Table 3.3, and results are compared in Fig. 3.7. Similar to the cylinder coils, the errors are computed as in (3.10), and the results are listed in Table 3.4. The maximum error of each method is within 10% with respect to each other.

Table 3.3. Taper coil geometry

θ (deg)	60	75
r (cm)	0.6	
Number of divisions	3	2
γ_n	2.675	1.963
N_n	3	4
N_k	[12 12 24]	[6 6 12 12]

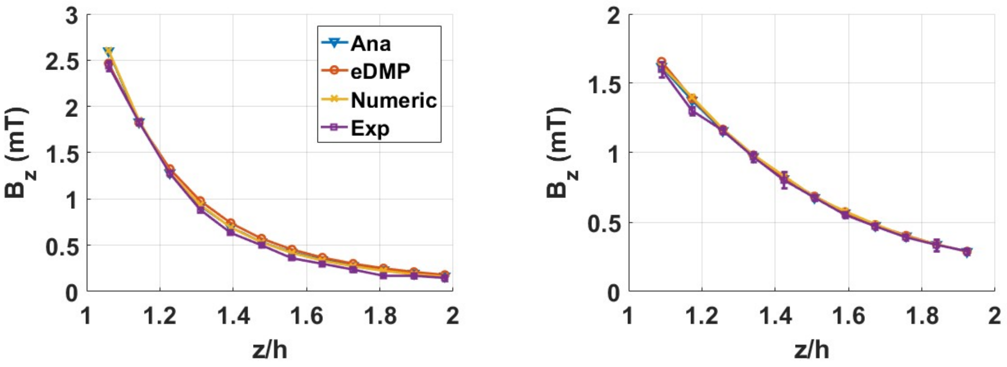

(a) Narrow side with $\theta = 60°$ (b) Wide side with $\theta = 60°$

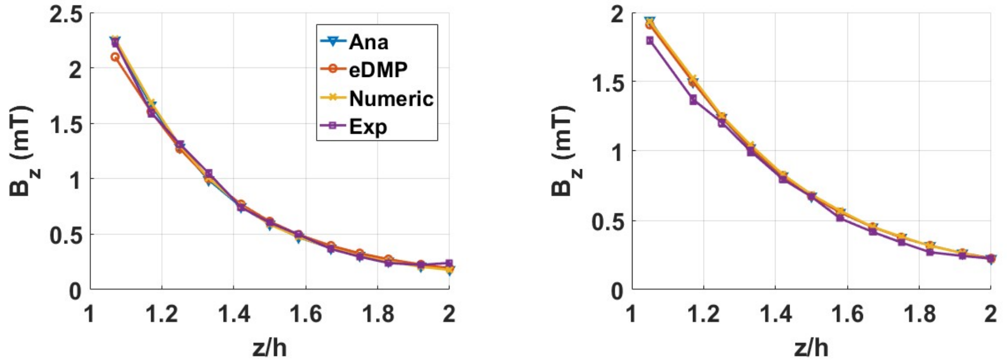

(c) Narrow side with $\theta = 75°$ (d) Wide side with $\theta = 75°$

Fig. 3.7. MFD results of taper coils

Table 3.4. Error analysis of Fig. 3.6

θ (deg)	60		75	
	Narrow	Wide	Narrow	Wide

eDMP (%)	6.50	6.69	6.02	9.09
Numerical (%)	6.90	7.49	5.77	11.1
Analytical (%)	8.23	5.68	4.20	7.98
Standard deviation (mT)	0.0214	0.0319	0.0167	0.0157

3.3.2 Illustrative application I: TMS

The eDMP method is utilized to analyze the stimulating performance of TMS coils. The attenuation during penetration and the spatial distribution of the MVP are analyzed for the three commercial coils in [51]. Fig. 3.8 (a), (c) and (e) show the design of the coils, the corresponding current flow ***I***, and the model of the human head that is approximated as a sphere with a radius of 8 cm. Relative permeability of the head can be assumed as 1 uniformly. The detailed geometric parameters are listed in Table 3.5.

Given that design I refers to a simple cylinder coil, the eDMP method can be applied as same as the cylinder coil in Fig. 3.5 (a). Design II is a taper coil and the required magnetic field is inside the coil winding unlike the taper coil in Fig. 3.5 (b). Thus, a set of magnetic dipoles are placed the outer layers of the coil winding. Design III has an arc shape, and it can be modelled as sum of a number of square coils along the circumference. Fig 3.8 (b), (d) and (f) show the eDMP model of each design, and the corresponding eDMP parameters are listed in Table 3.5. The strength of MVP is normalized by the maximum strength (in Table 3.5) and plotted on the ROI in the y-z plane in Fig. 3.9 (a)–(f). Furthermore, Fig. 3.10 shows the profiles taken from the location of the maximum vector potential to the center of the ROI, and the corresponding paths are illustrated in Fig. 3.9.

Table 3.5. TMS coil geometry

Design	I	II	III
Number of turns	7500	7500	7800
R (cm)	9		
t (cm)	2.25	1.5	0.3
β	3 cm	`	30 deg
γ	3 cm	30 deg	150 deg
Input current ***I*** (A)	1		
Current density (MA/m^2)	14.1		
N_n	4	4	2
N_k	[6 6 12 12]	[12 12 12 12]	[10 10]
Number of divisions	1	2	5
Max $\|\|\mathbf{A}\|\|$ (Vs/mm)	1.1	2.6	0.69

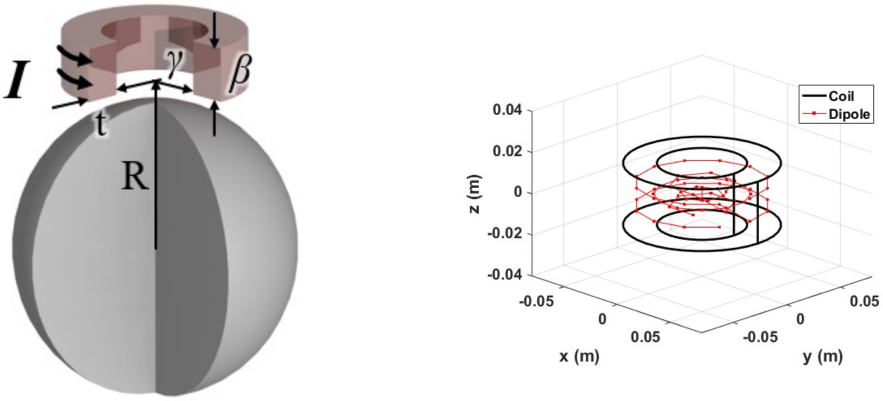

(a) Design I (b) Design I – eDMP model

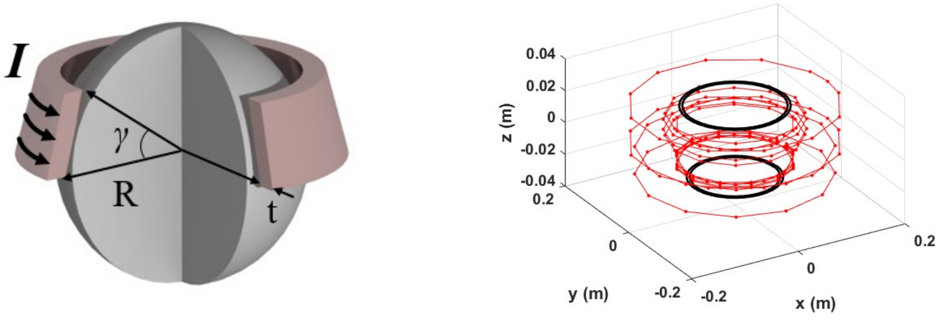

(a) Design II (b) Design II – eDMP model

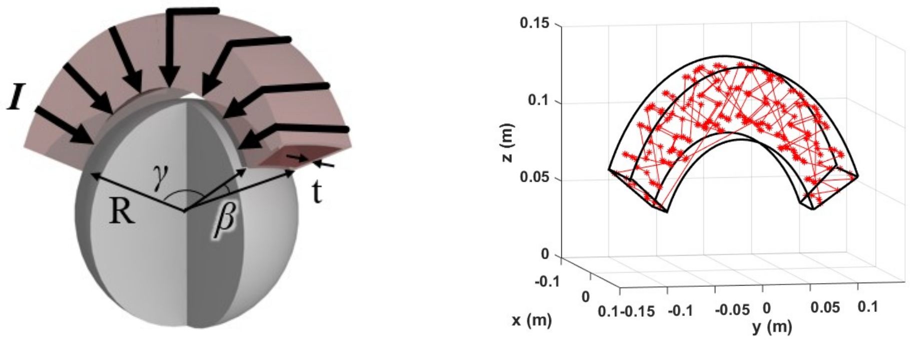

(a) Design III (b) Design III – eDMP model

Fig. 3.8. Design of TMS coils and eDMP model.

As shown in Table 3.5 and Fig. 3.9, both designs I and II can be applied to superficial stimulation of target depths within the range of 2–3 cm. Design III has the weakest of maximum field and may not be an optimal design compared to designs I and II. In Fig. 3.10, the response of design I are attenuated rapidly along the penetration depth. On the contrary, design II and III exhibit slow attenuation and generate sufficient field in deep TMS regions, requiring target depths in the range of 3–5 cm. Design II has better energy efficiency, but superficial region is risky due to unintended pulse. Considering the target depth, stimulated region and risk, an optimal TMS coil can be designed for a deep TMS.

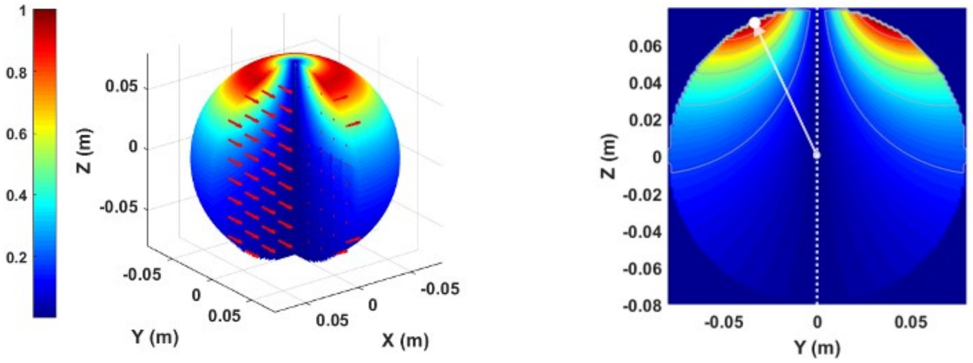

(a) Design I in 3D (b) y-z plane

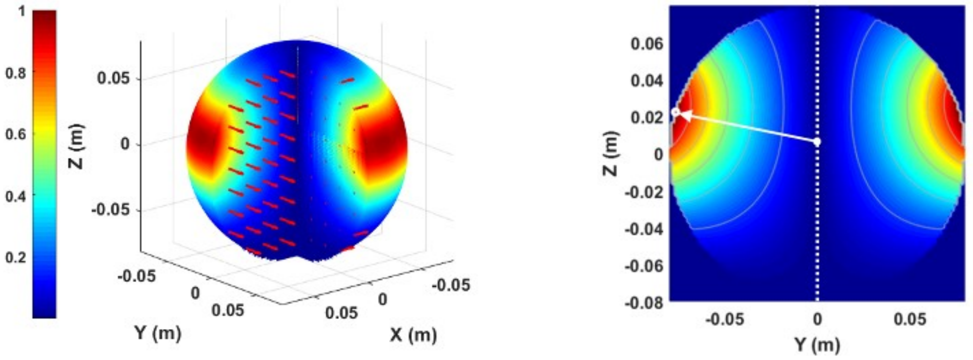

(c) Design II in 3D (d) y-z plane

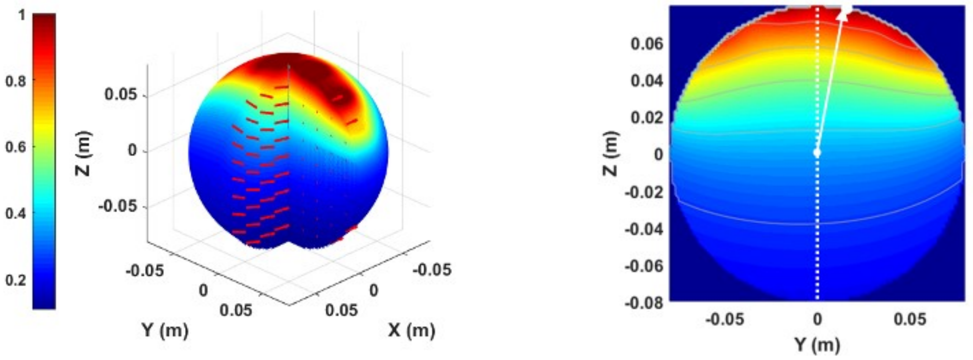

(e) Design III in 3D (f) y-z plane

Fig. 3.9. Normalized MVP for the proposed designs.

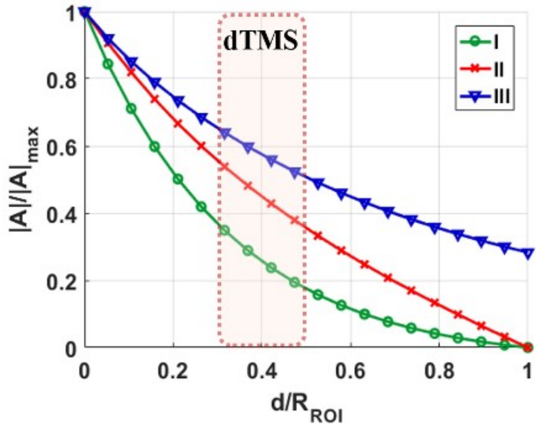

Fig. 3.10. Attenuation of MFD versus penetration depth.

3.4 Magnetic field control

3.4.1 Magnetic field control using eDMP

Fig 3.11 shows that the magnetic field in the desired ROI is controlled by a set of EMs located at its circumference. Without loss of generality, the ROI can take any shape, but the circular ROI is considered for illustration. Similar to the eDMP method for the EMs, the method can be applied to control the desired magnetic field $\mathbf{B}_{\mathrm{d}}$ in the ROI with a radius R_{ROI}. The magnetic field $\mathbf{B}_{\mathrm{d}}$ is computed at a number of positions discretized in the ROI. The method initially applied to characterize the field in the ROI as a single dipole and then, for the detailed shape of the EM, the eDMP model have been fully applied based on the orientation and current inputs of each single dipole.

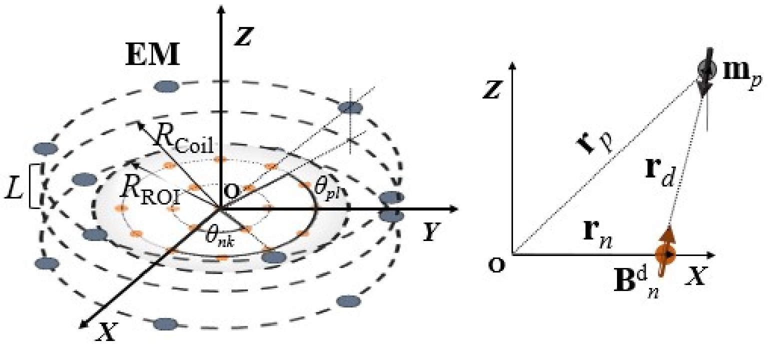

Fig. 3.11. Concept of magnetic field control.

For the circular ROI, position of the desired magnetic field in the ROI is set radially and uniformly, and the position $\mathbf{r}_{nk}$ of a k^{th} point on the n^{th} layer is expressed in accordance to (3.11):

$$\mathbf{r}_{nk} = [R_{nk}\cos\theta_{nk} \quad R_{nk}\sin\theta_{nk} \quad 0]^{\mathrm{T}} \tag{3.11}$$

where $R_{nk} = R_{\mathrm{ROI}}n/N_n$, $\theta_{nk} = 2\pi k/k_n$, $n=0,1,2,..,N_n$, $k=1,2,..,k_n$, and $k_n=N_k n$. In addition, N_n is the number of layers, k_n is the number of points on the n^{th} layer, and N_k is the number of points on the first layer.

N_n, k_n, and N_k, can be chosen as many as possible to describe adequately the desired field, considering too large number can make computation slow.

Similarly, the position $\mathbf{r}_{pl}$ of $\mathbf{m}_{pl}$ with a radius R_{EM} and a height from $-Lp$ to Lp, is expressed in accordance to (3.12):

$$\mathbf{r}_{pl} = [R_{\mathrm{EM}}\cos\theta_{pl} \quad R_{\mathrm{EM}}\sin\theta_{pl} \quad \pm(Lp)]^{\mathrm{T}} \tag{3.12}$$

where $$\theta_{pl} = \begin{cases} 2\pi(l-1)/N_l & (\mathbf{r}_{pl,z} = +(Lp)) \\ 2\pi(l-1)/N_l + \pi/N_l & (\mathbf{r}_{pl,z} = -(Lp)) \end{cases}$$

$p=1,2,..,N_p$, and $l=1,2,..,N_l$. Moreover, N_p is the number of layers, and N_l is the number of EMs on the p^{th} layer. The radius R_{EM} can be set as a constant, as close to the given ROI, since increasing the strength of the field from EMs using the input current is limited in practice due to heat on the EMs.

The magnetic field $\mathbf{B}$ generated from the dipole moment $\mathbf{m}_{pl}$ is computed in (3.13), and $\mathbf{m}_{pl}$ could be determined to control $\mathbf{B}$ as $\mathbf{B}_{\mathrm{d}}$.

$$\begin{bmatrix} \mathbf{B}_0 \\ \mathbf{B}_{11} \\ \vdots \\ \mathbf{B}_{N_nN_k} \end{bmatrix} = \mathbf{P} \begin{bmatrix} \mathbf{m}_{11} \\ \vdots \\ \mathbf{m}_{N_pN_l} \end{bmatrix} \tag{3.13}$$

$$\mathbf{P}_{nk,pl} = \frac{\mu_0}{4\pi d^5} \begin{bmatrix} (3x^2-d^2) & 3xy & 3xz \\ 3xy & (3y^2-d^2) & 3yz \\ 3xz & 3yz & (3z^2-d^2) \end{bmatrix} \tag{3.13a}$$

where $\mathbf{r}_d = \mathbf{r}_{nk} - \mathbf{r}_{pl}$ and $d = \|\mathbf{r}_d\|$.

Minimizing both the sum of errors in (3.15) and the maximum error in (3.16) ensures that the magnetic field at a specific location of the ROI can be controlled.

$$E_{nk} = w_{nk}\left\|\mathbf{B}_{\mathrm{d}nk} - \mathbf{B}_{nk}\right\| \tag{3.14}$$

$$\sqrt{\sum_{n=0}^{N_n}\sum_{k=1}^{k_n} {E_{nk}}^2} < E_{\max} \tag{3.15}$$

$$\max\left(E_{nk}\right) < E_{\infty} \tag{3.16}$$

where $E_{\max}$ is the given maximum sum of error in the ROI, E_{∞} is the maximal local error, and w_{nk} is an error weight function (initially set as 1). Smaller w_{nk} reduces the weight of the error at $\mathbf{r}_{nk}$.

In general, the desired magnetic field is a continuous field, but here it is discretized as a finite number of positions for computation. Thus, a discretization error may cause undesired fluctuation in the estimation of the magnetic field $\mathbf{B}$. It can be minimized by imposing a gradient magnetic field in (3.17) to compensate the error due to the discontinuity of the desired magnetic field, and reduce fluctuation in the field. The magnetic field thus becomes smooth and converges to the desired field

$$\left\|\nabla\mathbf{P}[\mathbf{m}]\right\| \le \left\|\nabla\mathbf{B}\right\|_{\max}. \tag{3.17}$$

$$\nabla \mathbf{P} = \frac{-3\mu_0}{4\pi d^7}\begin{bmatrix} 5x^3 - 3xd^2 & 5x^2y - yd^2 & 5x^2z - zd^2 \\ 5x^2y - yd^2 & 5xy^2 - xd^2 & 5xyz \\ 5x^2z - zd^2 & 5xyz & 5xz^2 - xd^2 \\ 5x^2y - yd^2 & 5xy^2 - xd^2 & 5xyz \\ 5xy^2 - xd^2 & 5y^3 - 3yd^2 & 5y^2z - zd^2 \\ 5xyz & 5y^2z - zd^2 & 5yz^2 - yd^2 \\ 5x^2z - zd^2 & 5xyz & 5xz^2 - xd^2 \\ 5xyz & 5y^2z - zd^2 & 5yz^2 - yd^2 \\ 5xz^2 - xd^2 & 5yz^2 - yd^2 & 5z^3 - 3zd^2 \end{bmatrix} \tag{3.17a}$$

$$\nabla \mathbf{B} = \begin{bmatrix} \frac{\partial B_x}{\partial x} & \frac{\partial B_x}{\partial y} & \frac{\partial B_x}{\partial z} & \frac{\partial B_y}{\partial x} & \cdots \\ \frac{\partial B_y}{\partial y} & \frac{\partial B_y}{\partial z} & \frac{\partial B_z}{\partial x} & \frac{\partial B_z}{\partial y} & \frac{\partial B_z}{\partial z} \end{bmatrix}^{\mathrm{T}} \tag{3.17b}$$

In addition, the strength of a dipole moment cannot be larger than the strength at the maximum current owing to the limited input current to the EMs as

$$\|\mathbf{m}\| \le \|\mathbf{m}\|_{\max} . \tag{3.18}$$

The error in (3.14) can be minimized through (3.19-21) iteratively. The h^{th} error $\Delta\mathbf{B}^h$ between $\mathbf{B}_d$ and the field $\mathbf{B}^h$ is computed in (3.19) to be compensated by the $\Delta\mathbf{m}^h$ in (3.20). Then the $(h+1)^{th}$ dipole moment, $\mathbf{m}^{h+1}$, can be determined in (3.21) and recursively computed as $\Delta\mathbf{B}$ converges to the desired error in (3.15) and (3.16).

$$\Delta\mathbf{B}^h = \mathbf{B}_d - \mathbf{B}^h \tag{3.19}$$

$$\mathbf{P}\Delta\mathbf{m}^h = \Delta\mathbf{B}^h \tag{3.20}$$

$$\mathbf{m}^{h+1} = \mathbf{m}^h + \Delta\mathbf{m}^h \tag{3.21}$$

The magnetic field in (3.13) satisfying (3.15-17) can be refined by increasing the number of EMs and current inputs. However, this may be difficult to achieve due to practical limitations in computation. The eDMP model is furthermore applied to account for the shapes and sizes of the EMs to enhance accuracy and controllability under the limited input current. The entire procedure used to control the magnetic field by a set of EMs is summarized in Fig. 3.12.

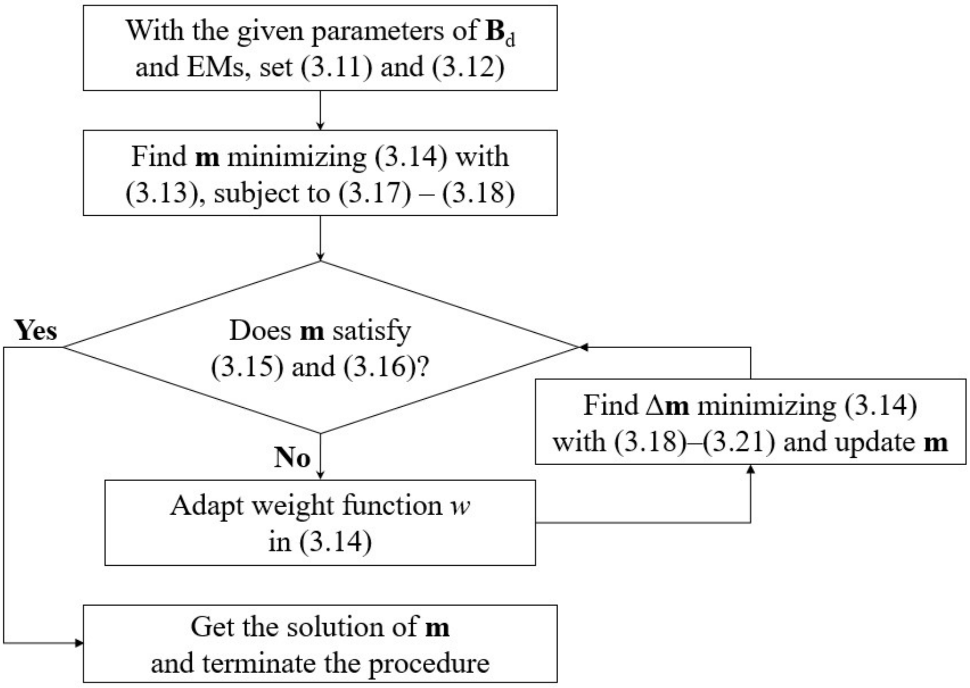

Fig. 3.12. Computational algorithm for magnetic field control.

3.4.2 Experimental validation

Three different magnetic fields are controlled by the set of EMs in the circular ROI: (i) uniform B_z along the z-axis of the entire ROI, (ii) uniform B_r along the radial axis of the entire ROI, and (iii) uniform B_z along the z-axis in half area of the ROI. The experimental testbed shown in Fig. 3.13 (a) is made of nonmagnetic conducting materials and a number of EMs, it is shielded to avoid the external interference. The ROI is placed in accordance to the predetermined parameters in Table 3.6. Fig. 3.14 (b) shows the EM energized by Li-ion 18650 batteries for a current supply. The input current is limited to 1.2 A due to the heat dissipation capacity of the EM. Table 3.7 shows the strength of the desired magnetic field within the ROI, considering the controllable range under the current limit. For case (iii), B_z is generated in the half of the ROI in S1 and the zero field in the other region S2.

Table 3.6. Geometric parameters

R_{ROI} (cm)	4.5	r_{in} (cm)	0.3
$[N_n, N_k]$	[3, 8]	r_{out} (cm)	1.3
R_{EM} (cm)	6.0	h (cm)	0.5
L (cm)	3.0	Number of EMs	36
$[N_p, N_l]$	[3, 6]	Maximum current (A)	1.2

Table 3.7. Desired Field Strength (μT)

Model	Uniform B_z	Uniform B_r	Half B_z

			S1	S2
B_z	50	0	13	0
B_r	0	50	0	0

Fig. 3.13 (c) shows the positions to control a desired magnetic field in the ROI, and the EMs similarly on the circumference of the ROI. Magnetic dipoles for the EMs in the simulation are interactively computed from (3.13)–(3.21). In the case of a uniform field, the error is small enough without the necessity for iterations, but for half the field in the case (iii), the error decreases and converges to 38 μT in the *4th* iteration, as shown in Fig. 3.13 (d). Unlike the uniform field, the intensity of the magnetic field along its discontinuity causes large error due to mathematical singularity. Thus, weighting *w* can be set to zero to avoid the singularity.

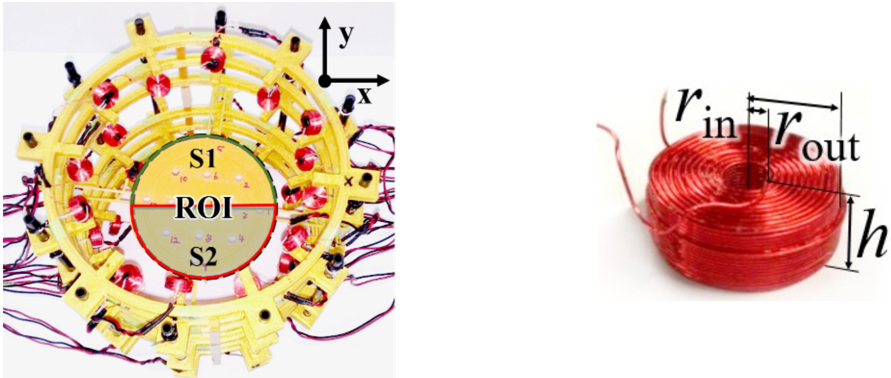

(a) Magnetic field controller (b) constructed coil

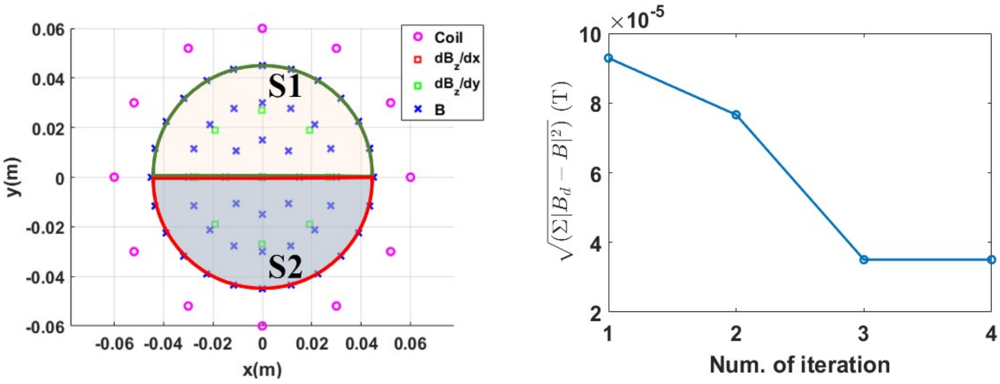

(c) Geometry (d) Error plot

Fig. 3.13. Setup for magnetic field control.

The EMs for the experiment are set based on the simulation. The sensor is initially calibrated to cancel a constant bias including Earth magnetic field. Controlled magnetic fields for both simulation and experiments are compared in Fig. 3.14.

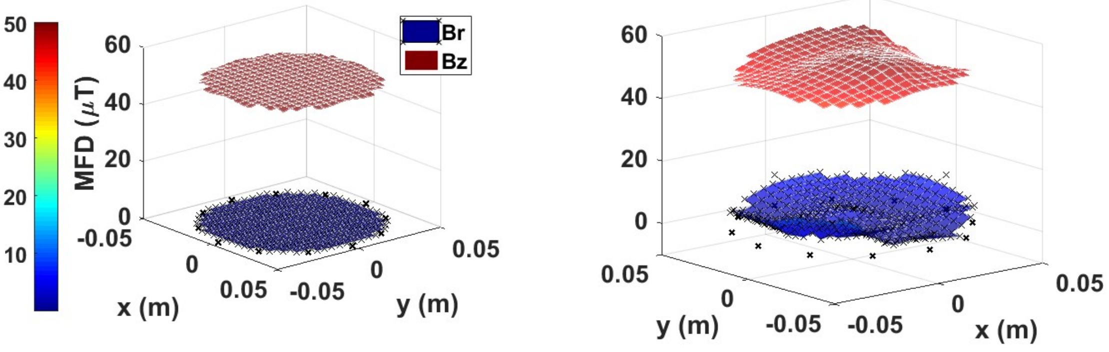

(a) Uniform B_z simulation (b) Experimental result

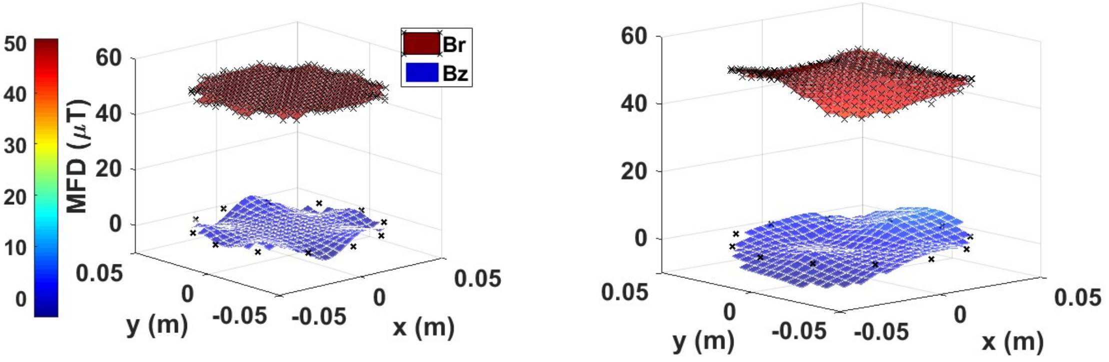

(c) Uniform B_r simulation (d) Experimental result

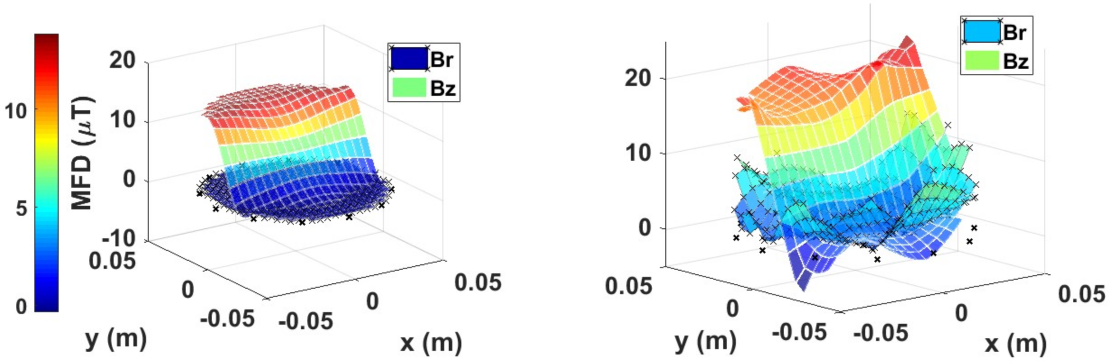

(e) Half B_z simulation (f) Experimental result

Fig. 3.14. Results of magnetic control.

The resultant magnetic fields are statically analyzed based on their mean, standard deviation of the entire field, maximum discrepancy and relative error, as detailed in Table 3.8. The standard deviation indicates the uniformity error of the field. The relative error of each experiment is computed as ratio of average discrepancy to the desired field, as (3.22).

$$\text{Relative error}(\%) = \frac{\text{mean}\left(\left|\mathrm{B}_i^{\text{exp}} - \mathrm{B}_i^{\text{des}}\right|\right)}{\left|\mathrm{B}_i^{\text{des}}\right|} \qquad (i = r, z) \qquad (3.22)$$

Table 3.8. Analysis for the control experiments

Model		Uniform B_z		Uniform B_r		Half B_z			
Figure		(a)	(b)	(c)	(d)	(e)		(f)	
						S1	S2	S1	S2
Average (μT)	r	0.11	4.2	50	49	0.15	2.0	4.1	3.4
	z	50	52	0.93	3.9	12	1.1	18	2.3
Standard deviation (μT)	r	0.11	1.9	0.41	1.8	0.15	0.12	2.2	2.3
	z	0.21	2.1	0.92	1.7	1.6	1.6	2.4	2.5
Maximum discrepancy (μT)	r	0.34	7.0	2.0	7.3	0.68	0.66	13	11
	z	1.1	5.9	3.9	8.3	4.6	4.9	10	12
Relative error (%)	r	*N/A*	*N/A*	0.34	3.4	*N/A*	*N/A*	*N/A*	*N/A*
	z	0.75	4.8	*N/A*	*N/A*	8.5	*N/A*	35	*N/A*

**N/A means 'not applicable' due to zero desired field in denominator*

Experimental results yield standard deviations in the range of 1–3 μT, while simulations yield 0.11, 0.21, 0.41 and 0.92 μT, in Fig. 3.14 (a) and (c). It is expected that the measurement error of the sensor itself could be affected since the Gauss meter used for the measurements has a 2 μT resolution. In addition, other uncertainties such as alignment of the EM position and orientation between the simulation and experiment, cause differences in the magnetic field. Fig. 3.14 (f) shows that S2 yields a maximum standard deviation of 2.5 μT, and S1 yields a maximum discrepancy of 13 μT. The error is dominantly caused by the discontinuity of the desired magnetic field. Furthermore, the discrepancies of each of the models have similar scales for both the B_r and B_z fields since the total magnetic flux of the experiments is same as in simulations. Variation of one component of the magnetic field directly affects other components. Comparison of the magnetic field distributions yields a good agreement indicating that the magnetic field is controllable.

3.4.3 Illustrative application: Capsule endoscope

Magnetic locomotion of a capsule is generally designed with PMs operating within the external magnetic field. The ability to manipulate the magnetic locomotion is verified in two cases: (i) rotation along the z-axis, and (ii) translation along the x-axis. Fig. 3.15 (a) and (b) shows the design of the PM capsule, comprising two cylinder PMs with M = 1.0 T that are enclosed with polystyrene. Fig. 3.15 (c) and (d) show the EMs and the ROI in the controller. The parameters of the ROI, the EM and capsule are listed in Table 3.14. The capsule is placed on the water surface since its locomotion can be observed clearly in that case. This design allows it to float on the water surface and move easily. Fig. 3.15 (e)-(f) show the corresponding magnetic field. The magnetic field in Fig. 3.15 (e) describes uniform B_x for rotation along the z-axis. In Fig. 3.15 (f), it has a uniform gradient $\partial B_x/\partial x$ used for translation along the *x*-axis. In Fig. 3.15 (f), numerous errors occur due to lack of a sufficient number of EMs, but gravity and buoyancy forces can cancel out locomotion due to B_z.

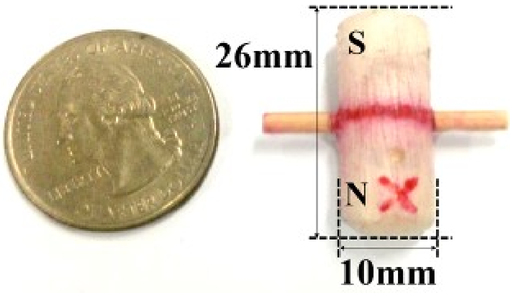

(a) Constructed PM capsule

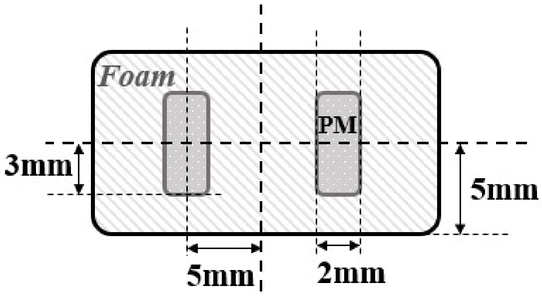

(b) Corresponding design

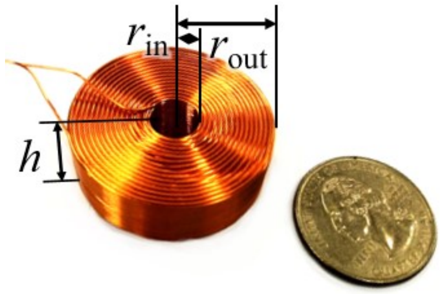

(c) Photograph of the constructed coil

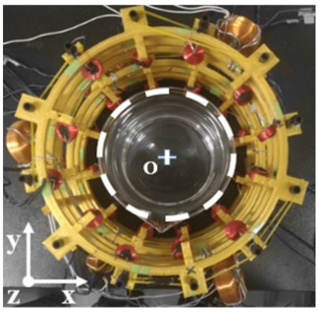

(d) ROI in a controller

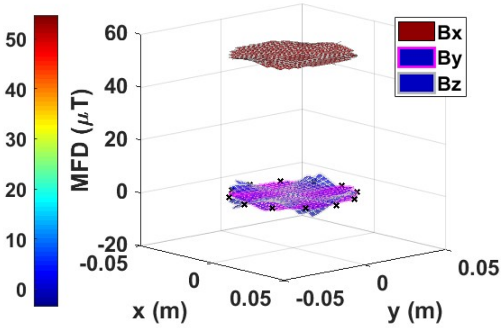

(e) Uniform B_x

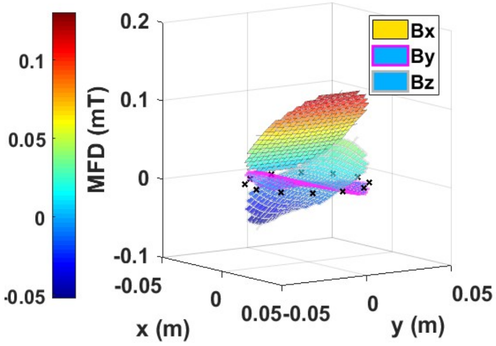

(f) Uniform $\partial B_x/\partial x$

Fig. 3.15. Setup for locomotion control.

Table 3.9. Magnetic locomotion geometry

R_{ROI} (cm)	3.0	r_{in} (cm)	0.375
$[N_n, N_k]$	[2, 4]	r_{out} (cm)	1.6
R_{EM} (cm)	8.0	h (cm)	0.5
L (cm)	4	Number of EMs	6
$[N_p, N_l]$	[1, 3]	Maximum current (A)	2.5
m (g)	0.754	J (g·cm^2)	0.838
c_F (g/s)	0.754	c_T (g·cm^2/s)	0.608

Dynamics of the capsule can be expressed as two degrees of freedom motion in (3.23) and (3.24) for translation and rotation, respectively. Force **F** and torque **T** acting on the PMs by the external magnetic field can be computed using the eDMP model. Dipole moments of the PMs, $\mathbf{m}_{PM}$, can be computed as [10].

$$m\ddot{x} + c_F \dot{x} = \mathbf{F} = \mathbf{m}_{PM} \cdot \nabla \mathbf{B}_{EM} \tag{3.23}$$

$$J\ddot{\theta} + c_T \dot{\theta} = \mathbf{T} = \left(\mathbf{m}_{PM} \times \mathbf{B}_{EM}\right) + \left(\mathbf{r}_{PM} \times \mathbf{F}\right) \tag{3.24}$$

where J is moment of inertia; m is mass; $\mathbf{r}_{PM}$ is position of the capsule. c_T and c_F are damping constants estimated by the experiments. All parameters are given in Table 3.9.

Fig. 3.16 shows the experimental result to control the magnetic capsule for orientation and position respectively. In Fig. 3.16 (a), the orientation along the z-axis is controlled by the uniform magnetic field B_x and the capsule is pointed to the desired axis in the ROI. In Fig. 3.16 (b), the position of the capsule is controlled and translated along the x-axis by the uniform gradient magnetic field $\partial B_x/\partial x$. Fig. 3.16 (c)-(f) show simulations and experimental results of angle, displacement, angular acceleration and acceleration respectively. Experimental errors with respect to simulation are 5.4, 1.7, 22, and 1.6 % and are caused by various experimental uncertainties including water drag, EMs and magnetic field. However, it is shown that the eDMP method for the control can be applied to achieve magnetic locomotion by generating the required magnetic field.

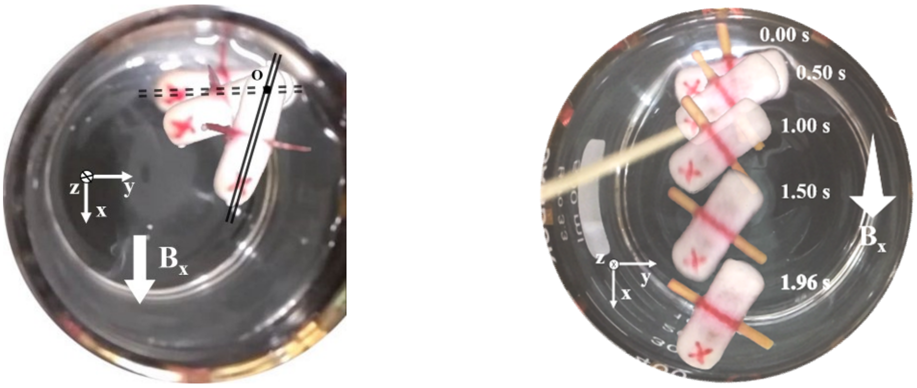

(a) Rotation control along the x-axis

(b) Translation control along the x-axis

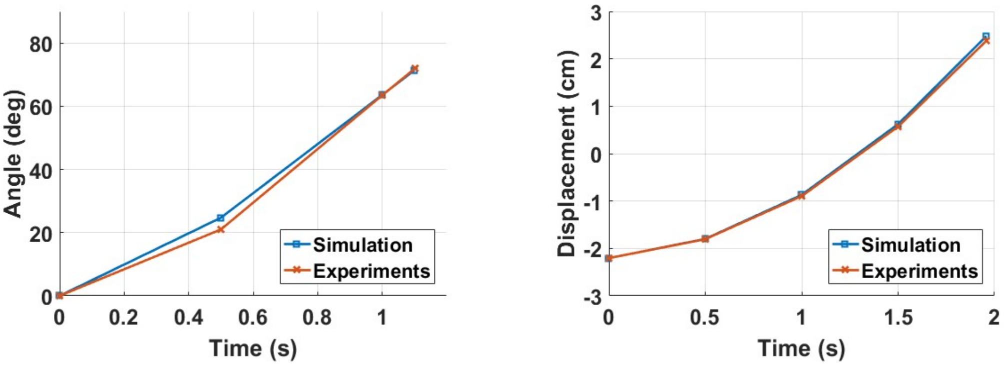

(c) Angle

(d) Displacement

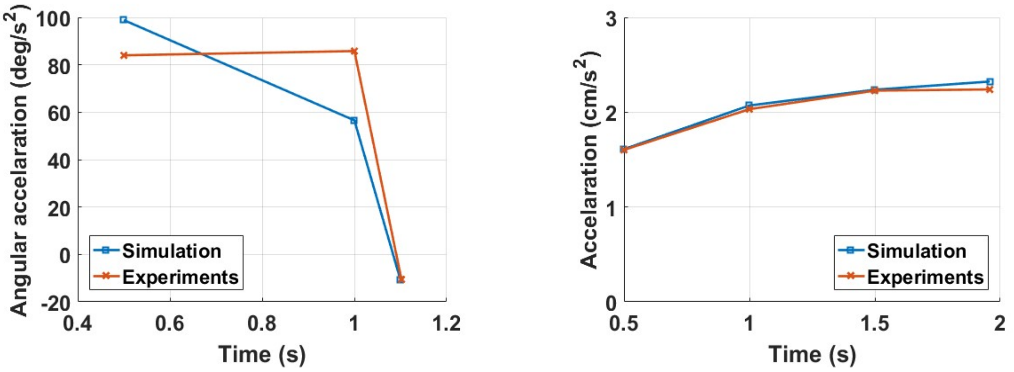

(e) Angular acceleration (f) Acceleration

Fig. 3.16. Motion of capsule.

3.5 Discussion

In this research, a novel method to actively control magnetic field in a region-of-interest is presented with the eDMP method for a number of EMs. The eDMP method is applied to characterize the magnetic field from EMs and control the magnetic field in the ROI. Position, orientation, and strength for a set of the EMs are determined to satisfy the desired magnetic field. Modeling and controllability are validated through the comparison of simulation and experimental results for various models. It is shown that the magnetic field can be controlled. Furthermore, TMS and magnetic locomotion as practical applications have been utilized to prove applicability of the method. The performance of each of the TMS coils is analyzed by the eDMP method. In addition, magnetic locomotion is illustrated through the experiments for both translation and rotation control. Usefulness and accuracy of the eDMP method and controllability of the magnetic field have been demonstrated. The method is expected to be applied to develop various magnetic applications.

4. Voice coil navigation sensor

4.1 Overview

In this chapter, a novel navigation sensor based on voice coils is proposed for an intubation tube. The navigation sensor comprises many sets of an exciter and sensors using a voice coil to measure the orientation and position. As the coils are wound along the intubation tube with thin layer, can be inserted in the human body. The curved path of the inserted tube can be reconstructed in real-time by measuring variance of the magnetic field due to bending of each tube segment. Design parameters of the sensor, including design of both exciter and sensor, geometry between two coils, can be analyzed to achieve the enhanced performance. Computing mutual inductance of various shaped coils with specific geometric relations has been studied in [56] and many detailed problems in [57-59] have been analyzed. Computation process for mutual inductance requires to solve series of integral operations for various positions, orientations and shapes of coils and takes a lot of computational effort. The extended distributed multi-pole (eDMP) method is developed to characterize the time-varying field and compute the mutual inductance, since it is a semi-analytical method capable of fast computing [55]. Then, the method is utilized to design a navigation sensor as a guidance of flexible intubation tube and investigates the design parameters for optimal performance. The proposed sensor is validated by comparing with experiments and further applied to measure the curve in throat.

4.2 Magnetic field analysis

4.2.1 Design concept

A navigation sensor should be designed considering a tube shape for intubation procedure. Fig. 4.1 shows the design concept of the voice coil navigation sensor for a flexible tube. A set of excitation coils (EX-N) and sensing coils (S-N) are wound alternately along the tube. Excitation and the sensing coils have different designs; the excitations are axis-symmetric cylinder coils, perpendicular to the tube; the sensing coils are inclined and two sensing coils are symmetrically wound at the same location of the tube. As alternative current input is applied to the excitation coils, time-harmonic magnetic field is generated along the tube. Consequently, the voltage is induced in each sensing coils. As the tube is straight in Fig. 4.1 (a), two sensing coils are symmetric and have the same induced voltages. Whereas, once the tube is bent in Fig. 4.1 (b), the induced voltages are different. Then, the bending angle of the flexible tube can be computed by measuring the difference between the two induced voltages and symmetric bending angle can be distinguished. The entire path of the tube can be reconstructed by utilizing a number of sets of the excitation coils and the sensing coils. Furthermore, two orthogonal orientations, pitch and yaw rotation in three-dimensional space, can be measured individually by wounding sensing coils orthogonally. As the tube is smoothly bent and the distance *l* between the two neighboring excitation coils is small, it is reasonable to assume that each curvature C-1, 2,…, N between the neighboring coils is a constant as an elementary curve. The orientation based on a sensing signal from each sensor, S-1, 2, ..., N can be determined by the curvature. Furthermore, the whole tube path can be reconstructed by inverse kinematics, with the curvature information from each sensing coil and their locations from the elementary curve length *l*.

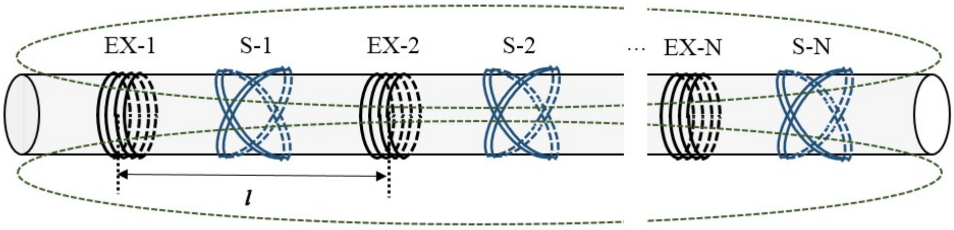

(a) Straight tube

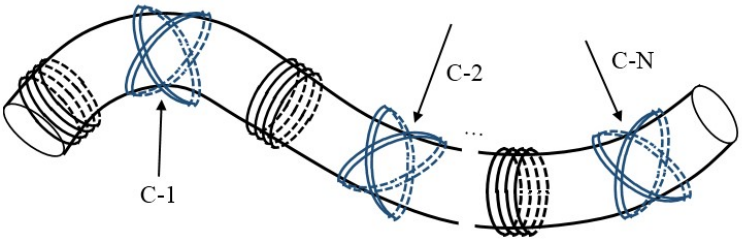

(b) Tube with bending

Fig. 4.1. Concept of navigation sensor.

4.2.2 Magnetic field modeling

The induced voltages in the sensing coils and the variance of the mutual inductance as the bending angle changes should be analyzed to enhance the sensing performance. The eDMP model can be applied to modeling the coils and compute a mutual inductance between two coils in real time, considering their relative positions and orientations [55]. Axis-symmetric cylinder coils has been already discussed in the previous chapter 3, and here the inclined sensing coils is analyzed. Fig. 4.2 shows the geometry of the inclined coil with angle β and the eDMP model (red dots). The inclined cross-section of the coil is an ellipse with major axis r_1 and minor axis r_2, length is L. Considering its asymmetric geometry, the eDMP model has the modeling parameters r_{m1}, r_{m2} and l_m, and the error in (3.5) is computed on both major and minor axis (blue dots). Then, the parameters, including the number of dipoles, could be determined through (3.1-3.6).

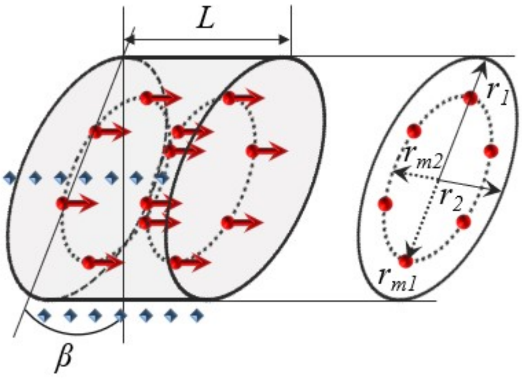

Fig. 4.2. Modeling scheme of an inclined coil.

Fig. 4.3 shows the eDMP model of a set of excitation and sensing coil along the bend tube. Coil *a* is excitation and coil *b* is sensing coil for measurement. The eDMP model of each coil is represented by the dipole moments **m** and dipole position **P**. The bending angle θ of the tube is expressed in the xyz coordinate. Once the modeling parameters are determined for the coils, the mutual inductance can be computed, and the induced voltage generated in the coil *b* by the coil *a* can be expressed in (4.1). Furthermore, the mutual inductance with respect to the bending angle θ is linearized as (4.2) and θ can be computed from the voltage measurement in real time. The detailed linearized model can be derived in Appendix.

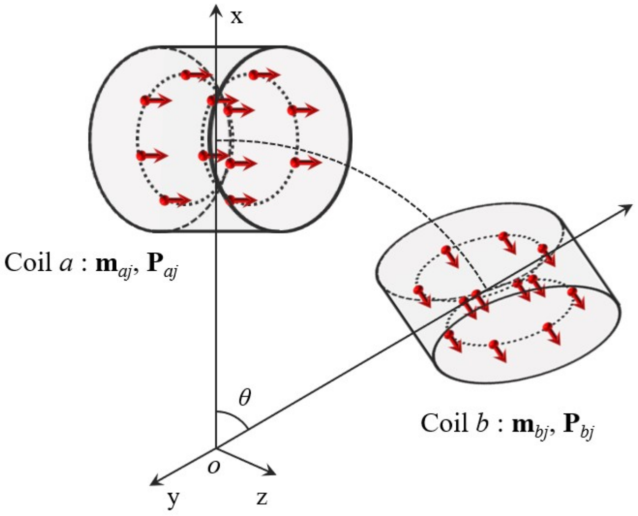

Fig. 4.3. Mutual inductance between two coils.

$$V_b = \frac{dI_a}{dt} M_{ab} = j\omega I_a \sum_{j=1}^{N_a} \left(\frac{1}{I_a I_b} \mathbf{m}_{bj} \sum_{i=1}^{N_b} \mathbf{B}_{ai} \right) \tag{4.1}$$

$$M_{ab}(\theta) = M_{ab}(\theta_0) + \left.\frac{dM_{ab}}{d\theta}\right|_{\theta=\theta_0} \theta \qquad (4.2)$$

where M_{ab} represents the mutual inductance between coil a and coil b; I_a and I_b represent the input current in coil a and b; ω is operating angular frequency of I_a; N_a and N_b represent the dipole number of the eDMP model for the coil a and b; θ_0 is a reference orientation angle without any bending.

4.2.3 System design

The induced voltage in (4.1) depends on various geometric design parameters such as the length of the coils, L and L_b, the distance l between the coils and diameter D of the coils, as shown in Fig. 4.4. The design and geometry of the coils should be optimized considering practical usage to achieve better performance. A length of the coil is determined by the number of turns. The excitation field is proportional to the number of turns of the exciter and decreasing the number of turns reduces the excitation field. Then, the sensing performance would be degraded. However, the coil length should be limited to preserve the flexibility of the tube.

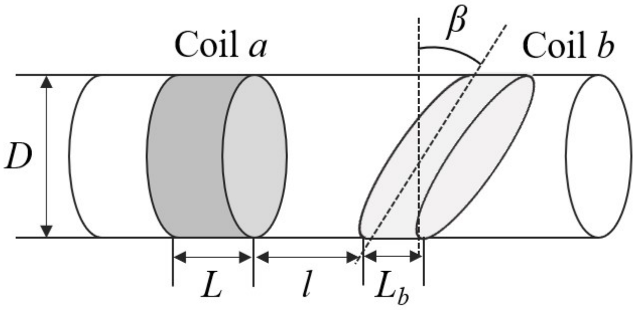

Fig. 4.4. Design parameters of proposed sensor.

The geometry of the excitation coil and the distance between two coils affect the induced signal in a coupling way, since a magnified coil set will induce the exact same signal at a distance magnified by the same degree. The geometric design parameters can be capsulized by two ratios in (4.3) and (4.4).

$$\lambda = \frac{D}{L} \qquad (4.3)$$

$$\kappa = \frac{l}{D} \qquad (4.4)$$

where diameter D would be constant since the tube diameter is usually pre-determined by its specific application. Under the thin layer coil assumption, aspect ratio λ solely accounts for the coil shape. By multiplying λ and κ, the relation between L and l can be examined to decide whether the elementary sensor set is too long for the tube to be practically bent.

To characterize the sensing performance, resolution S and linearity γ of the mutual inductance in terms of the tube bending angle θ are defined in (4.5) and (4.6).

$$S = Ave(\frac{dM}{d\theta}) \tag{4.5}$$

$$\gamma = Std(\frac{dM}{S}) \tag{4.6}$$

where the resolution S and linearity γ are calculated as the average and standard deviation of discrete sensitivity terms respectively. The resolution should be maximized while the linearity is minimized to optimize the sensing performance.

4.3 Model simulation

4.3.1 Modeling of an inclined angle

The eDMP method for the inclined coil is numerically simulated and validated against other methods. The coil is wound around a 5 mm diameter tube with 60 deg inclination. The analytical solutions and numerical results using commercial software COMSOL are used to compare with the simulation results of the eDMP method. The detailed parameters of the coil, eDMP and COMSOL are given in Table 4.1. The simulated fields for B_x and B_z in Fig. 4.5 are calculated at the locations with a radical distance of 2.6 mm from the tube axis and z coordinates ranged from zero to twice the coil length. B_y is close to zero due to symmetric shape. An INTEL quad-core desktop computer with 16G RAM and 3GHz CPU is used for computing the numerical solutions.

Compared with the numerical results from COMSOL, the eDMP model provides much smoother results and less computation efforts. When the 2z/*l* is smaller than one, it can be seen that the discrepancy between the analytical solutions and eDMP modeling results is bigger. This is due to the limited model of the exact coil boundary since these locations are only 0.1 mm away from the coil surface.

Table 4.1. Model parameters for an inclined coil

Coil geometry	L=8mm D=5mm $\beta = 60^\circ$
eDMP Model Parameters	$l_m = [2.6 \quad 4.2]mm$ $r_{m,1} = 2.5mm$ $r_{m,2} = 1.3mm$ $\lvert\mathbf{m}\rvert = [0.314e-4 \quad 0.609e-4]Am^2$
COMSOL parameters	Mesh shape: free tetrahedral Volume element quantity: 1369

	Volume mesh quality: 0.2634 Boundary element quantity: 29767 Boundary element quality:0.6733 Minimum size: 0.2mm

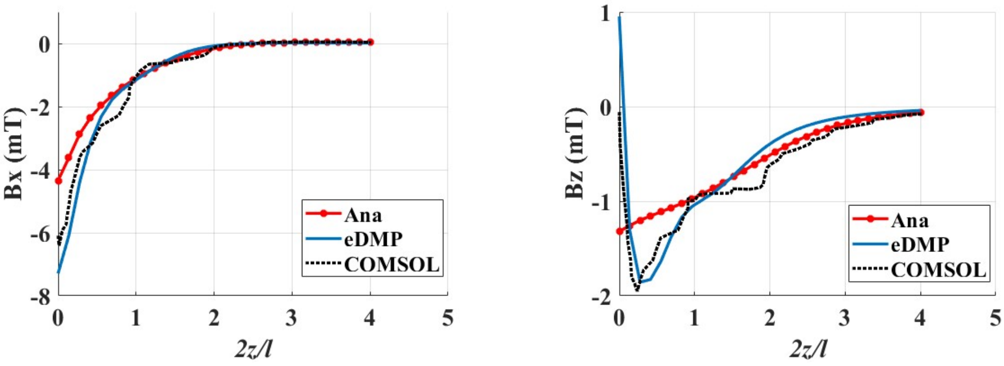

(a) B_x (b) B_z

Fig. 4.5. Magnetic field simulation of an inclined coil.

4.3.2 Design optimization

The various geometric design parameters have been simplified in Fig. 4.4 to be ratios λ, κ and the inclination angle β, while the tube diameter D is pre-determined by application. A nasogastric feeding tube with diameter 5 mm is used for demonstration. To examine the effect of inclination angle on the mutual inductance, the distance l between the excitation coil and sensing coil is set to be 2 cm and the coil length is set to be 0.8 cm. The inclination angle is considered as the sole design parameter. The simulation results of mutual inductance versus the bending angles are shown in Fig. 4.6, with the inclination angle β.

The results show that the relation between the mutual inductance and the bending angle is symmetric with respect to the zero-degree bending position. As the inclination angle varies, the mutual inductance with respect to the angle becomes linear. The slope increases with the inclination angle, indicating that better sensitivity can be expected for larger bending angles. The overall magnitude of the mutual inductance reduces as the bending angle increases, especially after the angle reaches 45 degree. This could cause a low signal-noise ratio and is susceptible to noise. Hence, the inclination angles, 45 degree and 60 degree are candidates for optimal design.

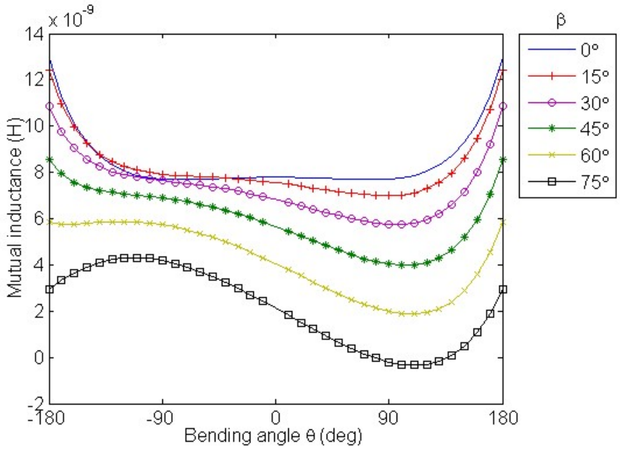

Fig. 4.6. Mutual inductance as inclination angle change.

Two sensing coils in a single sensor set are identical except the perpendicular inclination surfaces as shown in Fig. 4.1. Without loss of generality, only one coil is considered during the design optimization. Three main factors in design, including coil geometry, distance and inclination angle, are analyzed to examine their coupling effects on performance. Various lengths of the excitation coil are set to be 4 mm, 6 mm, 8 mm, 10 mm, and 12 mm for practical implementation. The excitation coil with even longer length may disturb insertion of the tube. The design parameters of the sensing coil are summarized in Table 4.2 and model parameters for the excitation coil are shown in Table 4.3.

Table 4.2. Summary of design parameters

D(mm)	5	κ	3:1/3:8
θ	$(-90^{\circ}:10^{\circ}:90^{\circ})$	β	45°,60°
λ	1.25, 0.83, 0.625, 0.5, 0.42		

For each combination of coils with different geometry, the mutual inductance with respect to the bending angle from -90 to 90 degree is computed. Linearity and resolution performance in (4.5) and (4.6) are shown in Fig. 4.7.

Table 4.3. Model parameters for coils with different geometry

λ	L(mm)	Coil a
0.42	12	$\lvert\mathbf{m}\rvert = 1.356e-4Am^2$, $l_m = 7.2mm$
0.5	10	$\lvert\mathbf{m}\rvert = 1.121e-4Am^2$, $l_m = 5.8mm$
0.625	8	$\lvert\mathbf{m}\rvert = 8.882e-5Am^2$, $l_m = 4.4mm$
0.83	6	$\lvert\mathbf{m}\rvert = 6.578e-5Am^2$, $l_m = 3.0mm$
1.25	4	$\lvert\mathbf{m}\rvert = 4.355e-5Am^2$, $l_m = 1.6mm$

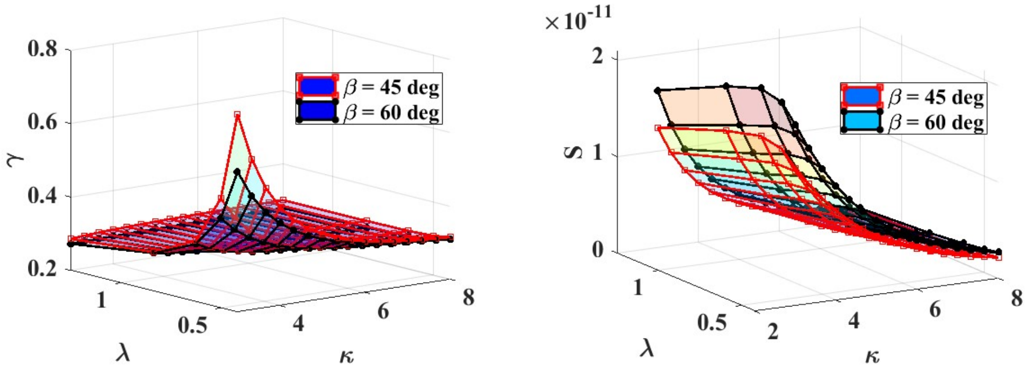

(a) Linearity (b) Resolution

Fig. 4.7. Effect of design parameters.

The linearity of the mutual inductance reaches its maximum at λ = 0.42 and κ = 3 regardless of the inclination angle, indicating that the sensor performance may not be good. It gradually decreases as λ and κ increase. The resolution with respect to the mutual inductance shown in Fig. 4.7 becomes maximum at λ = 0.625 and κ = 3, corresponding to L = 8 mm and l = 15 mm. The inclination angle at 60 degree provides even higher resolution with the same coil length and distance. In order to validate the optimal design, experiments are conducted and compared with a number of different designs.

4.4 Experiments and results

4.4.1 Experimental setup

The sensor set for experiments is shown in Fig. 4.8 and the operational electronics is shown in Fig. 4.9. The single excitation coil and two sensing sets are installed on a flexible tube. The magnetic field is generated from the excitation coil by input current 2 A with 400 KHz, originated in a voltage source and magnified by an operational amplifier in Fig. 4.9 (b). Differential amplifier in Fig. 4.9 (c) is used to amplify the difference between the two sensing coils. The two sensing coils, inclined in two perpendicular surfaces, are capable of detecting orientations in three-dimensional space based on the variations in induced voltage. Orientations of the tube can be verified by the circles with various diameters.

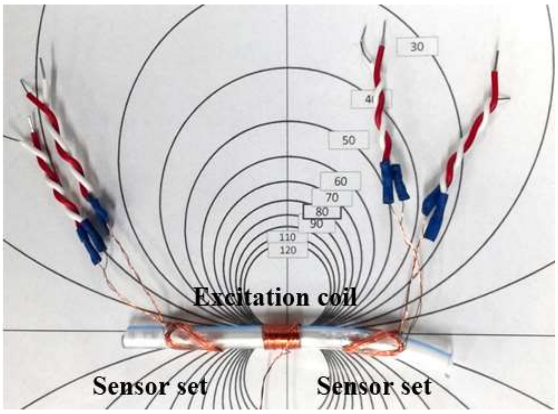

Fig. 4.8. Flexible tube with the sensor sets.

In order to enhance the performance of the navigation sensor, resolution for bending angle should be maximized. The resolution can be computed as a variation of induced voltage with bending angle change. The optimal design can be estimated considering design parameter and constraint. The design parameters of the system are length of coil *a* and *b*, distance between two coils and inclined angle *β*, as shown in Fig. 4.7. There are several design constraints: tube size and width of throat. In addition, flexibility of the tube should be maintained for operation.

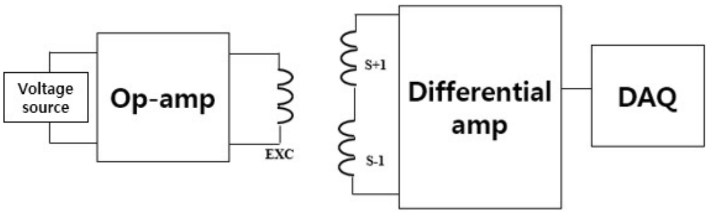

(a) Electrical diagram

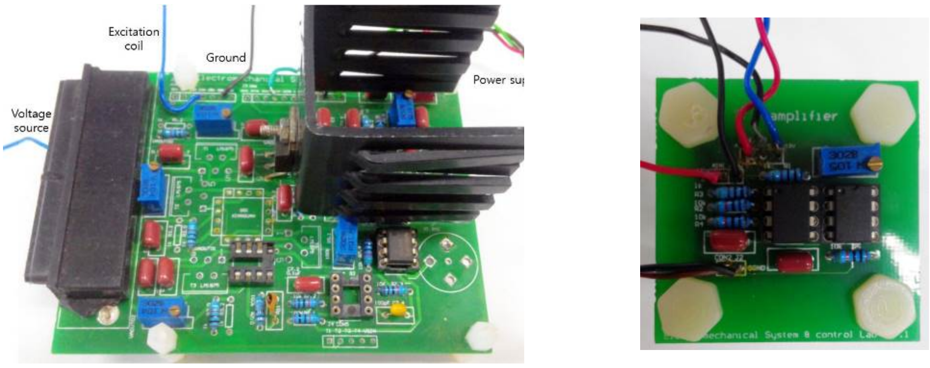

(b) Operational amplifier

(c) Differential amplifier

Fig. 4.9. Operational electronics.

Magnetic coupling between two overlapped sensing coils in the single sensor set should be examined before measuring the inductive signal. It is inevitable that one sensing coil need to be wound on top of the other sensing coil to measure all the orientation angles in three-dimensional space. However, this causes possible magnetic coupling with different geometries between the two sensing coils. When the bending of tube is conducted within the inclination surface of the inner coil, it is expected that the induced voltage in the inner coil is dominant compared to the outer coil. The effects of two overlapped coils on magnetic field coupling are simulated and compared to experimental results in Fig. 4.10 as the inner and outer coil are activated respectively. As the outer coil is activated, the variation of the outer and the inner coil is 3.59 mV and 0.07 mV. Similarly, when the inner coil is activated, the variation of the inner and the outer coil is 3.59 mV and 0.07 mV. The experimental results show the similar differences between the activated coil and the other: the variation of the outer coil is 3.97 mV when activated, while the variation of the inner coil is only 0.37 mV. It is worth mentioning that the outer coil always provides a bigger measurement due to its bigger cross-section area, unlike the modeling results. In addition, the bent coils could be one of the reasons for discrepancy. However, it can be assumed that the magnetic field interference due to the outer and inner coils is small and can be decoupled. The detailed results including the eDMP and experiments are summarized in Table 4.4.

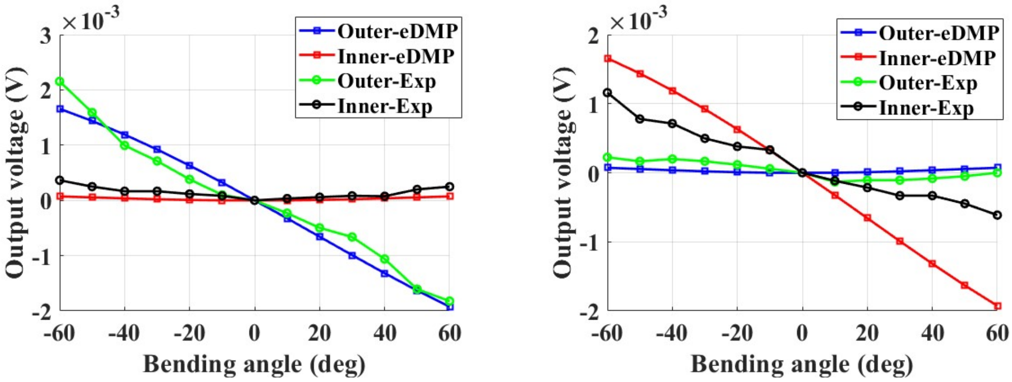

(a) Outer coil activated

(b) Inner coil activated

Fig. 4.10. Comparison of field coupling between the coils.

Table 4.4. Magnetic field interference between the coils

		Max	Min	Mean	Variation
Outer coil activated					
eDMP(mV)	Outer	1.66	-1.93	-0.05	3.59
	Inner	0.07	-0.00	-0.03	0.07
Exp.(mV)	Outer	2.15	-1.82	0.00	3.97
	Inner	0.37	0.00	0.14	0.37
Inner coil activated					
		Max	Min	Mean	Variation
eDMP(mV)	Outer	0.00	-0.07	-0.03	0.07

	Inner	1.66	-1.93	-0.05	3.59
Exp.(mV)	Outer	0.22	-0.13	0.03	0.35
	Inner	1.16	-0.61	0.14	1.77

4.4.2 Results and discussion

Performance of the navigation sensor with design parameters is numerically and experimentally demonstrated in the range of bending angle θ = -90°:10°:90°. Four design candidates, (Design A, B, C, and D) are considered with combination of various κ and β in Fig. 4.4. Experimental set-up and design parameters are summarized in Table 4.5.

Table 4.5. Experimental parameters

Design	A	B	C	D
κ (= l/D)	3	5	3	5
β (degree)	45	45	60	60
D (mm)	5			
λ (= D/L)	0.625			
Excitation current (A)	0.707 A_{RMS}, 400 kHz			

The experimental results are compared with the eDMP model and the COMSOL simulation in Fig. 4.11. The output voltage without any bending is calibrated as zero to remove a constant bias. Based on the experimental results, the 60 deg inclination shows more linear relation between the bending angle and the output voltage.

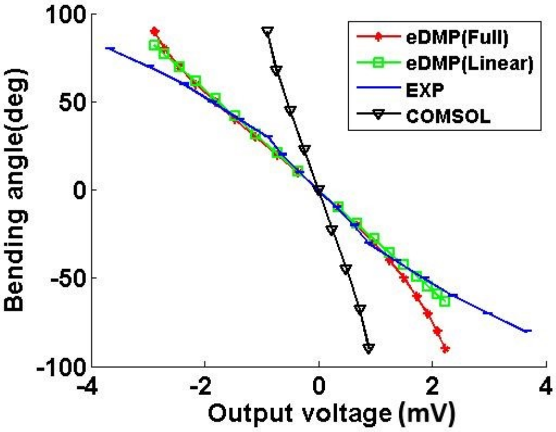

(a) Design A

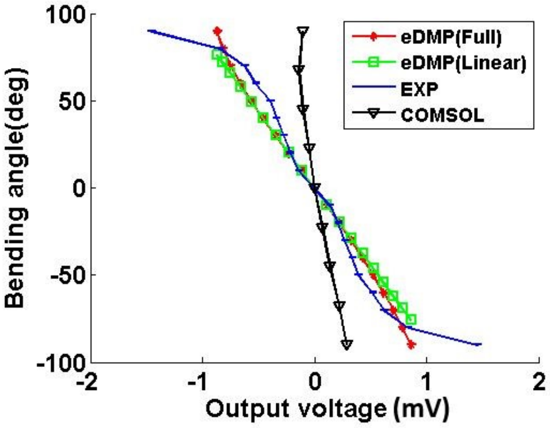

(b) Design B

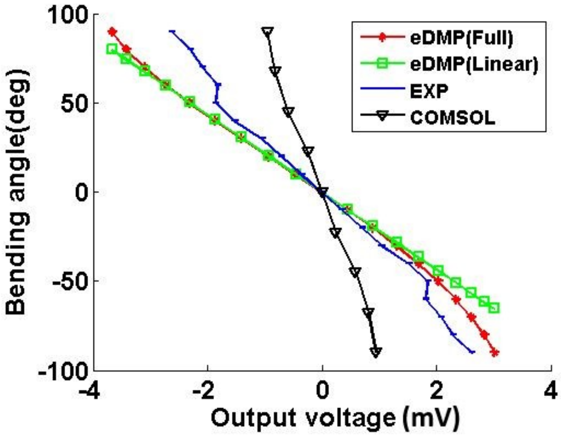

(c) Design C

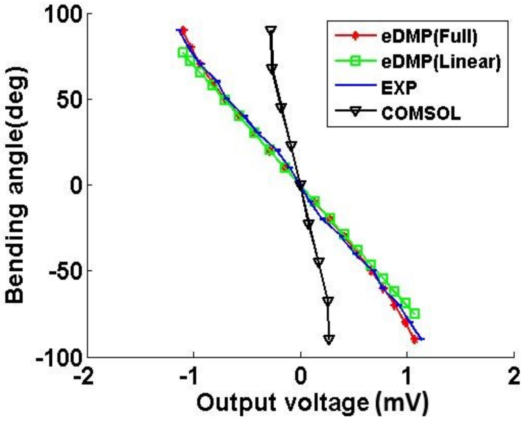

(d) Design D

Fig. 4.11. Comparsions of simulation and experimental results.

The error between the eDMP simulation results and experimental results can be computed as in (4.7). The maximum, minimum, and average errors in percentage and degrees with three times measurements are detailed in Table 4.6.

$$Error = \left| \frac{\theta_{eDMP} - \theta_{EXP}}{\theta_{eDMP}} \right| \tag{4.7}$$

Table 4.6. Error analysis

Design	Max		Min		Mean		Resolution *mv/deg*
	%	*deg*	*%*	*deg*	*%*	*deg*	
A	22.8	5.12	0.25	0.00	13.0	2.08	0.0352
B	42.5	13.8	5.15	0.00	21.1	4.36	0.0114
C	52.4	0.31	5.31	2.50	19.7	3.68	0.0459
D	54.7	0.66	0.94	0.04	20.4	2.75	0.0143

The maximum errors for each design occur at the bending angles, θ = 23.2, 32.6, -0.581, and -1.21 degree, and the minimum errors at 46.4, -15.8, -47.0, and 45.9 degree respectively. From the results, Design C offers the highest resolution, smallest absolute error of the angle in Max (even though the min is relatively large but it occurs at θ = -47 degree beyond the range of the operating region). In addition, the error and performance of Design C are investigated in more detail. The output voltages are measured while the bending angle ranges from -45 to 45 deg with every 5 deg as shown in Fig. 4.12. The maximum error is 1.19 deg at θ= -6.12. Figure 4.12 (b) shows the resolution of each method as the single sensing coil, computed from (4.3). The resolution of the linear model is a constant as 0.0919 mV/deg while the eDMP offers the maximum 0.0943 mV/deg at θ = 20 and the minimum 0.0732 mV/deg at θ = -40. Similarly, the experimental results show the maximum and the minimum as 0.1139 mV/deg at θ = 20 and 0.07 mV/deg at θ = 40 respectively. The experimental result shows fluctuation and asymmetry due to imperfection of the coil winding uncertainties in electronics. However, the resolution, in general, decreases as higher bending angle due to large bending and deformation of the coil.

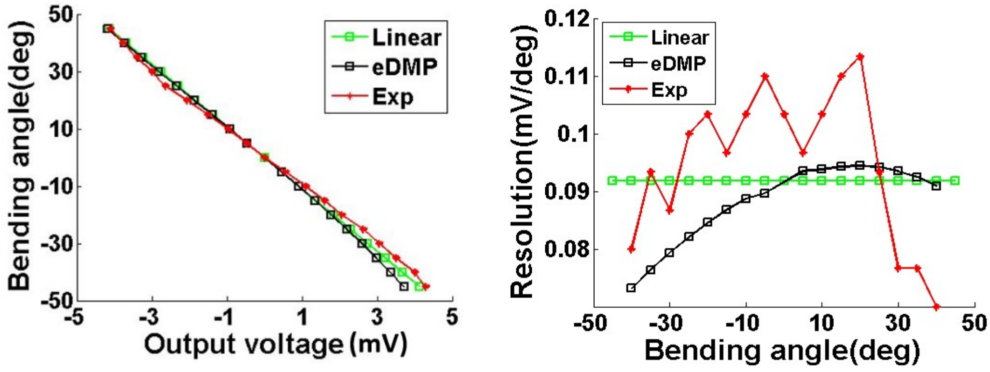

(a) Output voltage versus θ (b) Resolution versus θ

Fig. 4.12. Sensitivity for bending angle.

4.4.3 Application

Trajectory of a flexible nasogastric tube is demonstrated using an anatomy manikin as shown in Fig. 4.13 (a). Trachea and esophagus paths are abstracted using the NDI Aurora tracking device (NDI Medical, Canada). The overall length of the esophagus path from the nose to the area near lungs is 23 cm and that of the trachea is 22 cm. When the intubation device reaches the throat, the trachea bends towards the chest while the esophagus bends towards the back. The distance between them is about 2.5 cm, as shown in Fig. 4.13 (b), though distance could be slightly different from patient to patient. The navigation sensors in Fig. 4.14 are wound along the stomach tube with the length 20 cm. Five excitation coils are wound and four sensing coils are between the excitation coils. Each sensor set has a length of 4 cm. The reconstructed path is shown in Fig. 4.15, compared with the actual esophagus segment and trachea. Although the discrepancy between the actual and reconstructed intubation path increases with the intubation length, it is about 0.5 cm near the throat area and much smaller than the distance between the esophagus and trachea. The navigation sensor can be applied for preventing the tube from being mistakenly inserted into the trachea.

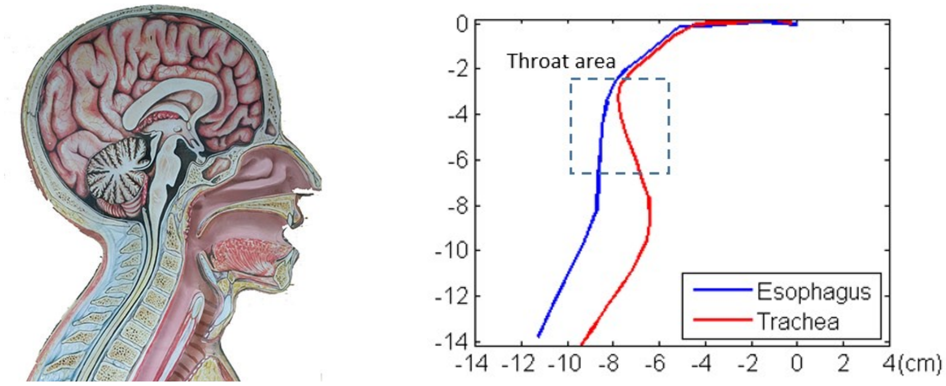

(a) Anatomy manikin (b) Intubation paths

Fig. 4.13. Intubation paths based on an anatomy manikin.

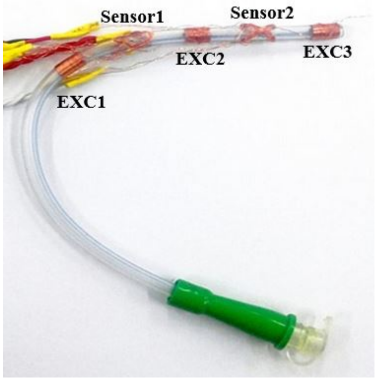

Fig. 4.14. Sensor sets on a flexible nasogastric tube.

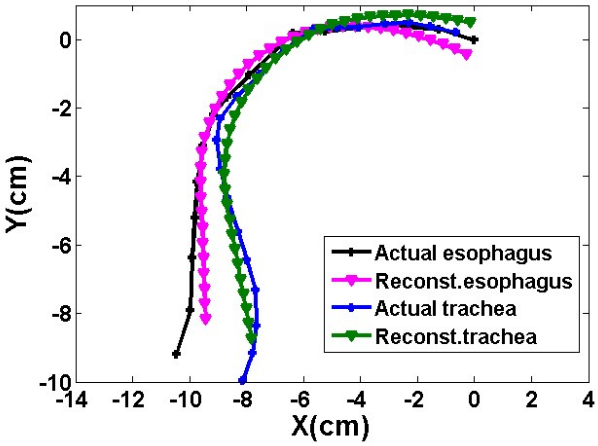

Fig. 4.15. Reconstructed path.

4.5 Discussion

In this research, a novel navigation sensor using the voice coil was presented and applied to guide the flexible intubation tube. A set of excitation coils and inclined sensing coils were wound along the tube and the induced voltage on the sensor was utilized to measure the curvature of the bent tube. The eDMP model was applied to modeling the coils and compute the mutual inductance between the coils. Based on the modeling, the effective design parameters were optimized to enhance the sensing performance, such as the resolution for the bending angle change. The eDMP method was validated by comparing with the numerical simulations and experiments. It presented that the eDMP method shows good agreement and the sensor design is optimized. Furthermore, the experiments demonstrated that the navigation sensor can distinguish the paths of trachea and esophagus. It indicated that the voice coil sensor is capable of navigating the intubation tube.

5. Magnetic induction tomography

5.1 Overview

In this chapter, a MIT system is analyzed by using the eDMP model and make image for the low conductivity objects. The fundamental of MIT is described by a term of dipole and validated by comparing with experiments. The system is implemented as electronics-level and applied to imaging various materials.

The eDMP method has been proposed to enhance accuracy in the near-field and compute the interaction between magnetic fields, such as magnetic induction, Lorentz force, and torque fast [52-54]. In this study, the eDMP method is applied to supplement the equivalent circuit model. The equivalent circuit modeling is applied to identify an entire system of the MIT using Z-parameters. Then, the eDMP can estimate the Z-parameters, considering the properties of the objects and system setup. Once forward modeling is constructed, an inverse algorithm can be developed. As the eDMP model based on the magnetic dipole moments takes less computational effort, the ill-posed condition can be compensated. Conductivity in the ROI can be determined by solving the inverse of phase shift and image processing can be achieved [60].

The experiments are performed to demonstrate the method is applicable to a MIT system. The object with uniform conductivity is applied as illustration and the effect of the object properties, the position, shape and conductivity, is studied since it requires high sensitivity for variation in the properties. Based on the results, the detailed sensitivity and resolution of the MIT system can be estimated. In addition, the imaging quality for characterization of the object properties, the position, shape and conductivity, is predicted. For the implementation, the phase domain transceiver system can be constructed.

5.2 Modeling using eDMP

5.2.1 Magnetic field of MIT

In Fig. 5.1, a pair of a k^{th} transmitter (Tx) coil ($k = 1, ..., N_k$) and a l^{th} receiver (Rx) coil ($l = 1, ..., N_l$) and conducting objects are shown for the illustration of the fundamental of MIT. The i^{th} object ($i = 1, ..., N_i$) has conductivity σ_i and permittivity ε_i. As the Tx coil generates time-harmonic magnetic flux density B_k (blue dashed line), the electric field E_i (green curved arrow) is induced in the i^{th} object and estimated as

$$\nabla \times \mathbf{E}_i = -\frac{\partial \mathbf{B}_k}{\partial t} = -j\omega \mathbf{B}_k \tag{5.1}$$

where $j^2 = -1$ and ω is the operating angular frequency.

The current I_i (green loop) which is caused by $\mathbf{E}_i$ and σ_i generates the secondary magnetic field $\mathbf{B}_i$ (green dashed line), whose phase is different from that of the primary field. The Rx coil can identify the phase shifted by the secondary field, and the phase shift depends on conductivity, relative orientation, and position among Tx, Rx, and the object. Thus, conductivity distribution in the ROI can be obtained by analyzing the phase shift.

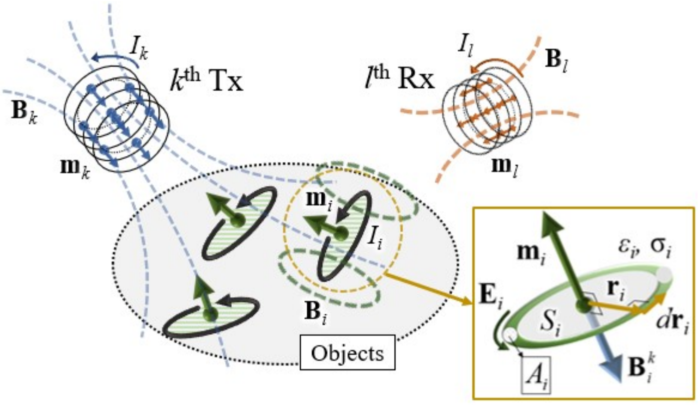

Fig.5.1 eDMP model of MIT.

The eDMP model utilizes multiple magnetic dipole moments to describe a coil and analyze the magnetic field. The number, arrangement, and strength of dipole moments are optimized, considering the design of a coil [54]. Magnetic vector potential $\mathbf{A}$, flux density $\mathbf{B}$ and mutual inductance between two coils can be computed using the dipole moments in (3.3-4) and (3.7). Fig. 5.1 shows the eDMP applied to the MIT. Two coils, as Tx and Rx, are modeled with the dipole moments $\mathbf{m}_k$ (blue arrows) and $\mathbf{m}_l$ (brown arrows), with current input I_k (blue curved arrow) and I_l (brown curved arrow), respectively. Unlike Tx and Rx, the objects can take various shapes, but not that of a coil. Thus, it is assumed that the object comprises numerous single-turn coils. The i^{th} object coil carrying current I_i has a loop with radius r_i (= $||\mathbf{r}_i||$) and the cross-section area A_i of coil winding. Furthermore, the loop is composed of a material with σ_i and ε_i. Each single-turn coil is represented as an SD moment, $\mathbf{m}_i$ (green arrow).

For the given design of Tx and Rx coils, the orientation and strength of $\mathbf{m}_i$ can be computed using (5.1) and (3.4). As in (5.1), the induced field $\mathbf{E}_i$ in the coil of I_i becomes perpendicular to the primary field at the i^{th} object, $\mathbf{B}_i^k$, which can be assumed to be uniform within the loop area S_i (= πr_i^2), encircled by the current, particularly for a small r_i. Then, (5.1) can be converted to (5.2) for the i^{th} object.

$$\oint_{\gamma_i} \mathbf{E}_i \cdot d\mathbf{r}_i = -\iint_{S_i} \frac{\partial \mathbf{B}_i^k}{\partial t} \cdot \mathbf{n}_i dS_i \tag{5.2}$$

$$\oint_{\gamma_i} \mathbf{E}_i \cdot d\mathbf{r}_i = 2\pi r_i \|\mathbf{E}_i\| \tag{5.2a}$$

$$-\iint_{S_i} \frac{\partial \mathbf{B}_i^T}{\partial t} \cdot \mathbf{n}_i dS_i = -j\omega\pi r_i^2 \left\| \mathbf{B}_i^k \right\| \tag{5.2b}$$

where t is time; $\mathbf{n}_i$ is the unit normal vector of S_i; $d\mathbf{r}_i$ is the unit tangent vector of loop I_i; and the negative sign follows Lenz's law.

Based on the orientations of $\mathbf{E}_i$ and I_i, the dipole moment $\mathbf{m}_i$ per unit I_i can be obtained as (5.3), following the definition of the magnetic single dipole moment.

$$\mathbf{m}_i / I_i = \oint_{\gamma_i} \mathbf{r}_i \times d\mathbf{r}_i = \pi r_i^2 \, \mathbf{B}_i^k \Big/ \left\| \mathbf{B}_i^k \right\| \tag{5.3}$$

The strengths of I_i and $\mathbf{m}_i$ can be determined as functions of σ_i and ε_i using Ohm's law. Thus, the equivalent circuit model is applied to solve Ohm's law in the objects. Furthermore, the circuit model can compute the phase shift considering the source of Tx and load of Rx. Fig. 5.2 shows the equivalent circuit model of the MIT system shown in Fig. 5.1. The coils of Tx and Rx are represented as the *RL* circuit, composed of resistance R_k, R_l and self-inductance L_k, L_l, respectively and have source impedance Z_S and load impedance Z_L. The *RL* circuit is used to model the i^{th} object with resistance R_i and self-inductance L_i. Each circuit is connected through the mutual inductances $M_{k,i}$, $M_{i,l}$, and $M_{k,l}$ between Tx and the object, Rx and the object, and Tx and Rx, respectively. As the Tx is activated by time-harmonic input V_{IN}, the Z-parameter of the MIT system can be expressed as (5.4-5.4b).

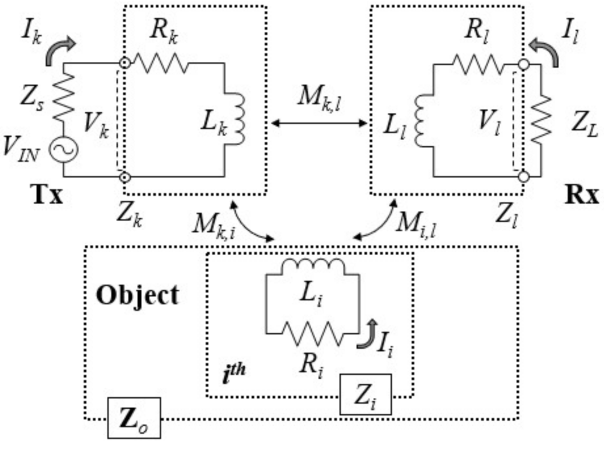

Fig. 5.2. Equivalent circuit model of the MIT system.

$$\begin{bmatrix} V_{IN} \\ 0 \\ \mathbf{0}_{N_i \times 1} \end{bmatrix} = [\mathbf{Z}] \begin{bmatrix} I_k \\ I_l \\ \mathbf{I}_o \end{bmatrix} \tag{5.4}$$

$$[\mathbf{Z}] = \begin{bmatrix} Z_s + Z_k & j\omega M_{k,l}{}^{\mathrm{T}} & j\omega \mathbf{M}_{k,o}{}^{\mathrm{T}} \\ j\omega M_{k,l} & Z_l + Z_L & j\omega \mathbf{M}_{l,o}{}^{\mathrm{T}} \\ j\omega \mathbf{M}_{k,o} & j\omega \mathbf{M}_{l,o} & \mathbf{Z}_o \end{bmatrix} \tag{5.4a}$$

$$Z_a = R_a + j\omega L_a \qquad (a = k,\ l,\ i) \tag{5.4b}$$

where $\mathbf{M}_{k,o} = [M_{k,1} \dots M_{k,Ni}]^{\mathrm{T}}$; $\mathbf{M}_{l,o} = [M_{l,1} \dots M_{l,Ni}]^{\mathrm{T}}$; $Z_o = Z_i \mathbf{I}_{N_i \times N_i}$; and $\mathbf{I}_o = [I_1 \dots I_{Ni}]^{\mathrm{T}}$.

The circuit parameters of the objects modeled as a single-turn coil, R_i and L_i, can be computed using the coil design shown in Fig. 5.1. R_i is estimated with complex conductivity κ_i ($= \sigma_i + j\omega\varepsilon_i$), as shown in (5.5).

$$R_i = \frac{2\pi r_i}{\kappa_i A_i} \tag{5.5}$$

The self-inductance of an object is defined as the magnetic flux passing through the current loop area per unit current and hence, L_i is obtained in (5.6), using Appendix (A.2-A.4). Finally, Z_i in (5.4b) is expressed as in (5.7).

$$L_i = \pi r_i^2 \left\| \mathbf{B}_i \right\|_{S_i} \Big/ I_i = \mu_0 \pi r_i / 2 \tag{5.6}$$

$$Z_i = \frac{2\pi r_i}{\left(\sigma_i + j\omega\varepsilon_i\right) A_i} + j\omega \frac{\mu_0 \pi r_i}{2} \tag{5.7}$$

The mutual inductances in (5.4a) can be computed by substituting $\mathbf{m}_k$, $\mathbf{m}_l$, and $\mathbf{m}_i$ in (3.5). Then, the impedance $\mathbf{Z}$ in (5.4) can be estimated using (5.2)−(5.7). As in (5.8), V_{kl0} and ΔV_{kl} are the voltages induced on Z_L due to the Tx and objects, respectively. The phase shift by the objects, $\Delta\varphi_{kl}$, is obtained in (5.9).

$$V_{kl0} + \Delta V_{kl} = -\frac{Z_L}{Z_l + Z_L}\left(j\omega M_{k,l} I_k + j\omega \mathbf{M}_{l,o}{}^{\mathrm{T}} \mathbf{I}_o \right) \tag{5.8}$$

$$\Delta\varphi_{kl} = \angle\left(\frac{V_{kl0} + \Delta V_{kl}}{V_{kl0}} \right) = \tan^{-1}\left(\frac{\mathbf{M}_{l,o}{}^{\mathrm{T}} \mathbf{I}_o}{M_{k,l} I_k} \right) \tag{5.9}$$

5.2.2 Conductivity estimation of MIT

Fig. 5.3 shows that the number of Txs, N_k, and number of Rxs, N_l, are applied to the plane ROI with radius R_{ROI}. The Txs and Rxs surround the ROI, with radii R_{T} and R_{R}, respectively. It is crucial to measure several effective measurements from Rxs and estimate the conductivity of the number of objects, N_i, minimizing the ill-posed condition. In general, a Tx is energized with various input frequencies, and then, the phase shift is measured at every Rx due to the object. The various fields can be formed by activating the Tx arrangement with respect to the object and Rxs.

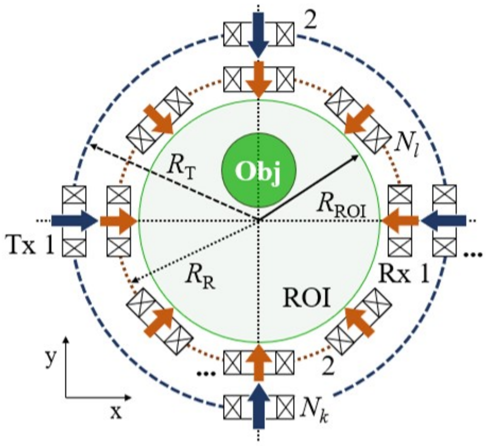

Fig. 5.3. Design of the MIT system with multiple Txs and Rxs.

The mutual inductance $\mathbf{M}_{l,o}$ in the third row of (5.4a) can be neglected since the effect of the magnetic field from the Rx coil on the object is small as the Rx yields a relatively weak field compared to the Tx coil. Thus, each eddy current I_i becomes directly proportional to $M_{k,i}$ and is expressed using admittance Y_i (= $1/Z_i$) in (5.10).

$$I_i = -j\omega M_{k,i} I_k / Z_i = -j\omega M_{k,i} I_k Y_i \tag{5.10}$$

The voltage induced from the objects to the l^{th} Rx is a linear combination of Y_i, as shown in (5.11). Subsequently, the phase shift $\Delta\varphi_{kl}$ at the l^{th} Rx is computed by substituting (5.11) for (5.9), in (5.12).

$$j\omega \mathbf{M}_{l,o}{}^{\mathrm{T}} \mathbf{I}_o = \omega^2 \sum_{i=1}^{N_i} M_{l,i} M_{k,i} I_k Y_i \tag{5.11}$$

$$\tan\left(\Delta\varphi_{kl}\right) = -j\omega \sum_{i=1}^{N_i} M_{l,i} M_{k,i} Y_i \Big/ M_{k,l} \tag{5.12}$$

For each Tx and Rx, the phase shift due to the admittance $\mathbf{Y}_o$ can be expressed using the sensitivity matrix $\mathbf{P}$.

$$\tan\left(\Delta\boldsymbol{\varphi}\right) = \left[\mathbf{P}\right]\mathbf{Y}_o \tag{5.13}$$

$$\mathbf{P} = \left[\mathbf{P}_{1,Ro}{}^{\mathrm{T}} \quad \cdots \quad \mathbf{P}_{k,Ro}{}^{\mathrm{T}} \quad \cdots \quad \mathbf{P}_{N_k,Ro}{}^{\mathrm{T}}\right]^{\mathrm{T}} \tag{5.13a}$$

$$\mathbf{P}_{k,Ro} = \begin{bmatrix} \cdots & (l-1)^{th} & \cdots \\ (i-1)^{th} & -\dfrac{j\omega M_{l,i} M_{k,i}}{M_{k,l}} & (i+1)^{th} \\ \cdots & (l+1)^{th} & \cdots \end{bmatrix} \tag{5.13b}$$

where $\mathbf{Y}_o = [1/Z_1 \ \ldots \ 1/Z_{N_i}]^{\mathrm{T}}$; $\Delta\boldsymbol{\varphi} = [\Delta\boldsymbol{\varphi}_{1R}{}^{\mathrm{T}} \ \ldots \ \Delta\boldsymbol{\varphi}_{N_kR}{}^{\mathrm{T}}]^{\mathrm{T}}$; $\Delta\boldsymbol{\varphi}_{kR} = [\Delta\varphi_{k1} \ \ldots \ \Delta\varphi_{kN_l}]^{\mathrm{T}}$; $\mathbf{P}_{k,Ro} \in \mathbb{C}^{N_l \times N_i}$; and $\mathbf{P} \in \mathbb{C}^{(N_k N_l) \times N_i}$.

The admittance $\mathbf{Y}_o$ can be computed by solving inverse of (5.13), using Tikhonov regularization in (5.14). Finally, the conductivity can be estimated in (5.15).

$$\mathbf{Y}_o = \left(\mathbf{P}^{\mathrm{T}}\mathbf{P} + \lambda\mathbf{I}\right)^{-1}\mathbf{P}^{\mathrm{T}}\tan\left(\Delta\boldsymbol{\varphi}_R\right) \tag{5.14}$$

$$\sigma_i = \mathrm{Re}\left(\frac{2\pi r_i}{\left(Z_i - j\omega L_i\right)A_i}\right) \tag{5.15}$$

where λ is the scalar regularization parameter.

5.2.3 Effect of objects on magnetic field

The magnetic field in the ROI is initially parallel to the primary field by $\mathbf{m}_i$ of Txs without an object. Once the object is placed in the ROI, the field would be changed by the secondary field generated by the object dipoles. The original primary field should be reflected by the secondary field, which can be iteratively computed to converge to a steady-state field. At the $(n\text{-}1)^{\mathrm{th}}$ iteration step, the i^{th} object current I_i^{n-1} and dipole $\mathbf{m}_i^{n-1}$ are computed by (5.4) after (5.14). Then, the secondary field and total field on the i^{th} object at the n^{th} computation, $\mathbf{B}_i^{o,n}$ and $\mathbf{B}_i^{k,n}$, can be estimated as shown in (5.16) and (5.17). Consequentially, the direction of $\mathbf{m}_i$ is rearranged according to (5.18) and the conductivity can be accurately updated by repeating (5.4-15). The iteration is proceeded until the dipole moments converge. The entire procedure is summarized in Fig. 5.4.

$$\mathbf{B}_i^{o,n-1} = \frac{\mu_0}{4\pi}\sum_{\substack{h=1\\(h\neq i)}}^{N_i}\frac{\left(\mathbf{m}_h^{n-1}\cdot\hat{\mathbf{r}}_{i,h}\right)\hat{\mathbf{r}}_{i,h} - \mathbf{m}_h^{n-1}}{\left|\mathbf{r}_{i,h}\right|^3} \tag{5.16}$$

$$\mathbf{B}_i^{k,n} = \mathbf{B}_i^{k} + \mathbf{B}_i^{o,n-1} \tag{5.17}$$

$$\mathbf{m}_i^n / I_i^n = \pi r_i^2\,\mathbf{B}_i^{k,n} \Big/ \left\|\mathbf{B}_i^{k,n}\right\| \tag{5.18}$$

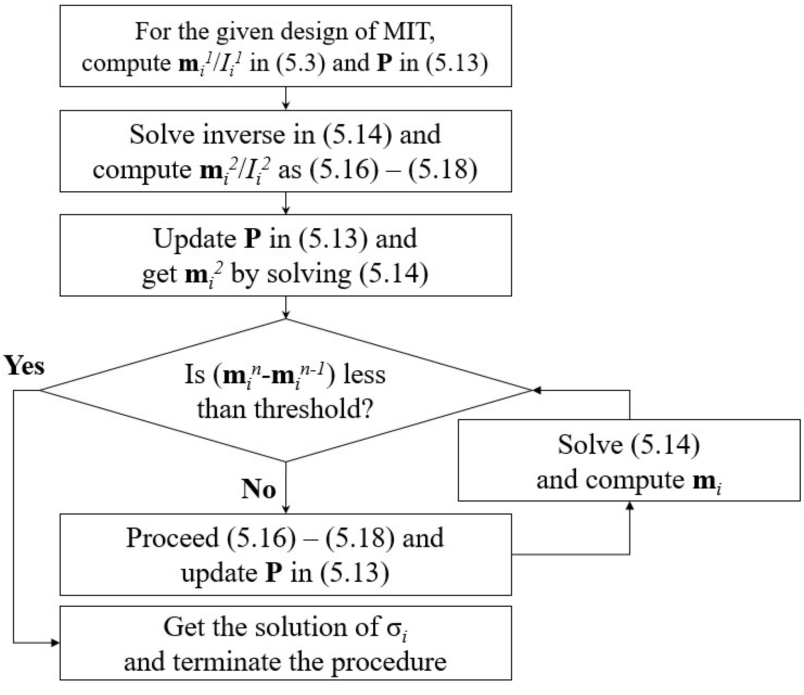

Fig. 5.4. Flowchart of eDMP modeling for MIT.

5.2.4 Performance estimation

Performance of the MIT system could be estimated by conductivity and spatial resolution. The resolutions can be defined as the variance of the parameters per unit phase shift. Phase shift $\Delta\varphi_{lk}$ could be represented as a function including variables accounting for position $\mathbf{x}_i$, conductivity σ_i and size R_{obj}.

$$\Delta\varphi_{lk}\left(\mathbf{x}_i,\sigma_i,R_{obj}\right)=\sum_{i}^{N_i}P_{k,l,i}Y_i=-\frac{1}{\left(\mathbf{m}_l\cdot\mathbf{B}_l^k\right)}\sum_{i=1}^{N_i}\left(\mathbf{m}_l\cdot\mathbf{B}_l^i\right) \tag{5.19}$$

Conductivity resolution (CR) is calculated as phase shift variance due to conductivity change with the given position and size, $\mathbf{x}_0$ and R_0:

$$CR=\left(\left.\frac{\partial\Delta\varphi_{kl}\left(\mathbf{x}_i,\sigma_i,R_{obj}\right)}{\partial\sigma_i}\right|_{\mathbf{x}_i=\mathbf{x}_0,R_{obj}=R_0}\right)^{-1} \tag{5.20}$$

$$\left.\frac{\partial\Delta\varphi_{kl}\left(\mathbf{x}_i,\sigma_i,R_{obj}\right)}{\partial\sigma_i}\right|_{\mathbf{x}_i=\mathbf{x}_0,R_{obj}=R_0}=-P_{k,l,i}\frac{\partial Y_i}{\partial\sigma_i}$$

For the low conductivity materials, it is assumed that imaginary term of Y_i is neglected. Then $\partial\sigma_i/\partial Y_i$ become constant, $A_i/2\pi r_i$.

Similarly, spatial resolution (SR) is computed using phase shift variance as position changes with the given conductivity and size, σ_0 and R_0. It is similar to the gradient of the secondary field.

$$SR=\left(\left.\frac{\partial\Delta\varphi_{kl}\left(\mathbf{x}_i,\sigma_i,R_{obj}\right)}{\partial\mathbf{x}_i}\right|_{\sigma_i=\sigma_0,R_{obj}=R_0}\right)^{-1} \tag{5.21}$$

$$\left.\frac{\partial\Delta\varphi_{kl}\left(\mathbf{x}_i,\sigma_i,R_{obj}\right)}{\partial\mathbf{x}_i}\right|_{\sigma_i=\sigma_0,R_{obj}=R_0}=-\frac{\mathbf{m}_l}{\left(\mathbf{m}_l\cdot\mathbf{B}_l^k\right)}\cdot\left(\frac{\partial\mathbf{B}_l^i}{\partial\mathbf{x}_i}\right) \tag{5.22}$$

Considering the minimum detectable phase shift $\Delta\varphi_{\min}$, resolution for the practical system can be computed as the minimum variance which is capable of yielding phase shift equal to $\Delta\varphi_{\min}$. $\Delta\varphi_{\min}$ depend on the specification of a measurement device and SNR.

$$\text{Resolution}=\Delta\varphi_{\min}\left(\frac{\partial\Delta\varphi_{kl}\left(\mathbf{x}_i,\sigma_i,R_{obj}\right)}{\partial x_i}\right)^{-1} \tag{5.23}$$

where $x_i = [\mathbf{x}_i, \sigma_i]$.

Minimum detectable conductivity and size are computed as phase shift equals $\Delta\varphi_{\min}$.

$$\Delta\varphi_{kl}\left(\mathbf{x}_i,\sigma_i,R_{obj}\right)=\Delta\varphi_{\min} \tag{5.24}$$

5.3 Validation

The performance of MIT is estimated by examining the effects of conductivity, position, and shape of objects. First, the numerical simulations of both eDMP and finite-difference time domain (FDTD) methods are conducted, and then, the results are compared to the experiment results. Each experiment is repeated three times for reliability. The mean and standard deviation of the results are presented.

5.3.1 MIT system setup

The MIT system is constructed for experiments with one set of a Tx and Rx, as shown in Fig. 5.5(a), and shielded from the external magnetic field. The geometry of the system and the design of the Tx and Rx are detailed in Tables 5.1 and 5.2, respectively.

Physiological saline similar to the human body fluid is applied to the object. At room temperature, the salt concentration is 0.9 %, conductivity is 1.6 S/m, and relative permittivity is 80. Two shapes, circle and square, are used as the target object to examine the effect of shape. Physiological saline 40 ml is injected in a circle and square case in Fig. 5.5 (b) and (c).

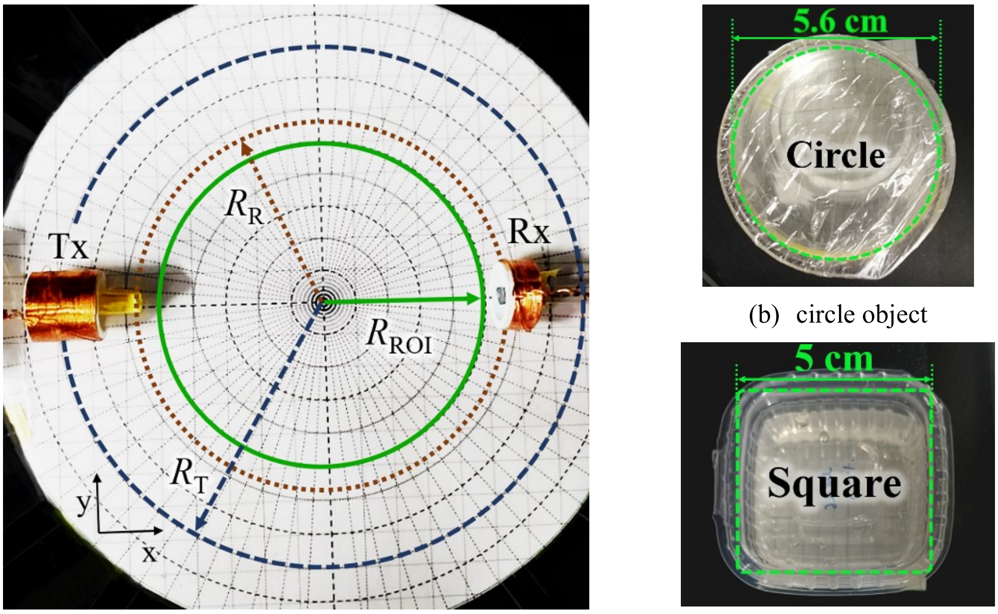

(b) circle object

(a) MIT system

(c) square object

Fig. 5.5. Picture of MIT setup.

Table 5.1. Geometry of the MIT System

R_T (cm)	7.6
R_R (cm)	5.6
R_{ROI} (cm)	5.0

Table 5.2. Coil design

	Tx	Rx
Radius (cm)	1.0	1.0
Height (cm)	2.0	1.0
Number of turns	60	18
Diameter of wire (mm)	0.3	0.5
Resistance (Ω)	0.5	0.2
Inductance (μH)	20	8.5

The experimental setup for the measurement is represented by the block diagram shown in Fig. 5.6. The NI pxie-5632 vector network analyzer (VNA) is used to measure the S-parameters of the device under test, with bandwidth of 300 kHz to 8.5 GHz.

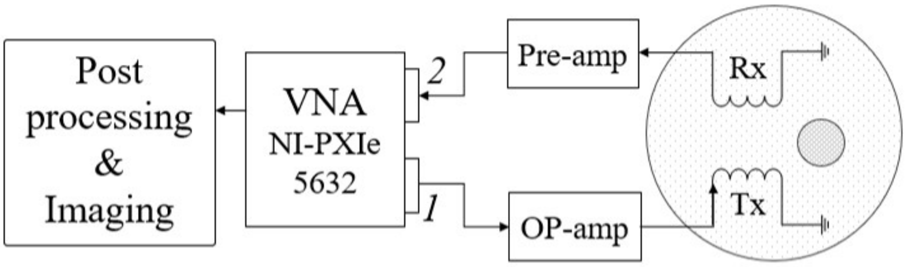

Fig. 5.6. Block diagram of the MIT system.

5.3.2 Simulation

The FDTD method is used to estimate and compare the performance of MIT. Unlike other numerical methods based on the frequency domain, FDTD is simulated in time domain based on the partial differential form of Maxwell's equations, so that a wide range of frequencies can be calculated simultaneously. FDTD has been applied to a range of systems, from ultralow frequency to visible light, due to the advantage of time-domain simulation and effectiveness.

Fig. 5.7(a) and (b) show that FDTD is applied to the MIT system in Fig. 5.5(a) and a square ROI of 28.8 cm × 28.8 cm × 15.8 cm is divided by 204, 204, and 74 cells in the x-, y-, and z-axes, respectively. At the end of each axis, eight lines of the perfect matched layer are placed for absorbing the boundary condition. As the method requires a large computational resource due to the enormous number of meshes, for accuracy, it is performed using a computer with INTEL quad-core i7 and 3.30 GHz CPU.

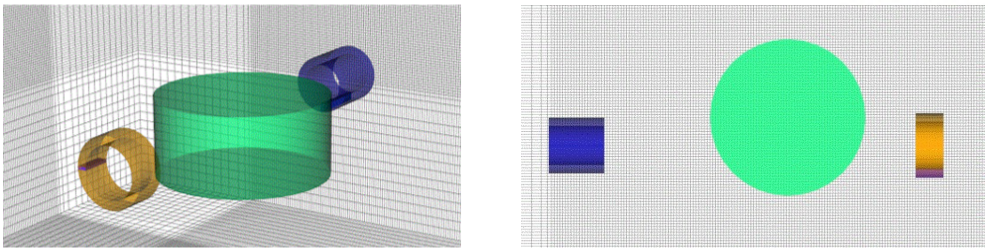

(a) 3D view (b) x-y plane

Fig. 5.7. FDTD model of the MIT system.

Similarly, the eDMP method is applied in Fig. 5.8(a) based on the coil design in Table II. In Fig. 5.8(b), the magnetic field generated by Tx is compared to that generated by FDTD for validation. In Figs. 5.8(c) and (d), the magnetic flux density **B** per current along the central axis of the Tx and Rx is computed, 10 cm from the surface of the coil, and the eDMP is compared with the FDTD. The mean discrepancy between the eDMP and FDTD is 0.0013 and 0.0044 mT.

(a) eDMP model of a coil (b) FDTD model of a coil

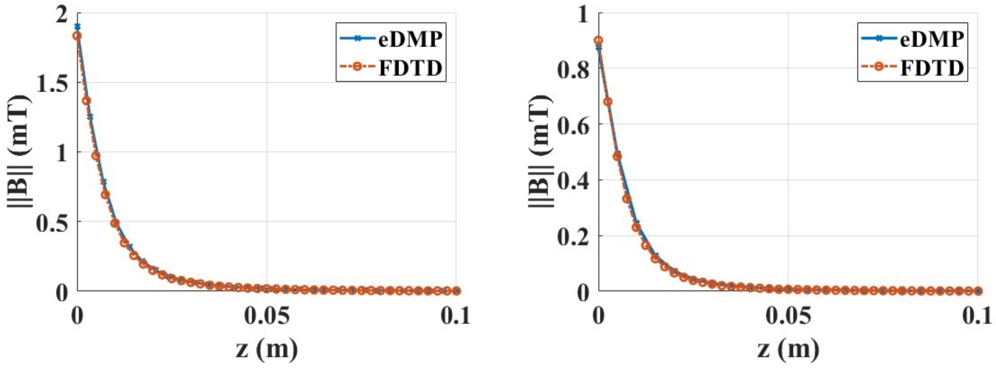

(c) ||B|| of Tx (d) ||B|| of Rx

Fig. 5.8 Comparison of eDMP and FDTD.

For the object modeling, the triangular distribution of object dipoles is used, since it can effectively account for various object shapes. Thus, object dipoles are arranged to form uniform regular triangles. Then, the following dipole parameters should be determined: r_i, N_i, and A_i. r_i in (5.3) can be set as half the length of the triangle to prevent overlapping between nearby dipoles. N_i should be large enough to describe the object shape and the primary field in the ROI. However, an excessively large N_i increases the computational effort. Fig. 5.9 (a) shows that the total induced voltage in the plane ROI per unit Tx current converges as N_i increases. It is confirmed that the number larger than 1000 results in steady computation. Considering the computation resource, N_i is set as 1270 and r_i is set as 3 mm. It is difficult to estimate A_i accurately since the eddy current in the objects cannot be observed directly. But A_i can be removed by normalizing phase shift. Finally, the eDMP model of the MIT system in Fig. 5.5 (a) can be presented in Fig. 5.9 (b-c), where single arrows indicate orientation of the coil. The object dipoles corresponding to the saline in Fig. 5.5 (b) are represented as pink circles. Phase shift in the model can be computed using (5.13). In Fig. 5.9 (d), the phase shift, varying the Rx azimuth angle from -180 to 0°, is validated by comparing with other methods: the eDMP method including the mutual inductances between objects, Rxs and objects, in (5.4) and FDTD method. The phase shift in the results is normalized to the maximum of each result for comparison. It yields mean discrepancy 0.00003 with the eDMP including every term and 0.0096 with FDTD. Thus, it is confirmed that the eDMP method can be applied to compute phase shift using (5.13).

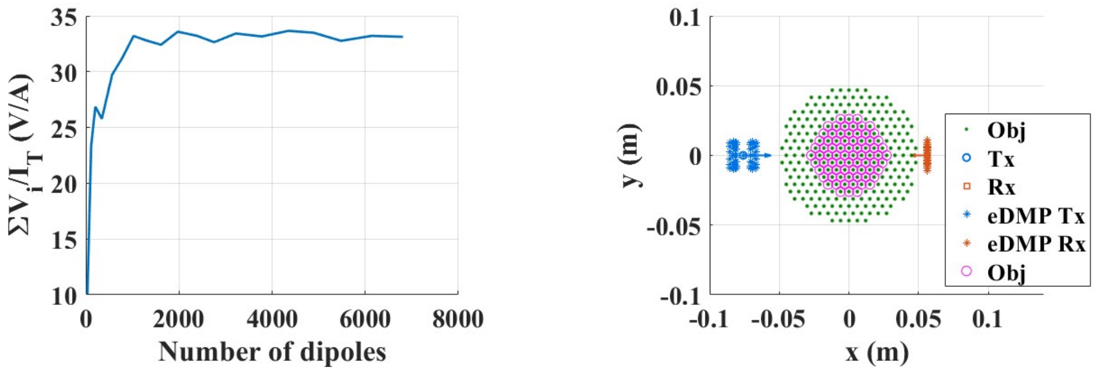

(a) Induced voltage in the ROI (b) x-y plane

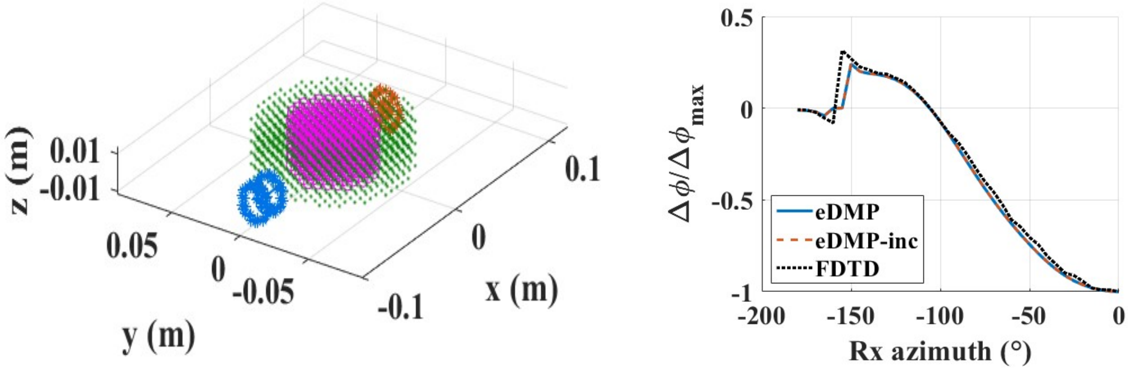

(c) 3D view (d) Comparison of phase shift

Fig. 5.9. eDMP model of the MIT system.

The operating frequency should be considered to enhance the system performance. The maximum allowable frequency for MIT is 30 MHz, due to β-dispersion in the living tissue, whereas increasing the frequency can amplify the phase shift, as shown in (5.13). In addition, the impedance of Tx is proportional to the frequency, as shown in (5.4b), and the increment in Tx impedance can reduce the SNR. Impedance matching can reduce the impedance at the specific frequency. The Rx circuit can be ignored because the phase shift does not depend on I_l in (5.13). Thus, for the design of a Tx coil in Table 5.2, the Tx circuit is tuned to operate at 24 MHz.

5.3.3 Effect of conductivity variation

In the human body, conductivity varies from 0.02 to 1.5 S/m. Blood conductivity is 1.14 S/m, muscle is 0.64, skin is 0.29, and bone is 0.02 [61]. Thus, the conductivity resolution of MIT should be high enough to determine the type of tissues. The MIT system is set in Fig. 5.10 (a). The circular object is placed at (0.01, 0) m, varying the conductivity within the range of human tissue, from 0.2 to 1.6 S/m. The trend in the phase shift due to conductivity variation is consistent in every setup; thus, without loss of generality, the result can be taken in other setups. In Fig. 5.10 (b), the experimental result is normalized with respect to a point at 1.6 S/m and compared to the simulation results, yielding a mean error of 0.0341 with eDMP and 0.3849 with FDTD. For low conductivity (< 0.8 S/m), the phase shift increases with the conductivity. However, for a conductivity above 0.8 S/m, the phase shift decreases. In (5.4-4b), high conductivity reduces R_i, and then, self-inductance $j\omega L_i$ becomes dominant in $\mathbf{Z}_o$ and the phase shift decreases. In FDTD, the phase shift is linear as the conductivity increases, because only resistance is considered. It is confirmed that the conductivity can be estimated from the phase shift within the tissue range.

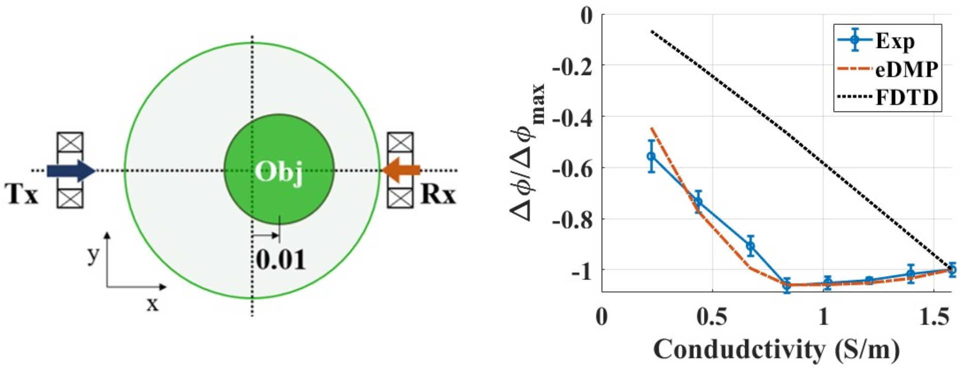

(a) Design (b) Result

Fig. 5.10. Phase shift as conductivity changes.

5.3.4 Effect of position

Phase shift, as the object position, indicates the spatial accuracy and resolution. In Fig. 5.11 (a), the system design is shown to move the object from -0.02 to 0.02 m, along the x-axis. The experimental result is compared to the simulation result in Fig. 5.11 (b), yielding a mean error of

0.0086 with eDMP and 0.0260 with the FDTD method. As the position changes from 0 to 0.02 m, the phase shift increases, and then, the position becomes distinguishable. However, within (-0.02-0) m, it is difficult to determine the position because the sensitivity in (5.13) is uniform within the region. Arranging the Tx and Rx on a symmetrical position can improve the spatial resolution in the region. Thus, numerous Txs and Rxs should be placed at various locations to enhance sensitivity in the entire ROI.

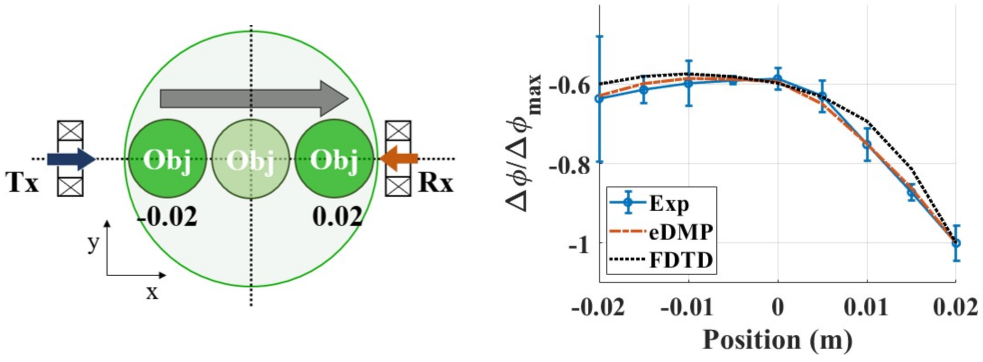

(a) Design (b) Result

Fig. 5.11. Phase shift as object moves.

The relative position between the Tx and Rx can achieve the same performance as that obtained using multiple Txs and Rxs, as shown in Fig. 3. Thus, the Tx is placed at every 90° ($N_k = 4$) and the Rx is arranged every 5°, from -90° to 265° ($N_l = 72$). In total, 288 phase shifts are acquired in the system. The circular object is placed at (0, 0.01) m and the eDMP model of the circle is shown in Fig. 5.12 (a). The phase shifts are arranged in Fig. 5.12, at (b) Tx1, (c) Tx2, and (d) Tx4, and normalized with respect to the maximum in Fig. 5.12 (b)−(d). The result at Tx3 is excepted since it is symmetrical to that at Tx1. The mean errors are listed in Table 5.3. In the simulation results, there are sharp peaks and discontinuities, such as Rx azimuth 150 and 210° in Fig. 5.12 (b), 60 and 120° in Fig. 5.12 (c). As an Rx coil is arranged perpendicular to the primary field, $M_{k,l}$ in (5.13b) becomes small which result in discontinuities. In the experiments, the peaks are not observed because there is a bias voltage on Rx. Except for the few points, the phase shift is shown clearly as Txs and Rxs change. In addition, the position of the object can be characterized in the results. For example, the maximum phase shift in Fig. 5.12 (c) is less than the maximum in Fig. 5.12 (d), as shown in Fig. 5.11 (b).

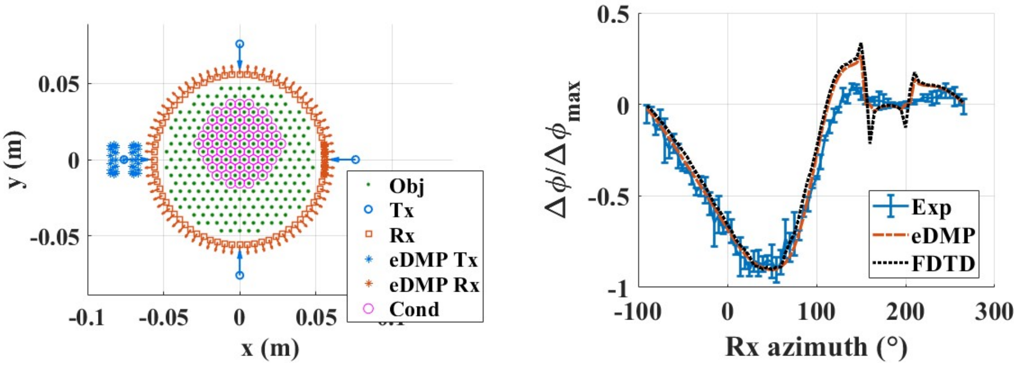

(a) eDMP model (b) Tx1

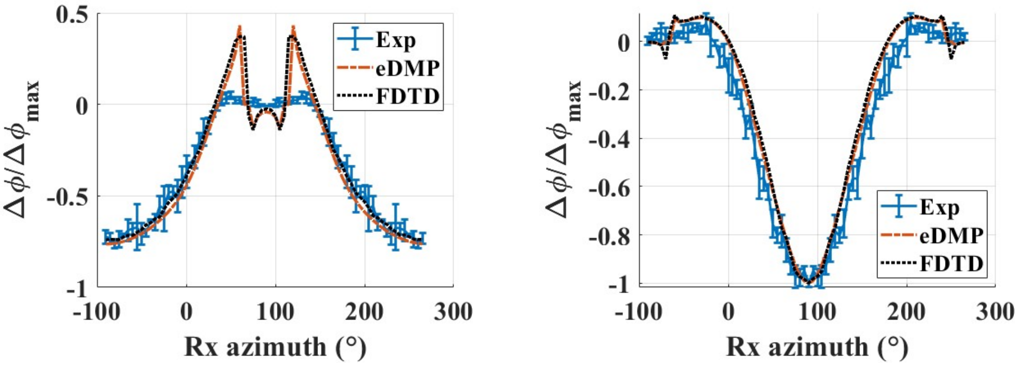

(c) Tx2 (d) Tx4

Fig. 5.12. Phase shift with multiple Txs and Rxs.

Table 5.3. Mean Error of Simulations in Fig. 5.12

Figure	(b)	(c)	(d)
eDMP	0.0528	0.0656	0.0669
FDTD	0.0749	0.0675	0.0774

5.3.5 Effect of object shape

Various shapes of a target object are required to characterize the type of tissues with similar conductivity. Fig. 5.13 (a) shows the eDMP model with the square object in Fig. 5.5 (c) placed at (0, 0.01) m to compare to the circle Fig. 5.13 (b)–(d) presents the results, yielding the mean errors as listed in Table 5.4. The phase shift in Fig. 5.13 is similar to that in Fig. 5.12, and has sharp peaks. Nevertheless, several differences are observed; the phase shift in Fig. 5.13 (b) has a higher gradient and sharper maximum than that in Fig. 5.12 (b). In addition, in Fig. 5.13 (d), the phase shift shows a blunt shape at the maximum, while the result of circle is sharp in Fig. 5.12 (d). It is confirmed that the MIT system can detect the object shape in phase shift.

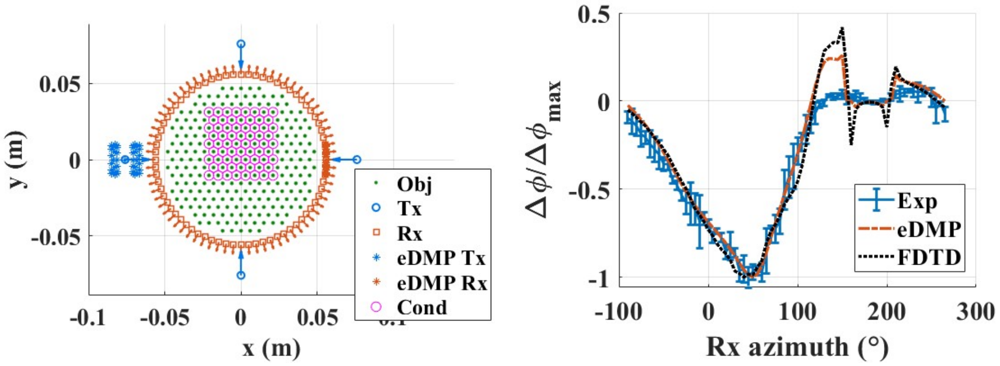

(a) eDMP model of square (b) Tx1

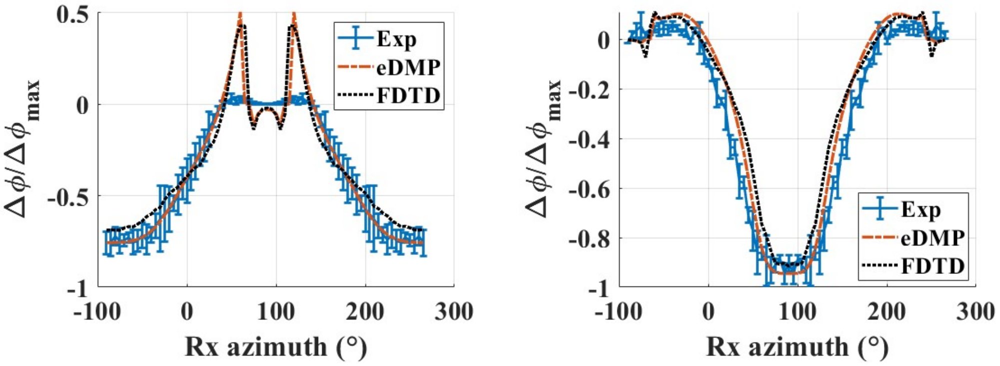

(c) Tx2 (d) Tx4

Fig. 5.13. Phase shift for square.

Table 5.4. Mean Error of Simulations in Fig. 5.13

Figure	(b)	(c)	(d)
eDMP	0.0554	0.0470	0.0704
FDTD	0.0789	0.0970	0.0872

5.3.6 System analysis

The MIT system in Fig. 5.5 is analyzed to estimate its performance in detail. As the given setup measure 288 data for phase shift, phase shift in (5.23) uses the maximum phase shift. Minimum detectable phase shift of the system is 0.5 deg. Fig. 5.14 (a) shows the eDMP models to compute resolution with respect to object position. A Tx and Rx are arranged to face each other for acquiring the maximum phase shift. The cylinder object with conductivity 1.6 S/m and radius 1 cm is moved from 0 to 0.038 m to compute the resolution. Fig. 5.14 (b-d) presents the phase shift, CR and SR as the object position changes. CR is similar as the inverse of phase shift and SR is the inverse of its gradient. Considering $\Delta\varphi_{\min}$, an object with 1.6 S/m conductivity and radius 1 cm can be detected at larger than 0.01 m. At the point, CR is 1.4 S/m and SR is 0.03 m. Maximum CR and SR are 0.31 S/m and 0.002 m.

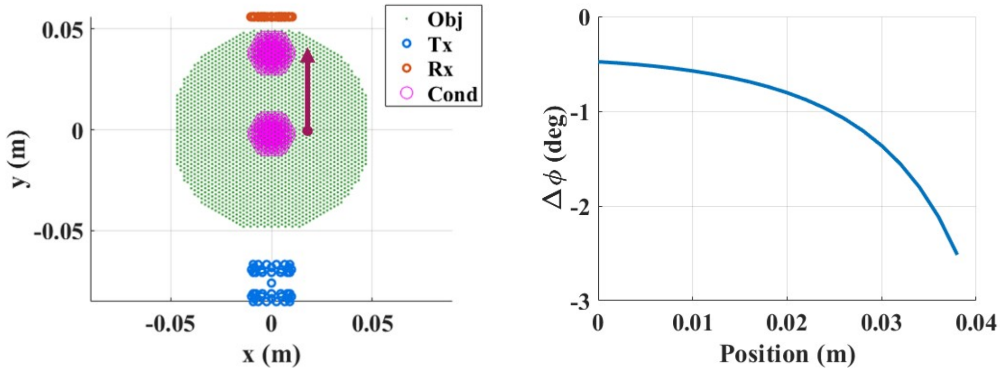

(a) eDMP model for object position (b) Phase shift as position changes

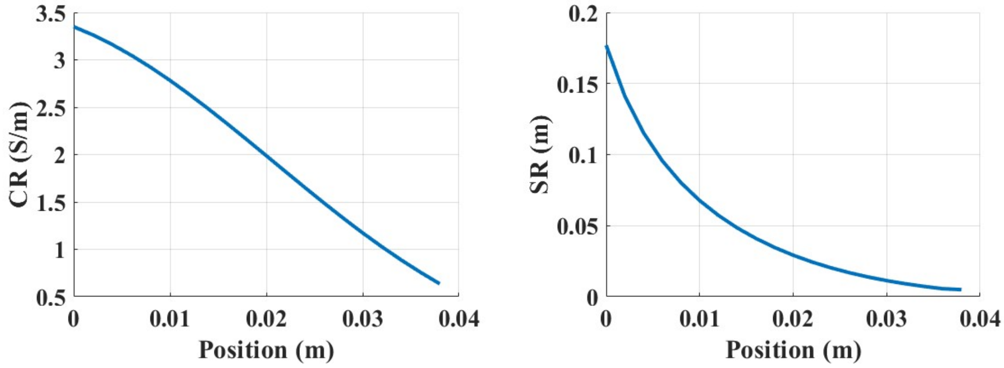

(c) CR as position changes (d) SR as position changes

Fig. 5.14. Resolution as position changes.

Fig. 5.15 (a) shows the object is placed on (0, 0.01) m, as Fig. 5.12 (a), and the radius increases from 1 to 3 cm. Phase shift and CR increase by the square of the radius increment. The object in Fig. 5.5 (b), with diameter 5.6 cm, has CR 0.22 S/m and SR 5 mm.

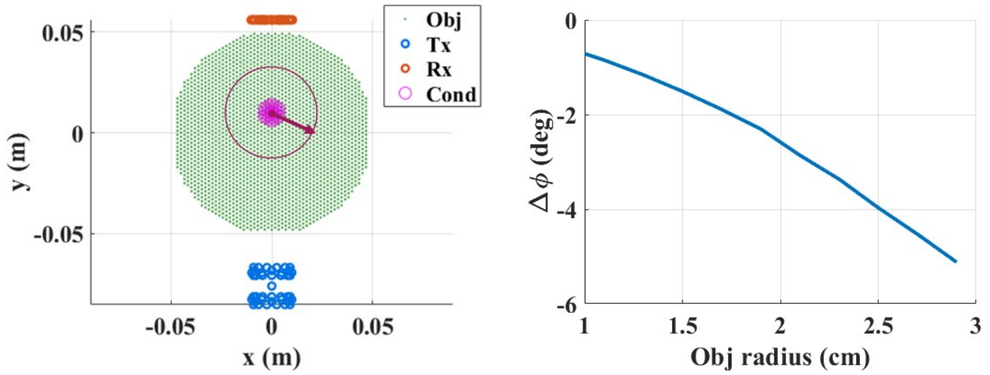

(a) eDMP model for object size (b) Phase shift as position changes

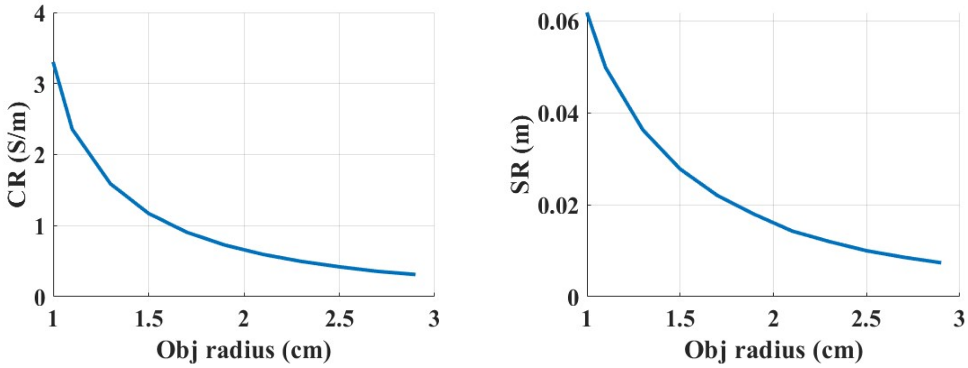

(c) CR as object size changes (d) SR as object size changes

Fig. 5.15. Resolution as object size changes.

The effect of conductivity change is investigated as the object with diameter 5.6 cm is placed on (0, 0.01) m. Fig. 5.16 shows the eDMP model and the analysis results. CR decreases as conductivity increases from 0.2 to 1.6 S/m. SR shows the same tendency as phase shift in Fig. 5.10. As conductivity is 0.8 S/m, SR is minimum, 4 mm. For the given object in Fig. 5.5 (b), the analysis presents the same resolution as Fig. 5.15 and it indicates the object position and shape larger than 5 mm can be detected.

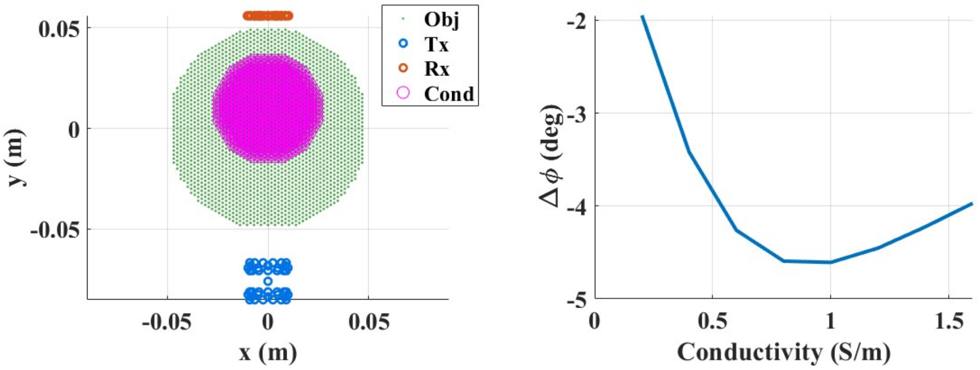

(a) eDMP model for conductivity (b) Phase shift as conductivity changes

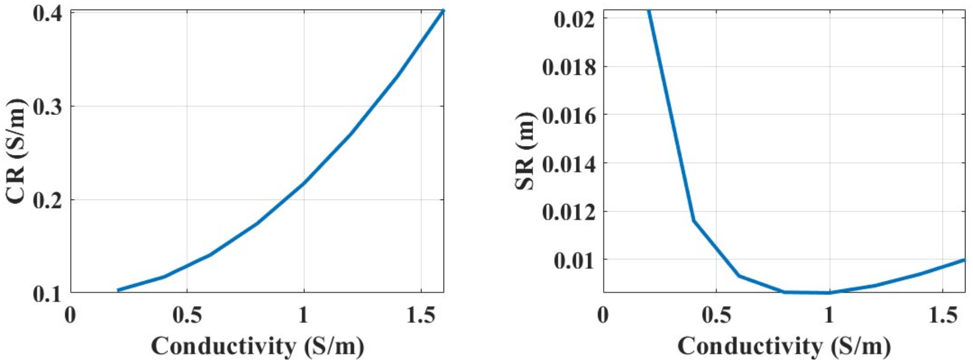

(c) CR as conductivity changes (d) SR as conductivity changes

Fig. 5.16. Resolution as conductivity changes.

5.3.7 Image reconstruction

The image reconstruction can be achieved by solving the inverse in (5.14), using the results in Fig. 5.12 and 5.13. Considering that large N_i causes an ill-posed condition, in Fig. 5.17 (a) and (b), the object dipoles of the eDMP models are rearranged as r_i is 4.5 mm and N_i is 456. True images are shown in Fig. 5.17 (c) for the circle and (d) for the square. Fig. 5.17 (e)−(f) is based on the eDMP simulation and Fig. 5.17 (g)−(h) shows the experimental results. In Fig. 5.17 (f), Tikhonov regularization coefficient in (5.14) is computed from the circle as a reference object for calibration and the corresponding coefficient is applied to the square in Fig. 5.17 (h). The final images are scaled to the absolute value for comparison. The simulation images show that the position and conductivity of the object corresponds with that of the true image and the object shape is distinguishable. But the results have the same resolution as that of the eDMP model shown in Fig. 5.17 (a)−(b), and thus, show coarser resolution than those of the true and experimental images. In the experimental images, the position of the objects corresponds with that of the true image. But conductivity is not uniform due to the measurement error in Fig. 5.12. The object shape is characterized: the circle in Fig. 5.17 (g) maintains curvature uniformly but has a smaller size than the true image. In Fig. 5.17 (h), the square has four edges, but the aspect ratio is less than one.

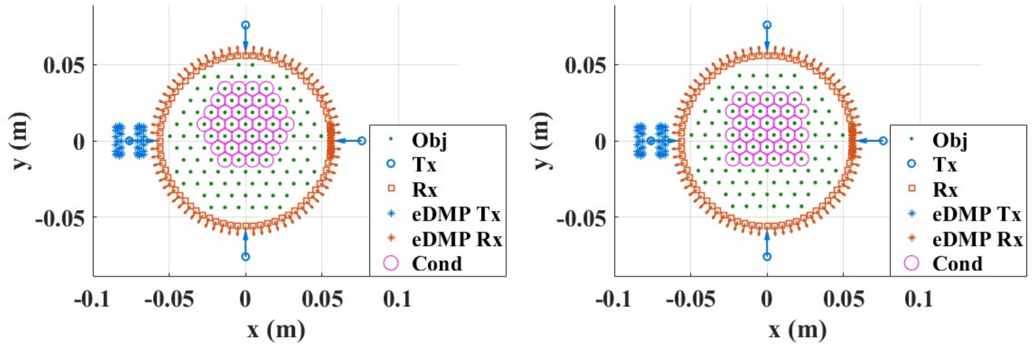

(a) eDMP model of circle

(b) eDMP model of square

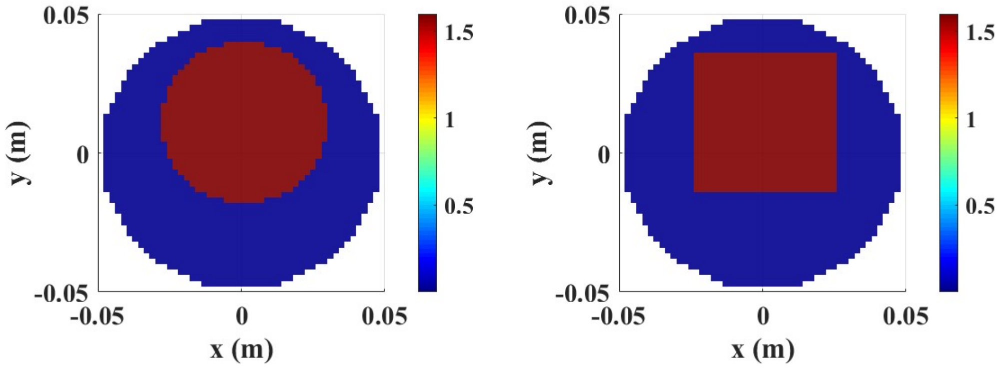

(c) True image of circle

(d) True image of square

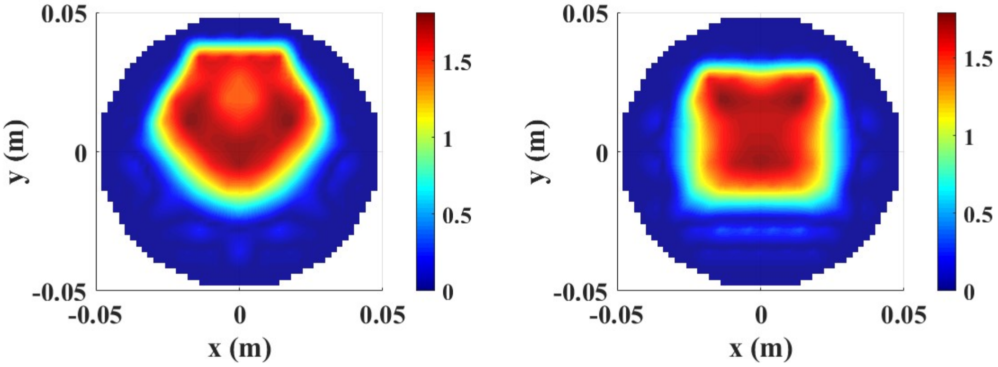

(e) Simulation results of circle (f) Simulation results of square

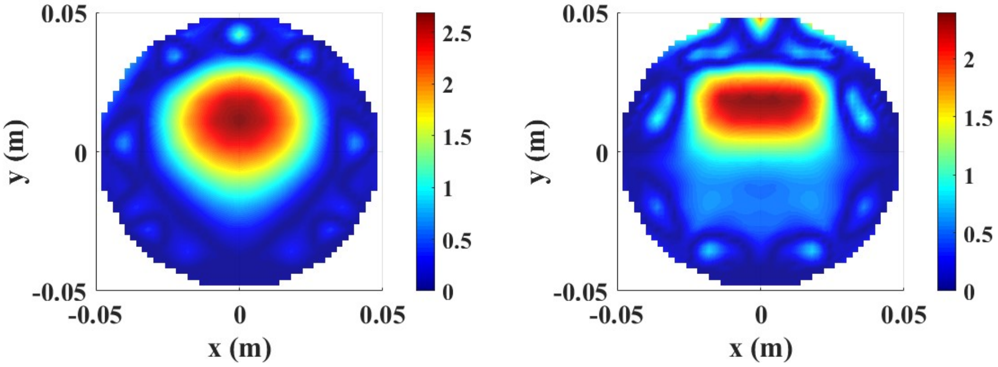

(g) Experimental results of circle (h) Experimental results of square

Fig. 5.14. Imaging results with r_i = 4.5 mm.

The image resolution can be improved by increasing the object dipoles in the vicinity of the object. In Fig. 18 (a) and (b), the eDMP models with r_i reduced from 4.5 mm to 3 mm are shown. In addition, dipoles 4 cm away from the object center are eliminated to improve the ill-posed condition. Thus, 995 dipoles are applied to describe the object shape. Consequently, the simulation results in Fig. 18 (c) and (d) show higher resolution than those in Fig. 17 (e) and (f). The experimental results are shown in Fig. 18 (e) and (f). The circle in Fig. 18 (e) is distorted more than that in Fig. 17 (g), but its size grows similar to the true image in Fig. 17 (c). In Fig. 18 (f), the aspect ratio of the square becomes one. Eventually, the results show that the MIT using the eDMP can be applied to reconstruct images to detect the conductivity, position, and shape of the object.

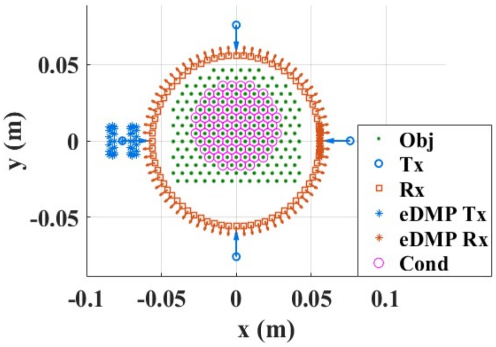

(a) eDMP model of circle (b) eDMP model of square

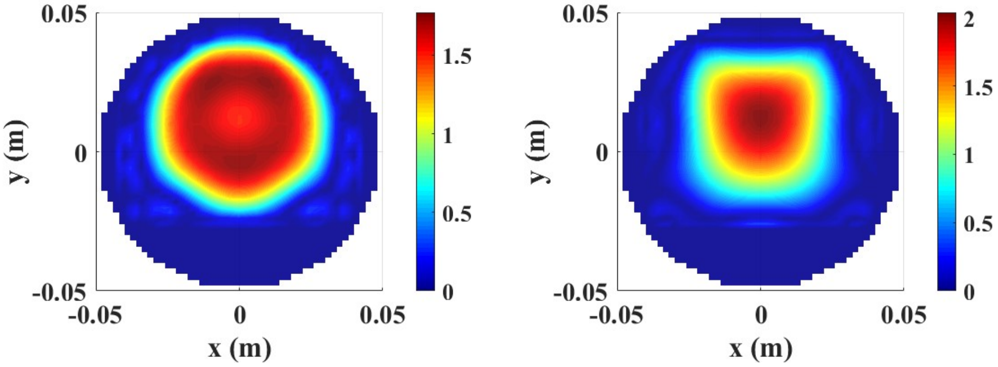

(c) Simulation results of circle (d) Simulation results of square

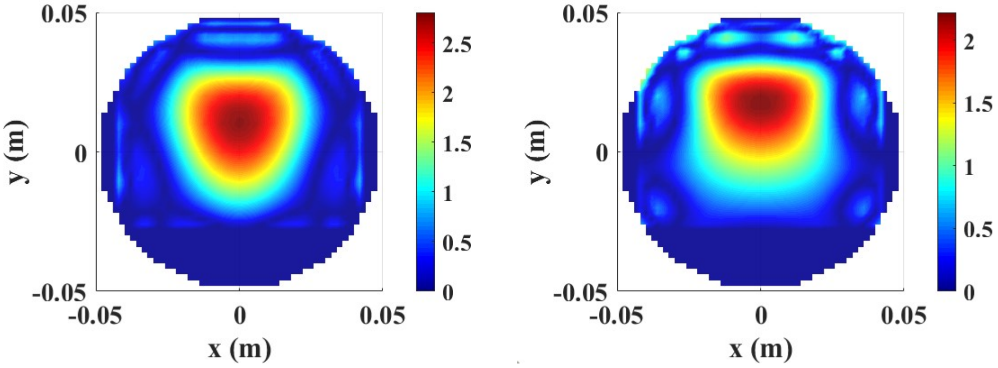

(e) Experimental results of circle (f) Experimental results of square

Fig. 5.18. Imaging results with $r_i = 3$ mm.

5.4 Multi-channel MIT

5.4.1 Phase-domain MIT transceiver

The system in Fig. 5.5 comprises a single coil set and uses a massive instrument for data acquisition. That kinds of systems are hard to make a device portable. Thus, MIT transceiver using a phase-locked loop (PLL) and a phase-domain sigma-delta modulator (PD-ΔΣM) has been proposed to construct portable and low power system [62]. Fig. 5.19 shows a block diagram of the MIT transceiver system. The PLL is capable of sweeping frequency. The PD-ΔΣM acquires analog data of the signal on a Rx and convert to digital to compute phase shift.

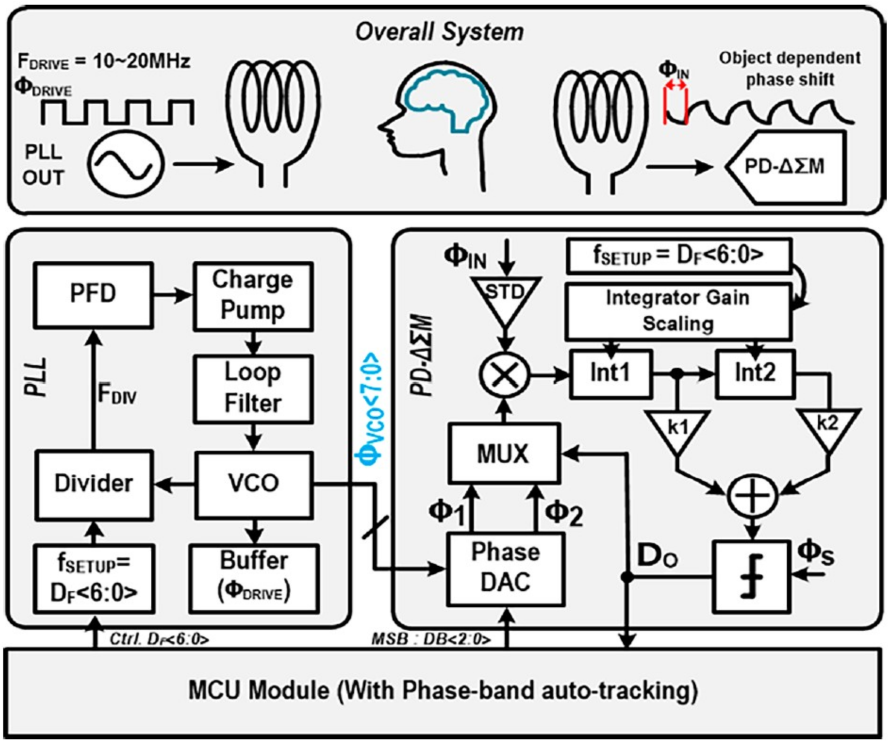

Fig. 5.19. Block diagram of MIT transceiver [62]

5.4.2 Multi-channel MIT system

The MIT transceiver system is constructed to implement the multi-channel MIT system. As shown in Fig. 5.20 (a), a MIT transceiver board comprises a chip for the phase domain computing, Mux for multi-channel measurement, power generator for a Tx, and Bluetooth connection for wireless data acquisition. 18650 Li-ion battery is used to input power. The board generates 1.5 MHz square wave with 3 V amplitude. Mux is capable of connecting 10 channels and has 70 ohms. Minimum voltage is 50 mV_{pp} and maximum voltage is limited as 2 V_{pp}. Minimum detectable phase shift, $\Delta\varphi_{min}$ is 0.1 deg. Based on the specification of the board, coils of the MIT system are designed. Fig. 5.20 (b) shows a Tx and a total of 7 Rxs are installed every 30 deg, considering the number of channels of Mux and size of the system. The circular ROI has 3 cm radius and Tx is designed to yield voltage larger than voltage limit. Detailed geometry is written in Table 5.5 and coil designs are in Table 5.6. Impedance matching for 1.5 MHz frequency is achieved at each coil considering voltage limit of the board. Tx is connected to 104 pF and Rx have 168, 221, 271, 276, 271, 221, 168 pF, from channel 1 to 7. As the transceiver system is constructed, the phase shift of each Rx could be measured automatically, and the data is acquired to a computer through Bluetooth connection.

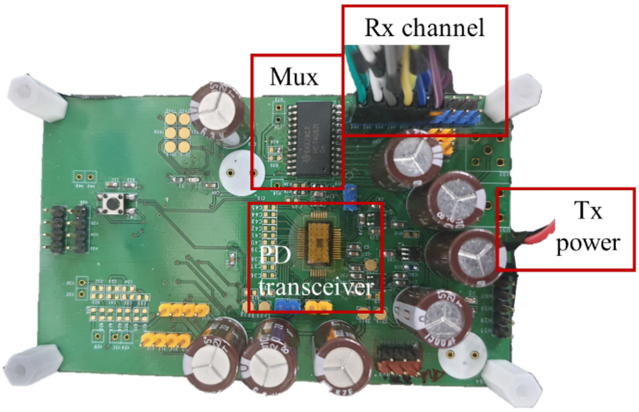

(a) Transceiver board

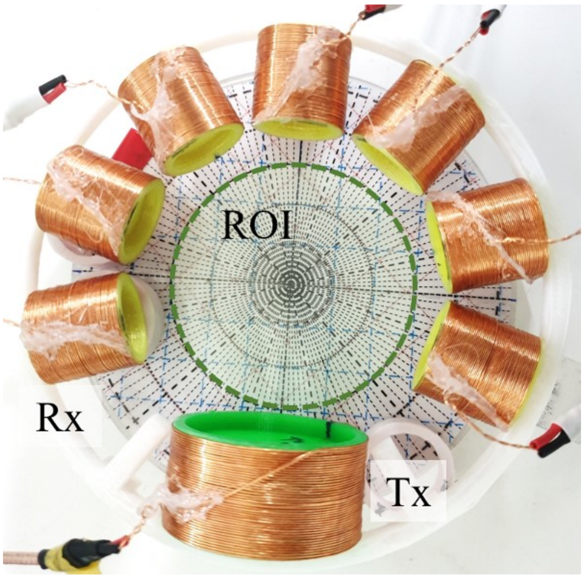

(b) Experimental setup

Fig. 5.20. Experimental setup of multi-channel MIT transceiver.

Table 5.5. Geometry of system

R_T (cm)	5.0	N_k	24
R_R (cm)	5.1	N_l	7
R_{ROI} (cm)	3.0		

Table 5.6. Geometry of coils

	Tx	Rx
Radius (cm)	2.0	1.0
Height (cm)	2.0	2.0
Number of turns	60	60
Diameter of wire (mm)	0.3	0.3
Resistance (Ω)	0.5	0.5

Inductance (μH)	109	42

Fig. 5.21 shows the system is represented as the eDMP model for sensitivity analysis. The object dipoles are placed with 1 mm distance and 2275 dipoles are applied to compute phase shift and resolution accurately. There are three planes of object dipoles to describe the volume of the object.

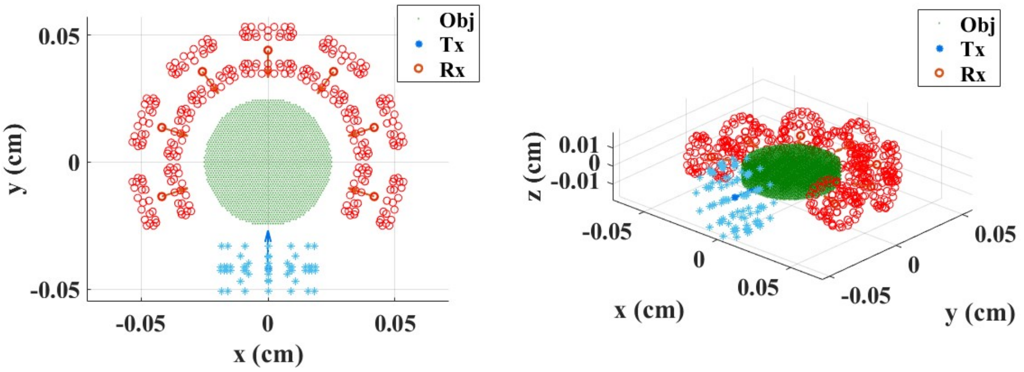

(a) eDMP model of circle

(b) eDMP model of square

Fig. 5.21. eDMP model of MIT transceiver.

5.4.3 System validation and analysis

Due to frequency limitation of the MIT transceiver system, it should be applied to the high conductivity materials. In this research, a carbon rod is utilized to detect the crack on the carbon rod.

Fig. 5.22 (a-b) shows the carbon rod with diameter 2.5 cm, thickness 1 mm and conductivity 3e5 S/m and the phase shift result It is placed on the center of the ROI. Phase shift for the 7 Rxs is compared to the eDMP simulation for validation, yielding mean error 0.49 deg. Each measurement is repeated three times for reliability and the standard deviation of the measurements yields average 0.08 deg. Due to symmetricity, phase shift is same as the system is rotated, and then image can be reconstructed. Fig. 5.22 (c-d) shows the true image and experimental image. In the experimental imaging, the carbon rod is expressed as a solid circle while the true image shows a thin rod.

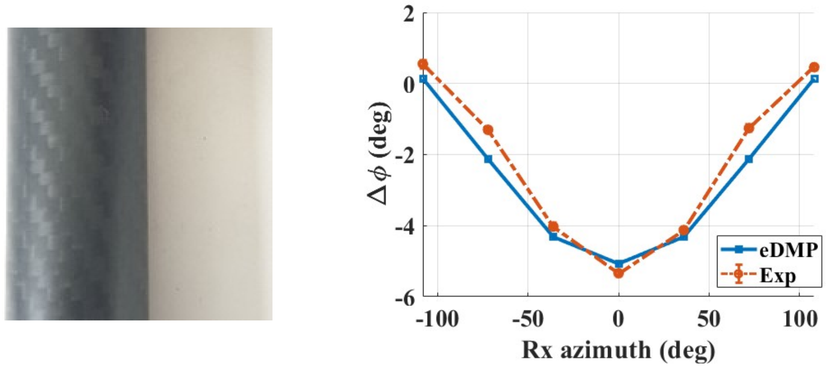

(a) Carbon rod

(b) Phase shift

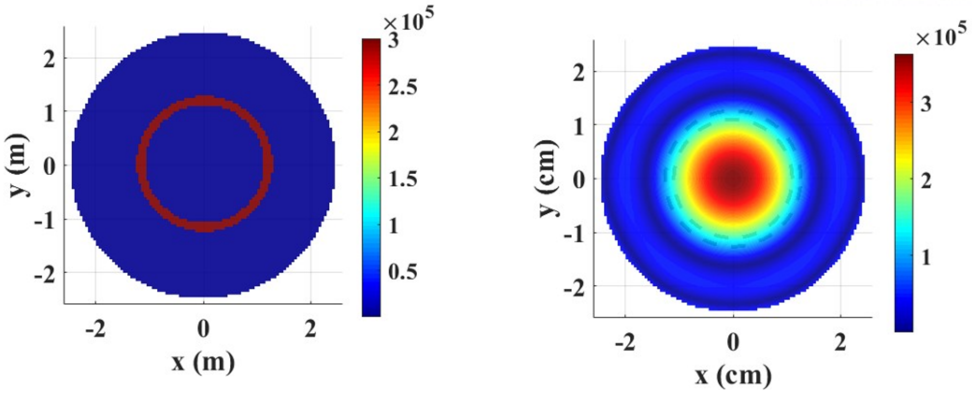

(c) True image (d) Experimental image

Fig. 5.22. Imaging results of carbon rod.

Sensitivity for the given system setup could be analyzed to estimate the detection capability of the system. It is based on the phase shift results in Fig. 5.20 (b), using (5.19-23). As the object conductivity is uniform as 300 kS/m, the analysis is applied to estimate the effect of the object position and size.

Fig. 5.23 shows the analysis as object size, radius of the rod in here, increases from 0.5 to 2.5 cm, with thickness 1 mm. The object with carbon conductivity is placed on the center of the ROI to extend the radius as long as possible. The 4^{th} Rx is utilized, since the Rx in the geometry yields the maximum phase shift. For the radius of the given carbon rod, 1.25 cm, spatial resolution is 1.8 mm. It indicates the shape and position deformation, such as squeezing and crack, larger than 1.8 mm can be detected for the system.

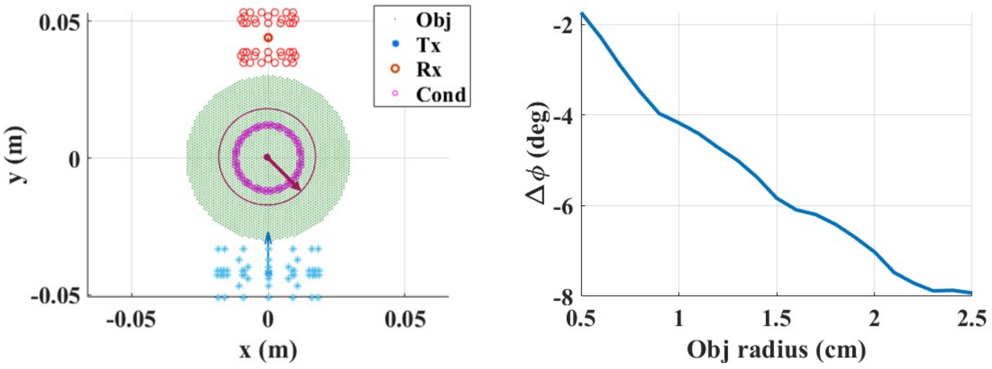

(a) eDMP model for object size change (d) Phase shift as object size changes

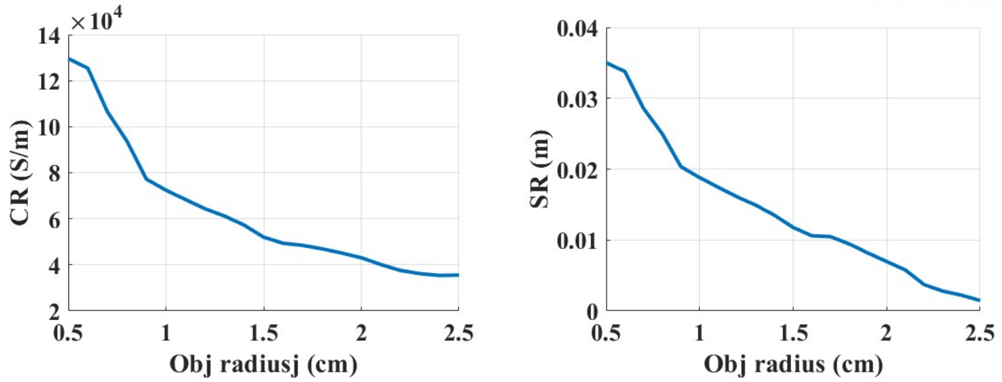

(c) CR as object size changes (d) SR as object size changes

Fig. 5.23. Analysis as object size changes.

Fig. 5.24 shows the effect of the object position. As shown in Fig. 5.24 (a), an object with R_{obj} = 0.5 mm and σ_0 = 3*10^5 S/m is placed on the position along y-axis from 0 to 0.028 m. Fig. 5.24 (b-d) present the effect of position as the phase shift and resolution. SR decreases rapidly as the object become closer to Tx and Rxs, while CR is reduced slowly since SR is a function of the gradient field. Considering $\Delta\varphi_{\min}$, the object can be detected over the position 0.019 m. As shown in Fig. 5.23, the bigger object then 0.5 mm can be detected under the position. It also indicates the geometrical defect, such as a hole and crack, with 1 mm size, cannot be detected within the region.

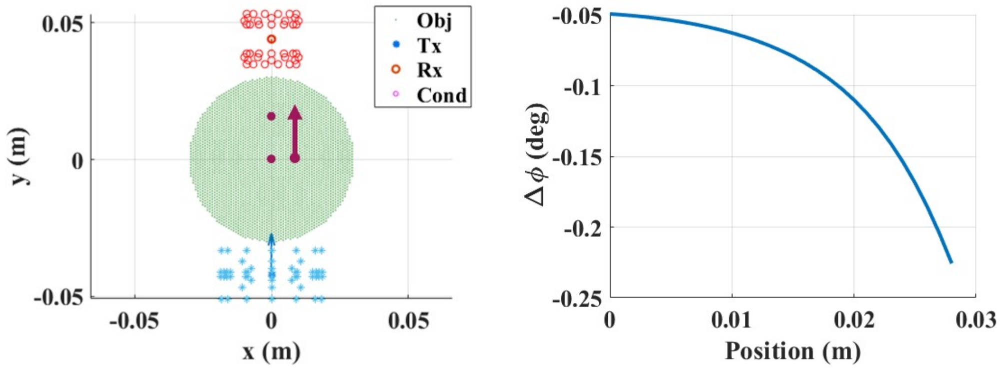

(a) eDMP model for position change (b) Phase shift as object size changes

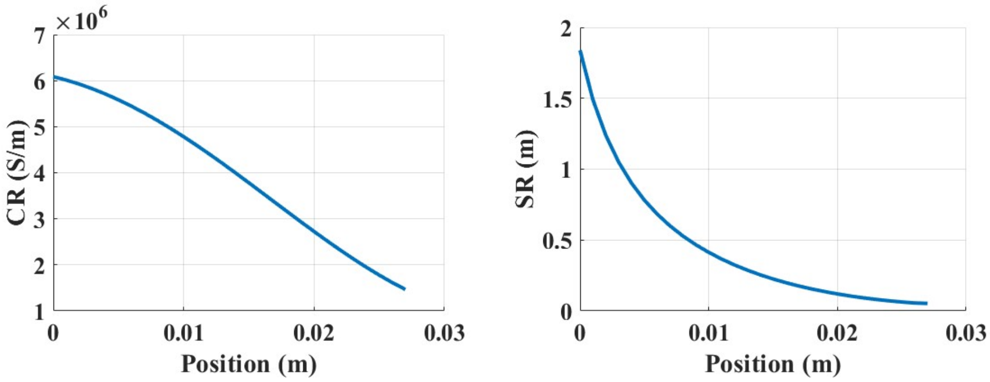

(c) CR as position changes (d) SR as position changes

Fig. 5.24. Analysis as position changes.

Considering the application for the crack detection, the effect of the crack size on the system is investigated. Fig. 5.25 (a) shows the eDMP model with a crack on the carbon rod in Fig. 5.22 (a). The arrangement which the coils are aligned to the crack is set to $\Delta\varphi_0$ and the system rotates 90 deg for $\Delta\varphi_0$ is $\Delta\varphi_{90}$. As $\Delta\varphi_{90}$ causes the maximum difference in phase shift with $\Delta\varphi_0$, the phase difference between $\Delta\varphi_0$ and $\Delta\varphi_{90}$ is computed to estimate the detection capability according to the size of crack. As shown in Fig. 5.25 (b), the phase difference is proportional to the crack size as it increases form 0.2 mm to 5.4 mm. Considering 0.1 deg $\Delta\varphi_{\min}$, the crack size larger than 1.7 mm can be detected in the MIT transceiver system with the given geometry of the carbon rod.

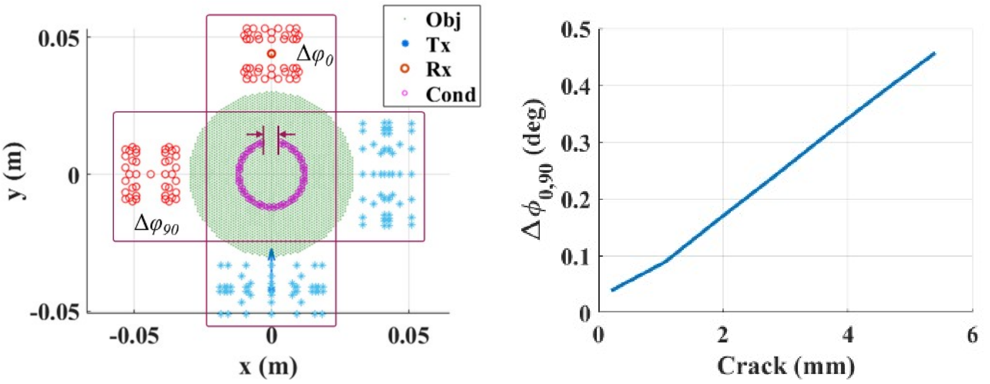

(a) eDMP model of cracked rod (b) Phase difference as crack size changes

Fig. 5.25. Analysis as crack size changes.

5.4.4 Application: Carbon crack detection

A crack occurs on the carbon rod in a straight line and three sizes, 1, 2.5 and 5 mm, are attempted. Fig. 5.26 shows the cracked rod and the imaging results of the crack detection. Due to crack, the circles are cut at the position of crack.

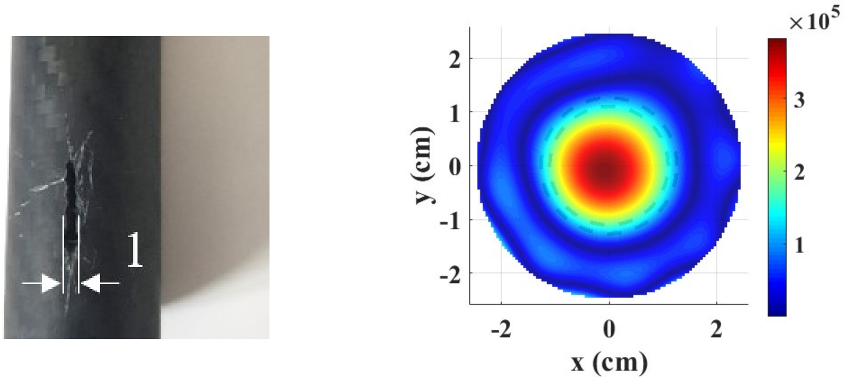

(a) Crack 1 mm (b) Imaging of 1 mm crack

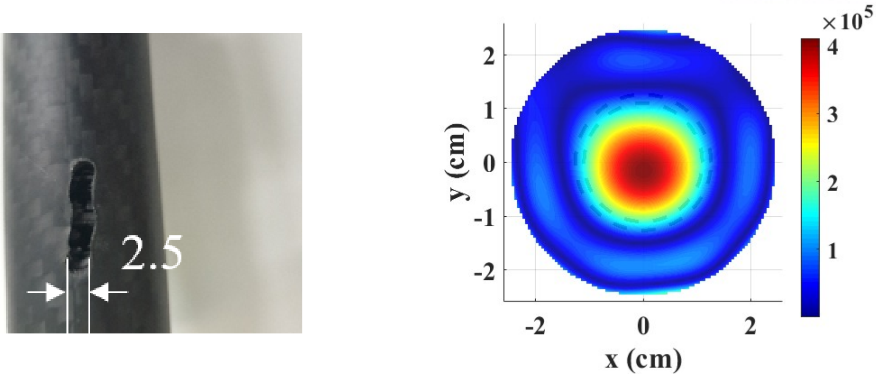

(c) Crack 2.5 mm (d) Imaging of 2.5 mm crack

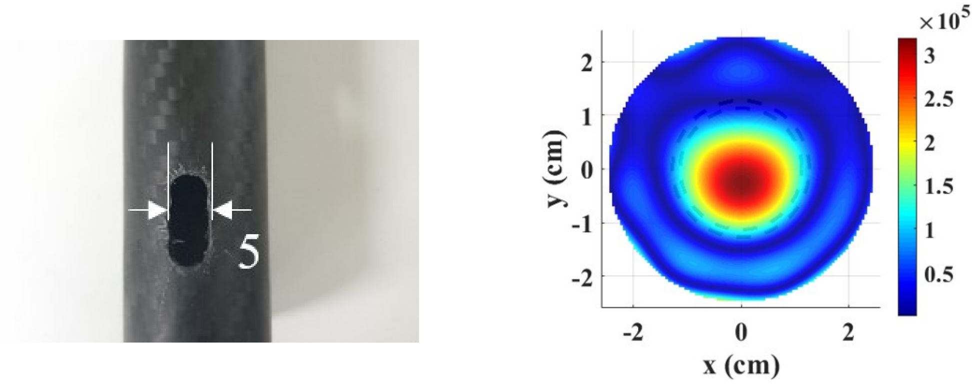

(e) Crack 5 mm (f) Imaging of 5 mm crack

Fig. 5.26. Imaging results of carbon crack detection.

The part of crack is focused in Fig. 5.27 and both normal and cracked rod are compared. It is presented that 1 mm cracked rod has little difference with the normal rod, since the spatial resolution of the system is larger than 1 mm. In Fig. 5.27 (c-d), the gap with the normal circle is shown and grows as much as the size of the crack. It presents that the MIT transceiver system is capable of detecting a crack in the shape, comparing the reference.

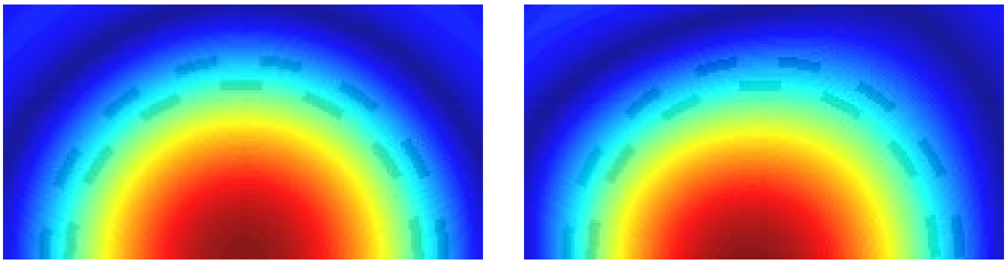

(a) Normal (b) 1 mm

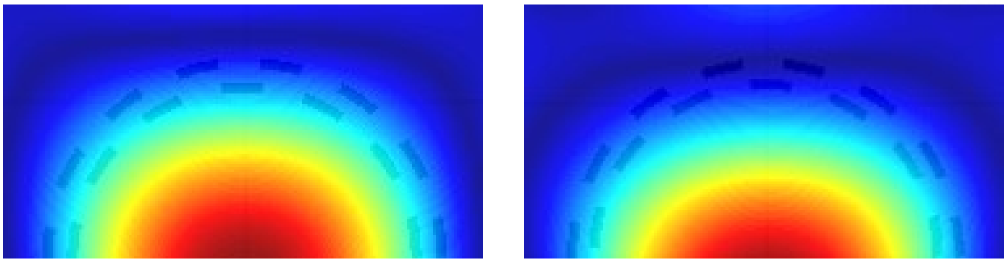

(c) 2.5 mm (d) 5 mm

Fig. 5.27. Crack imaging.

5.5 Application: Egg imaging

An egg is a living cell, containing two different conductivity objects, yolk and white. As shown in Fig. 5.28 (a), the yolk is suspended by a string and surrounded by the white. It has conductivity about 0.3 S/m while albumen is 0.7 S/m at room temperature, due to fatty acid and water. The egg contains white 33 g and the yolk 17 g. Detailed geometry of egg is presented in Table 5.7. The similar MIT system in Fig. 5.5 (a) is used for egg detection as shown in Fig. 5.28 (b)-(d). R_{Tx} is reduced to 5.5 cm in order to increase SNR and Rxs with azimuth angle -30 to 210 deg are used to acquire the effective data. The egg in a plastic case is placed on the origin of the ROI. The object dipoles are distributed with r_i = 2 mm and N_i = 439 per plane.

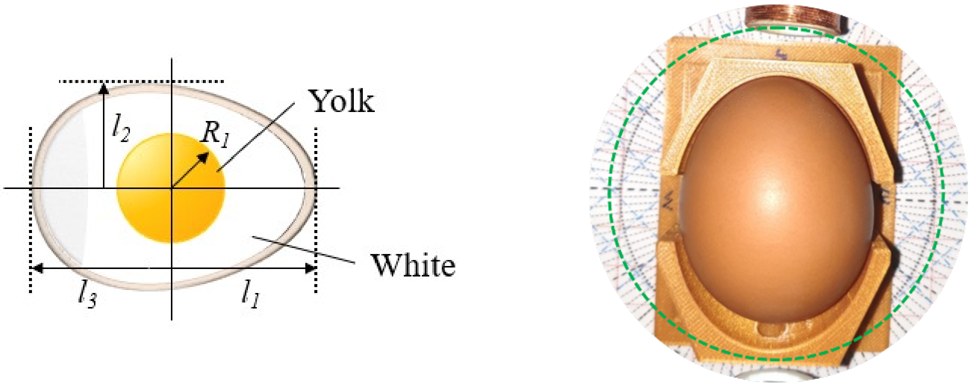

(a) Geometry of egg (b) Picture of egg

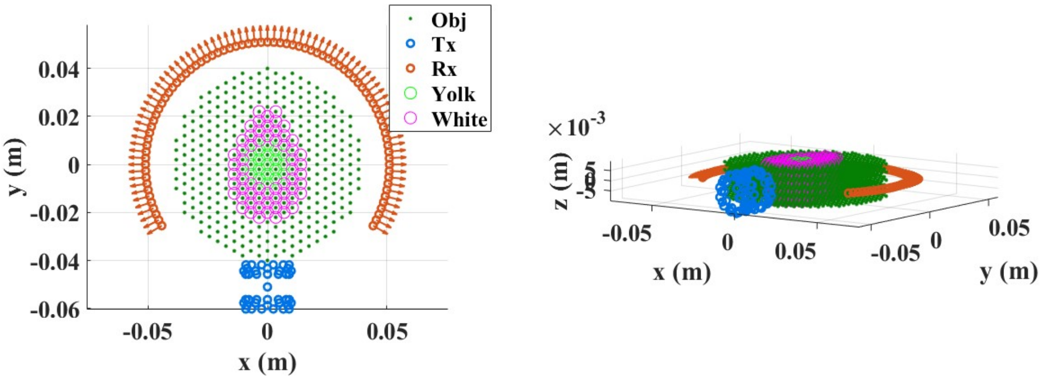

(c) eDMP model in x-y plane (d) eDMP model in 3D view

Fig. 5.28. Setup for egg imaging.

Table 5.7. Geometry of egg

l_1 (cm)	l_2 (cm)	l_3 (cm)	R_1 (cm)
2.3	2.1	2.2	1.0

Fig. 5.29 shows the phase shift results and the reconstructed images of the egg. Mean error of the total phase shifts is 0.0507. The experimental image presents the shape of the egg but the yolk is not characterized, due to lack of resolutions, while the simulation imaging in Fig. 5.29 (b) indicates the position and shape of the yolk. It is challenging to observe the yolk, since the signal from the white is more dominant than that of the yolk. The size of the egg in Fig. 5.29 (c) is smaller than the geometry in Table 5.7 since the cross-section of the egg changes along the z-axis. But it indicates that the MIT system can be used to detect a living cell.

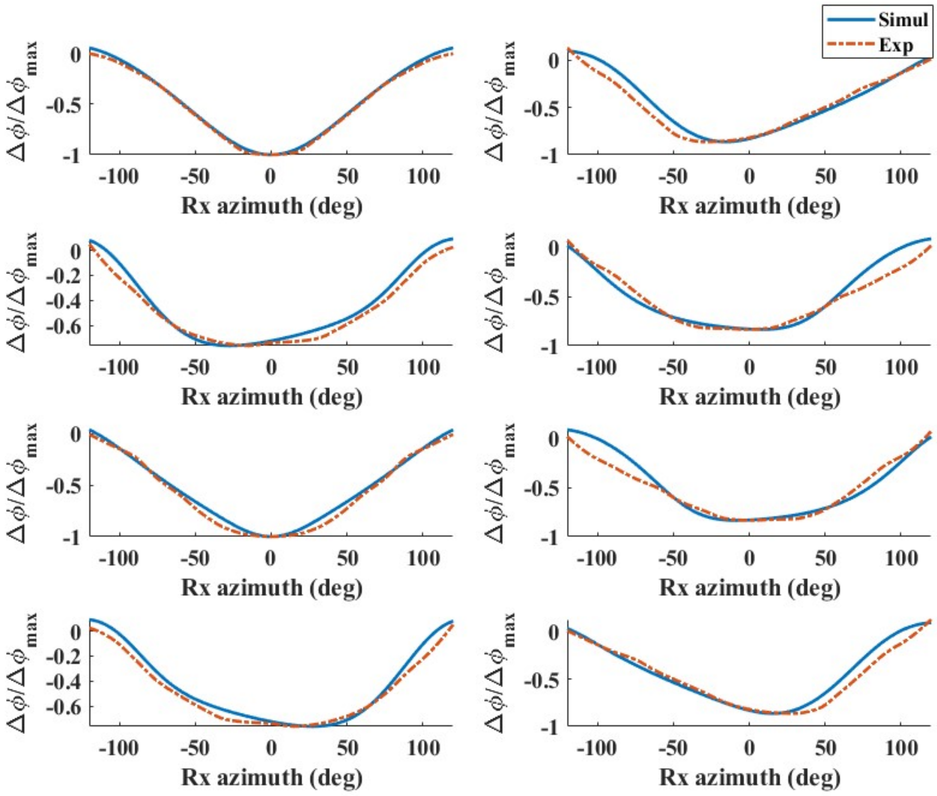

(a) Phase shift of egg

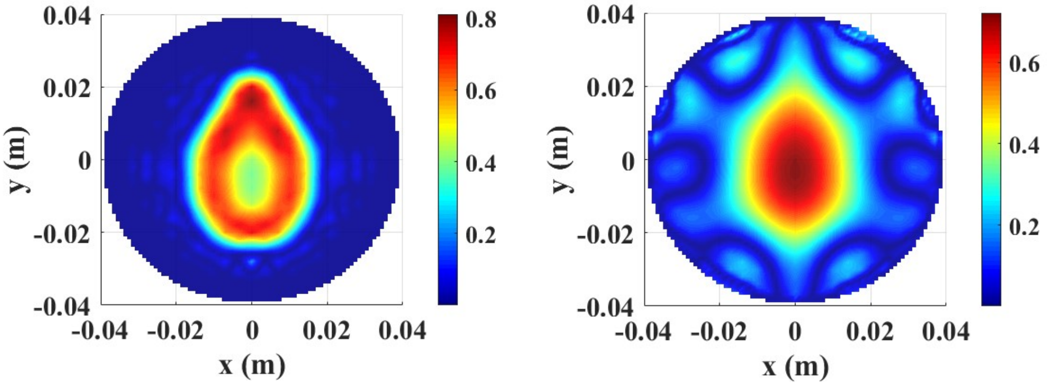

(b) Simulation (c) Experiments

Fig. 5.29. Experimental results of egg.

5.6 Discussion

In this study, a MIT was developed using the eDMP method for modeling and applied to detect target objects with various conductivity. The eDMP method utilized several dipoles for the objects to estimate the magnetic coupling between the coils and objects. The equivalent circuit modeling was applied to analyze the phase shift in the MIT system, considering the object properties. An inverse algorithm was applied using Tikhonov regularization. The phase shifts in the experiments, eDMP and FDTD numerical method were compared. The results showed good agreement as the conductivity, position, and shape of the object were changed. The sensitivity and resolution of the proposed system were estimated. Images were reconstructed and refined to present the properties of a circle and a square. It is expected that the eDMP method contribute to develop an MIT system and achieve better performance. Furthermore, the MIT transceiver system was implemented with automatic measurement and wireless data acquisition. The system observed the crack on the carbon rod and demonstrated the system could be portable. Finally, imaging egg is achieved and the MIT system could observe some change in a target object which larger than the system resolution.

6. Conclusion and open issue

6.1 Achievement and contribution

In this research, a method analyzing and controlling magnetic field was proposed to develop the magnetic biomedical devices using the dipole model. The two illustrative applications, navigation sensor for a tube and magnetic induction tomography were investigated. The navigation sensor reconstructed a path of the tube and MIT generated the tomographic image of low conductivity objects. The detailed achievement contribution is summarized as below:

[Chapter 3]

The eDMP method which is originated from the dipole model was developed to compute the time-varying magnetic field of EMs, including mutual inductance. Unlike single dipole model, the method can be applied to EMs with various designs. It was demonstrated by modeling cylinder coils with different aspect ratios and tapered coils with different slant angle. In case of the taper coils, they were treated as a summation of the cylinder coils. The modeling results were compared to experiments and the other modeling method: analytical method, numerical method (COMSOL). As a practical illustration, it was applied to modeling TMS coil with three designs and analyzed attenuation rate in the ROI. The best design according to the penetration depth could be determined. The eDMP model was used inversely to control the magnetic field. In the circular ROI, strength and orientation of the field were constructed as desired by modulating position, orientation, and strength for a set of the EMs. Practical limitation, such as maximum input power was considered. Controllability of the method was verified through the experiments for various models, changing strength and orientation of the field. The method was utilized to achieve magnetic locomotion for capsule endoscope. A capsule holding PMs took translation and rotation as desired.

[Chapter 4]

A navigation sensor was proposed for an intubation tube since the tube could make perforation during inserting tube, due to sharp curve at throat area. It utilized that mutual inductance between two coils changes as their relative orientation vary. Exciter coil and sensing coil were alternately wound along the tube to track the path of the tube and sensing coils were slanted to distinguish the symmetric position. The eDMP model was used to compute mutual inductance analyze the system. Based on the modeling, design of the navigation sensor was determined to enhance resolution for orientation angle, considering practical usage. Both modeling and design are validated by comparing with experiments and numerical simulations (COMSOL). Finally, it was presented that the navigation sensor could measure orientation at the sharp curve in throat and reconstruct the path of tube.

[Chapter 5]

A novel approach to analyze the magnetic field of MIT using magnetic dipoles and a lumped parameter model was presented. MIT is a medical imaging technique imaging conductivity of target objects. It has a problem of inferior performance due to the nonlinearity, low SNR, and ill-posed condition in inverse problem. The eDMP model and a lumped parameter were used to solve the forward and inverse problem of MIT system. The method was validated through experiments, varying the modeling parameters, and the results were compared to numerical method using FDTD. It was demonstrated that the system can characterize conductivity, position and shape of the target object. The MIT transceiver system was constructed for automatic measurement and data acquisition. Images for the saline water and carbon rod were reconstructed. Comparing the normal image, anomality in the shape were observed. Finally it was used to imaging a living cell. The MIT was implemented as a system and reconstructed images for various materials.

6.2 Open issue

There are several open issues which require continuous investigation for implementation of the devices. Open issues of each chapter are listed below:

[Chapter 3]

Magnetic field modeling and applications in this research was conducted in the magnetic near field with time-harmonic property. The far field cause wave propagation delay which depends on the position. Modeling the far field with higher frequency will be investigated. In addition, the system with irregular motion, such as MRI, requires time-domain analysis. It can be achieved by modifying the modeling equation as a function of time.

[Chapter 4]

In this research, navigation of the sensor was performed in a 2D plane. Considering the practical environment of a patient, navigation in 3D should be achieved. Then, the real-time navigation system displaying 3D path will be implemented and contribute to prevent some injury.

[Chapter 5]

It is demonstrated that the MIT system is capable of detecting low conductivity materials using the eDMP model and the multi-channel MIT transceiver system is constructed. As a future work, the MIT transceiver system should be developed to detect low conductivity materials for medical usage. Imaging multiple objects with various conductivity will be performed to adjust to the practical tissue of human body. A target object would be developed from meat, animals to human. Some practical accidents can be simulated, such as cerebral hemorrhage, using the manikin and artificial blood.

Furthermore, various types of sensors can be utilized. For example, a gradiometer and a superconducting quantum interference device (SQUID) provides the higher sensitivity than a coil sensor. They could contribute to increase the resolutions near the center of the ROI.

Appendix

[Chapter 4]

The magnetic mutual induction in (4.2) is nonlinear and can be linearized in (4.3) by the eDMP method, detailed in A.1.

$$\frac{dM_{ab}}{d\theta}=\sum_{j=1}^{k}\left[\begin{array}{l} m_{bj}\cos(\theta+\beta)Bx_{aj}-m_{bj}\sin(\theta+\beta)Bz_{aj} \\ \qquad +m_{bj}\sin(\theta+\beta)\dfrac{dBx_{aj}}{d\theta}+m_{bj}\cos(\theta+\beta)\dfrac{dBz_{aj}}{d\theta}\end{array}\right] \tag{A.1}$$

where
$$Bx_{aj}=\frac{\mu_0}{4\pi}\sum_{i=1}^{p}\frac{3(m_{ai}\bullet P_{ij})Px_{ij}}{\left|P_{ij}\right|^{5/2}}$$

$$Bz_{aj}=\frac{\mu_0}{4\pi}\sum_{i=1}^{p}\left(\frac{3(m_{ai}\bullet P_{ij})Pz_{ij}-m_{ai}}{\left|P_{ij}\right|^{5/2}}\right)$$

$$\frac{dBx_{aj}}{d\theta}=\frac{\mu_0}{4\pi}\sum_{i=1}^{p}3m_{ai}\frac{\left(\dfrac{d(Pz_{ij}Px_{ij})}{d\theta}\cdot P_{ij}-5/2(Pz_{ij}Px_{ij})\cdot\dfrac{dP_{ij}}{d\theta}\right)}{\left|P_{ij}\right|^{7/2}}$$

$$\frac{dBz_{aj}}{d\theta}=\frac{\mu_0}{4\pi}\sum_{i=1}^{p}\left(3m_{ai}\frac{\left(\dfrac{d(Pz_{ij})^2}{d\theta}\cdot P_{ij}-5/2(Pz_{ij})^2\cdot\dfrac{dP_{ij}}{d\theta}\right)}{\left|P_{ij}\right|^{7/2}}+\frac{3}{2}m_{ai}\frac{1}{\left|P_{ij}\right|^{5/2}}\right)$$

$$|P_{ij}|={Px_{ij}}^2+{Py_{ij}}^2+{Pz_{ij}}^2$$

$$Px_{ij}=\left(-\frac{l}{\theta}+\frac{l\cos\theta}{\theta}+x_{bj}\cos(\theta+\beta)+z_{bj}\sin(\theta+\beta)\right)-x_{ai}$$

$$Py_{ij}=y_{bj}-y_{ai}$$

$$Pz_{ij}=\left(-\frac{l\sin\theta}{\theta}-x_{bj}\sin(\theta+\beta)+z_{bj}\cos(\theta+\beta)\right)-z_{ai}$$

[Chapter 5]

The magnetic flux density in (5.6) can be converted to vector potential $\mathbf{A}_i$ on the loop of I_i, as shown in (A.2-4). $\mathbf{A}_i$ can be computed by substituting $\mathbf{m}_i$ in (3.3), and hence, L_i in (5.4b) is obtained as

$$L_i=\pi r_i^2\left\|\mathbf{B}_i\right\|\Big|_{S_i}\Big/I_i=2\pi r_i\left\|\mathbf{A}_i\right\|\Big|_{r_i}\Big/I_i \tag{A.2}$$

$$\left.\left(\mathbf{A}_i/I_i\right)\right|_{\mathbf{r}=\mathbf{r}_i}=\frac{\mu_0}{4\pi}\frac{\left(\mathbf{m}_i/I_i\right)\times\mathbf{r}_i}{r_i^3}=-\frac{\mu_0}{4}d\mathbf{r}_i \tag{A.3}$$

$$L_i=\mu_0\pi r_i\big/2 \tag{A.4}$$

Reference

[1] M. P. Kummer, J. J. Abbott, B. E. Kratochvil, R. Borer, A. Sengul, and B. J. Nelson, "OctoMag: An Electromagnetic System for 5-DOF Wireless Micromanipulation," *IEEE Transactions on Robotics,* vol. 26, no. 6, pp. 1006-1017, 2010

[2] O. S. Kim, "Low-Q Electrically Small Spherical Magnetic Dipole Antennas," *IEEE Transactions on Antennas and Propagation,* vol. 58, no. 7, pp. 2210-2217, 2010

[3] M. Simi *et al.*, "Magnetically Activated Stereoscopic Vision System for Laparoendoscopic Single-Site Surgery," *IEEE/ASME Transactions on Mechatronics,* vol. 18, no. 3, pp. 1140-1151, 2013

[4] J. Burgner *et al.*, "A Telerobotic System for Transnasal Surgery," *IEEE/ASME Transactions on Mechatronics,* vol. 19, no. 3, pp. 996-1006, 2014

[5] R. Hongliang and P. Kazanzides, "Investigation of Attitude Tracking Using an Integrated Inertial and Magnetic Navigation System for Hand-Held Surgical Instruments," *IEEE/ASME Transactions on Mechatronics,* vol. 17, no. 2, pp. 210-217, 2012

[6] J. García-Martín, J. Gómez-Gil, and E. Vázquez-Sánchez, "Non-Destructive Techniques Based on Eddy Current Testing," *Sensors,* vol. 11, no. 3, pp. 2525-2565, 2011

[7] H. Griffiths, W. R. Stewart, and W. Gough, "Magnetic Induction Tomography: A Measuring System for Biological Tissues," *Annals of the New York Academy of Sciences,* vol. 873, no. 1, pp. 335-345, 1999

[8] Z. Zhang, K. Huang, and C. H. Menq, "Design, Implementation, and Force Modeling of Quadrupole Magnetic Tweezers," *IEEE/ASME Transactions on Mechatronics,* vol. 15, no. 5, pp. 704-713, 2010

[9] R. G. Montague, C. Bingham, and K. Atallah, "Magnetic Gear Pole-Slip Prevention Using Explicit Model Predictive Control," *IEEE/ASME Transactions on Mechatronics,* vol. 18, no. 5, pp. 1535-1543, 2013

[10] H. Son and K.-M. Lee, "Distributed multipole models for design and control of PM actuators and sensors," *IEEE/ASME Transactions on Mechatronics,* vol. 13, no. 2, pp. 228-238, 2008

[11] X. Liu and S. Y. Hui, "Optimal Design of a Hybrid Winding Structure for Planar Contactless Battery Charging Platform," *IEEE Transactions on Power Electronics,* vol. 23, no. 1, pp. 455-463, 2008

[12] J. H. Kim, B. H. Choi, H. R. Kim, and C. T. Rim, "2-D Synthesized Magnetic Field Focusing Technology With Loop Coils Distributed in a Rectangular Formation," *IEEE Transactions on Industrial Electronics,* vol. 66, no. 7, pp. 5558-5566, 2019

[13] L. Kok-Meng and Z. Debao, "A real-time optical sensor for simultaneous measurement of

three-DOF motions," *IEEE/ASME Transactions on Mechatronics,* vol. 9, no. 3, pp. 499-507, 2004

[14] W. L. Leong, Y. Lim, and A. T. Sia, "Palatopharyngeal wall perforation during Glidescope intubation," (in eng), *Anaesth Intensive Care,* vol. 36, no. 6, pp. 870-874, 2008

[15] J. Stoll, H. Ren, and P. E. Dupont, "Passive Markers for Tracking Surgical Instruments in Real-Time 3-D Ultrasound Imaging," *IEEE Transactions on Medical Imaging,* vol. 31, no. 3, pp. 563-575, 2012

[16] M. Rea, D. McRobbie, H. Elhawary, T. Zion Tsz Ho, M. Lamperth, and I. Young, "System for 3-D Real-Time Tracking of MRI-Compatible Devices by Image Processing," *IEEE/ASME Transactions on Mechatronics,* vol. 13, no. 3, pp. 379-382, 2008

[17] R. J. Roesthuis, M. Kemp, J. J. v. d. Dobbelsteen, and S. Misra, "Three-Dimensional Needle Shape Reconstruction Using an Array of Fiber Bragg Grating Sensors," *IEEE/ASME Transactions on Mechatronics,* vol. 19, no. 4, pp. 1115-1126, 2014

[18] A. Plotkin, V. Kucher, Y. Horen, and E. Paperno, "A New Calibration Procedure for Magnetic Tracking Systems," *IEEE Transactions on Magnetics,* vol. 44, no. 11, pp. 4525-4528, 2008

[19] T. Reichl, N. Gardiazabal J Fau - Navab, and N. Navab, "Electromagnetic servoing-a new tracking paradigm," (in eng), no. 1558-254X (Electronic),

[20] A. M. Franz, T. Haidegger, W. Birkfellner, K. Cleary, T. M. Peters, and L. Maier-Hein, "Electromagnetic Tracking in Medicine-A Review of Technology, Validation, and Applications," *IEEE Transactions on Medical Imaging,* vol. 33, no. 8, pp. 1702-1725, 2014

[21] M. Soleimani, W. R. B. Lionheart, and A. J. Peyton, "Image Reconstruction for High-Contrast Conductivity Imaging in Mutual Induction Tomography for Industrial Applications," *IEEE Transactions on Instrumentation and Measurement,* vol. 56, no. 5, pp. 2024-2032, 2007

[22] L. Ma, S. Spagnul, and M. Soleimani, "Metal Solidification Imaging Process by Magnetic Induction Tomography," *Scientific Reports,* vol. 7, no. 1, p. 14502, 2017

[23] Y. Zhou, Q. Ma, G. Guo, J. Tu, and D. Zhang, "Magneto-acousto-electrical Measurement Based Electrical Conductivity Reconstruction for Tissues," *IEEE Transactions on Biomedical Engineering,* vol. 65, no. 5, pp. 1086-1094, 2018

[24] L. Wang and A. M. Al-Jumaily, "Imaging of Lung Structure Using Holographic Electromagnetic Induction," *IEEE Access,* vol. PP, no. 99, pp. 20313-20318, 2017

[25] A. V. Korjenevsky and V. A. Cherepenin, "Progress in realization of magnetic induction tomography," *Annals of the New York Academy of Sciences,* vol. 873, no. 1, pp. 346-352, 1999

[26] H. Wei and M. Soleimani, "Theoretical and Experimental Evaluation of Rotational Magnetic Induction Tomography," *IEEE Transactions on Instrumentation and Measurement,* vol. 61, no. 12, pp. 3324-3331, 2012

[27] J. Xiang, Y. Dong, M. Zhang, and Y. Li, "Design of a Magnetic Induction Tomography

System by Gradiometer Coils for Conductive Fluid Imaging," *IEEE Access,* vol. 7, pp. 56733-56744, 2019

[28] B. U. Karbeyaz and N. G. Gencer, "Electrical conductivity imaging via contactless measurements: an experimental study," *IEEE Transactions on Medical Imaging,* vol. 22, no. 5, pp. 627-635, 2003

[29] S. Hermann, K. L. Helmut, and R. Javier, "Magnetic induction tomography: hardware for multi-frequency measurements in biological tissues," *Physiological Measurement,* vol. 22, no. 1, p. 131, 2001

[30] D. Gürsoy and H. Scharfetter, "Imaging artifacts in magnetic induction tomography caused by the structural incorrectness of the sensor model," *Measurement Science and Technology,* vol. 22, no. 1, p. 015502, 2011

[31] H.-Y. Wei and M. Soleimani, "Hardware and software design for a National Instrument-based magnetic induction tomography system for prospective biomedical applications," *Physiological Measurement,* vol. 33, no. 5, pp. 863-879, 2012

[32] J. R. Feldkamp, "Single-coil magnetic induction tomographic three-dimensional imaging," *Journal of Medical Imaging,* vol. 2, no. 1, pp. 013502-013502, 2015

[33] C. A. González, C. Villanueva, C. Vera, O. Flores, R. D. Reyes, and B. Rubinsky, "The detection of brain ischaemia in rats by inductive phase shift spectroscopy," *Physiological Measurement,* vol. 30, no. 8, pp. 809-819, 2009

[34] G. Jin *et al.*, "A new method for detecting cerebral hemorrhage in rabbits by magnetic inductive phase shift," *Biosensors and Bioelectronics,* vol. 52, pp. 374-378, 2014

[35] S. Zhao *et al.*, "An Experimental Study of Relationship Between Magnetic Induction Phase Shift and Brain Parenchyma Volume With Brain Edema in Traumatic Brain Injury," *IEEE Access,* vol. 7, pp. 20974-20983, 2019

[36] D. Gürsoy and H. Scharfetter, "The effect of receiver coil orientations on the imaging performance of magnetic induction tomography," *Measurement Science and Technology,* vol. 20, no. 10, p. 105505, 2009

[37] D. Gursoy and H. Scharfetter, "Optimum Receiver Array Design for Magnetic Induction Tomography," *IEEE Transactions on Biomedical Engineering,* vol. 56, no. 5, pp. 1435-1441, 2009

[38] C. Deans, L. Marmugi, S. Hussain, and F. Renzoni, "Optical atomic magnetometry for magnetic induction tomography of the heart," in *Quantum Optics*, 2016, vol. 9900, p. 99000F: International Society for Optics and Photonics.

[39] K. Stawicki, S. Gratkowski, M. Komorowski, and T. Pietrusewicz, "A New Transducer for Magnetic Induction Tomography," *IEEE Transactions on Magnetics,* vol. 45, no. 3, pp. 1832-1835, 2009

[40] M. Zolgharni, H. Griffiths, and P. D. Ledger, "Frequency-difference MIT imaging of cerebral haemorrhage with a hemispherical coil array: numerical modelling," *Physiological Measurement,* vol. 31, no. 8, pp. S111-S125, 2010

[41] C. Tan, Y. Wu, Z. Xiao, and F. Dong, "Optimization of Dual Frequency-Difference MIT Sensor Array Based on Sensitivity and Resolution Analysis," *IEEE Access,* vol. 6, pp. 34911-34920, 2018

[42] F. Li, J. F. P. J. Abascal, M. Desco, and M. Soleimani, "Total Variation Regularization With Split Bregman-Based Method in Magnetic Induction Tomography Using Experimental Data," *IEEE Sensors Journal,* vol. 17, no. 4, pp. 976-985, 2017

[43] X. Liu and Z. Liu, "A novel algorithm based on L1-Lp norm for inverse problem of electromagnetic tomography," *Flow Measurement and Instrumentation,* vol. 65, pp. 318-326, 2019

[44] R. Merwa, K. Hollaus, B. Brandst tter, and H. Scharfetter, "Numerical solution of the general 3D eddy current problem for magnetic induction tomography (spectroscopy)," *Physiological Measurement,* vol. 24, no. 2, pp. 545-554, 2003

[45] L. Ma and M. Soleimani, "Magnetic induction tomography methods and applications: a review," *Measurement Science and Technology,* vol. 28, no. 7, pp. 072001-072012, 2017

[46] Q. Wang, *Practical design of magnetostatic structure using numerical simulation*. John Wiley & Sons, 2013.

[47] N. D. Geeter, G. Crevecoeur, and L. Dupré, "An Efficient 3-D Eddy-Current Solver Using an Independent Impedance Method for Transcranial Magnetic Stimulation," *IEEE Transactions on Biomedical Engineering,* vol. 58, no. 2, pp. 310-320, 2011

[48] Z. Xiao, C. Tan, and F. Dong, "Effect of inter-tissue inductive coupling on multi-frequency imaging of intracranial hemorrhage by magnetic induction tomography," *Measurement Science and Technology,* vol. 28, no. 8, p. 084001, 2017

[49] E. M. Wassermann and S. H. Lisanby, "Therapeutic application of repetitive transcranial magnetic stimulation: a review," *Clinical Neurophysiology,* vol. 112, no. 8, pp. 1367-1377, 2001

[50] A. Zangen, Y. Roth, B. Voller, and M. Hallett, "Transcranial magnetic stimulation of deep brain regions: evidence for efficacy of the H-Coil," *Clinical Neurophysiology,* vol. 116, no. 4, pp. 775-779, 2005

[51] Z.-D. Deng, S. H. Lisanby, and A. V. Peterchev, "Coil design considerations for deep transcranial magnetic stimulation," *Clinical Neurophysiology,* vol. 125, no. 6, pp. 1202-1212, 2014

[52] F. Wu, J. Jeon, S. K. Moon, H. J. Choi, and H. Son, "Voice Coil Navigation Sensor for Flexible Silicone Intubation," *IEEE/ASME Transactions on Mechatronics,* vol. 21, no. 2, pp.

851-859, 2016

[53] F. Wu, S. Moon, and H. Son, "Orientation Measurement Based on Magnetic Inductance by the Extended Distributed Multi-Pole Model," *Sensors,* vol. 14, no. 7, p. 11504, 2014

[54] J. Jeon and H. Son, "Active Control of Magnetic Field Using eDMP Model for Biomedical Applications," *IEEE/ASME Transactions on Mechatronics,* vol. 23, no. 1, pp. 29-37, 2018

[55] F. Wu, S. K. Moon, and H. Son, "Orientation measurement based on magnetic inductance by the extended distributed multi-pole model," *Sensors,* vol. 14, no. 7, pp. 11504-11521, 2014

[56] P. L. K. J. Binns, C. Trowbridge, *The analytical and numerical solution of electric and magnetic fields*. Wiley, 1992.

[57] S. Babic, F. Sirois, C. Akyel, and C. Girardi, "Mutual Inductance Calculation Between Circular Filaments Arbitrarily Positioned in Space: Alternative to Grover's Formula," *IEEE Transactions on Magnetics,* vol. 46, no. 9, pp. 3591-3600, 2010

[58] T. C. John, "Inductance Calculations for Noncoaxial Coils Using Bessel Functions," *IEEE Transactions on Magnetics,* vol. 43, no. 3, pp. 1023-1034, 2007

[59] E. Joy, A. Dalal, and P. Kumar, "The Accurate Computation of Mutual Inductance of Two Air Core Square Coils with Lateral and Angular Misalignments in a Flat Planar Surface," *IEEE Transactions on Magnetics,* vol. 50, no. 1, 2014

[60] J. Jeon, W. Chung, and H. Son, "Magnetic Induction Tomography Using Magnetic Dipole and Lumped Parameter Model," *IEEE Access,* vol. 7, pp. 70287-70295, 2019

[61] H. PA *et al.* (2018, May 15) *IT'IS Database for thermal and electromagnetic parameters of biological tissues*. (4th ed.) [Online]. Available: http://itis.swiss/database

[62] C. S. Park *et al.*, "A Portable Phase-Domain Magnetic Induction Tomography Transceiver with Phase-Band Auto-Tracking and Frequency-Sweep Capabilities," *Sensors,* vol. 18, no. 11, p. 3816, 2018

Acknowlegement

It is great honor to present this dissertation for Ph.D degree. Above all, I'd like to say thank to my God, family for supporting me, mother and father, dear sister Ji Hyun and brother Seung-Ki.

I'd appreciate my research advisor Prof. Hungsun Son. I respect him as an engineer, professor, and advisor. My researches have been proceeded under his direction and achieved some papers and patent.

My laboratory companions have contributed to this research. Particularly, Wonmo Chung performed a part of simulation and experiments. Myunggun Kim, Seongmin Lee, Chanbeom Bak, Minho Shin, Hoyoung Kim, Junguk Kim, Sangheon Lee, Sejoon Joo and Minsu Kimm spent a long time together and have discussed about the various research topics. Soyoon Kim deserves my thanks for encouraging me. Sang-A Park is a good friend caring me. Also, I appreciate Wu Fang, who is my first mentor for the magnetic field research. She was a first Ph.D student of Prof. Hungsun Son. I wrote the first paper about the voice coil navigation sensor with her and inherited her researches about the eDMP and MIT. I'm grateful to Chan Sam Park, who has collaborated research about the MIT transceiver. Owing to his genius research about transceiver, I have further developed the MIT research.

Curriculum Vitae

Jiyun Jeon
Soopbil1, 201 ho, 10-10, Daeri 3-gil, Ulju-gun, Ulsan, Republic of Korea, 44922
jyjeon@unist.ac.kr / jyjeon19@gmail.com
+82-10-9067-6330

EDUCATION

Mar. 2014 - Feb. 2020	**Ulsan National Institute of Science and Technology (UNIST)** • Combined MS-Ph.D degree in the school of Mechanical, Aerospace and Nuclear Engineering • Electromechanical system and control laboratory	Ulsan, Korea
Mar.2010 - Feb. 2014	**Ulsan National Institute of Science and Technology (UNIST)** • B.S. in the school of Mechanical and Nuclear Engineering	Ulsan, Korea

RESEARCH PUBLICATION

- **Jiyun Jeon**, Wonmo Chung and Hungsun Son*, "Magnetic Induction Tomography Using Magnetic Dipole and Lumped Parameter Model," *IEEE Access*, 2019
- Chan Sam Park, **Jiyun Jeon**, Byungjoo Oh, Hee Young Chae, Kyeonghwan Park, Hungsun Son and Jae Joon Kim*, "A Portable Phase-Domain Magnetic Induction Tomography Transceiver with Phase-Band Auto-Tracking and Frequency-Sweep Capabilities," *Sensors*, 2018
- **Jiyun Jeon** and Hungsun Son*, "Active Control of Magnetic Field Using eDMP Model for Biomedical Applications," *IEEE/ASME Trans. Mechatronics*, 2018
- Fang Wu, **Jiyun Jeon** (equal contribution), Seung Ki Moon, Hae-Jin Choi, and Hungsun Son*, "Voice Coil Navigation Sensor for Flexible Silicone Intubation," *IEEE/ASME Trans. Mechatronics*, 2016

* *Corresponding author*

PATENTS

- Hungsun Son, **Jiyun Jeon** "A voice coil navigation sensor for intubation tube and the manufacturing," Korea, Patent No. 10-1764327 (2017)

CONFERENCE PROCEEDING

- **Jiyun Jeon** and Hungsun Son*, "Design Improvement of magnetic induction tomography using the extended multi-poles and equivalent circuit model," *IEEE International conference of advanced intelligent mechatronics (AIM)*, München, Germany, 2017
- Fang Wu, **Jiyun Jeon** and Hungsun Son*, "A novel magnetic orientation sensor for intubation procedures," *IEEE International conference of advanced intelligent mechatronics (AIM)*, Busan, Korea, 2015

* *Corresponding author*